

The effect of elastic modulus and equilibrium vapor adsorption on capillary forces

Dissertation

zur Erlangung des Grades

„Doktor der Naturwissenschaften“

*am Fachbereich Physik, Mathematik und Informatik
der Johannes Gutenberg-Universität in Mainz*

vorgelegte von

Marjan Zakerin

geboren in Shiraz, Islamic Republic of Iran

Mainz, den 16 Mai 2013

Tag der Promotion: 16.05.2013

Zusammenfassung

Die Kapillarkraft entsteht durch die Bildung eines Meniskus zwischen zwei Festkörpern. In dieser Doktorarbeit wurden die Auswirkungen von elastischer Verformung und Flüssigkeitsadsorption auf die Kapillarkraft sowohl theoretisch als auch experimentell untersucht.

Unter Verwendung eines Rasterkraftmikroskops wurde die Kapillarkraft zwischen einem Siliziumoxid Kolloids von $2\text{ }\mu\text{m}$ Radius und eine weiche Oberfläche wie n.a Polydimethylsiloxan oder Polyisopren, unter normalen Umgebungsbedingungen sowie in variierende Ethanolampfdrücken gemessen. Diese Ergebnisse wurden mit den Kapillarkräften verglichen, die auf einem harten Substrat (Silizium-Wafer) unter denselben Bedingungen gemessen wurden. Wir beobachteten eine monotone Abnahme der Kapillarkraft mit zunehmendem Ethanolampfdruck (P) für $P/P_{sat} > 0,2$, wobei P_{sat} der Sättigungsdampfdruck ist.

Um die experimentellen Ergebnisse zu erklären, wurde ein zuvor entwickeltes analytisches Modell (Soft Matter 2010, 6, 3930) erweitert, um die Ethanoladsorption zu berücksichtigen. Dieses neue analytische Modell zeigte zwei verschiedene Abhängigkeiten der Kapillarkraft von P/P_{sat} auf harten und weichen Oberflächen. Für die harte Oberfläche des Siliziumwafers wird die Abhängigkeit der Kapillarkraft vom Dampfdruck vom Verhältnis der Dicke der adsorbierten Ethanolschicht zum Meniskusradius bestimmt. Auf weichen Polymeroberflächen hingegen hängt die Kapillarkraft von der Oberflächenverformung und des Laplace-Drucks innerhalb des Meniskus ab. Eine Abnahme der Kapillarkraft mit zunehmendem Ethanolampfdruck hat demnach eine Abnahme des Laplace-Drucks mit zunehmendem Meniskusradius zur Folge.

Die analytischen Berechnungen, für die eine Hertzsche Kontakt-deformation angenommen wurde, wurden mit Finit Element Methode Simulationen verglichen, welche die reale Deformation des elastischen Substrats in der Nähe des Meniskus explizit berücksichtigen. Diese zusätzliche nach oben gerichtete Oberflächenverformung im Bereich des Meniskus führt zu einer weiteren Erhöhung der Kapillarkraft, insbesondere für weiche Oberflächen mit Elastizitätsmodulen $< 100\text{ MPa}$.

Abstract

Capillary force arises from a meniscus forming a liquid bridge between two solids. In this thesis, the effects of elastic deformation and liquid adsorption on the capillary force were analyzed both theoretically and experimentally. Using an atomic force microscope, the adhesion force between silica spheres of $2\text{ }\mu\text{m}$ radius and soft surfaces (polydimethylsiloxane and polyisoprene) was measured both in ambient conditions as well as in the presence of different vapor pressures of ethanol. Results were compared to adhesion forces measured on a hard substrate (silicon wafer). We observed a monotonous decrease of capillary force with increasing ethanol vapor pressure (P) for $P/P_{sat} > 0.2$, where P_{sat} is the saturation vapor pressure.

In order to explain the experimental results, a previously developed analytical model (Soft Matter 2010, 6, 3930) was extended to take into account vapor adsorption of ethanol. The new analytical model revealed two different mechanisms for the dependence of capillary force on hard and soft surfaces. For a hard Si wafer, the ratio between adsorbed layer thickness and the meniscus radius determines the dependence of capillary force on vapor pressure. For the soft polymer surfaces, the capillary force is controlled by the interplay of surface deformability and Laplace pressure within the meniscus. In other words, the monotonous decrease of capillary force with increasing of ethanol vapor pressure follows the decrease of Laplace pressure with increasing meniscus radius.

The analytical calculations that assumed a Hertzian contact deformation were compared to finite element method simulations which allowed taking the detailed deformation of the elastic support close the meniscus explicitly into account. The effect of this additional upward surface deformation within the meniscus area leads to a further increase in capillary force for soft surfaces specially for elastic moduli below 100 MPa.

Contents

List of Figures	v
List of Tables	xiii
1 Introduction	1
1.1 Motivation	1
1.2 Wet adhesion mechanism of tree frogs – state of art	3
1.3 Aim and objectives	7
1.4 Overview of thesis	9
2 Basics, principles and analytical models	11
2.1 Van der Waals interaction between the molecules	11
2.2 Van der Waals interaction between macroscopic objects	13
2.2.1 Hamaker microscopic approach	13
2.2.2 Lifshitz theory	15
2.2.3 Retarded van der Waals forces	16
2.3 Free surface energy theory of adhesion	17
2.4 Contact mechanics	18
2.4.1 Hertz model	19
2.5 Capillary forces	22
2.5.1 Liquid surface tension	22
2.5.2 Young–Laplace equation	24
2.5.3 Kelvin equation	25
2.6 Equilibrium vapor adsorption on solid surfaces: liquid physisorption . .	26
2.7 Capillary forces between a rigid sphere and a rigid plane: the influence of physisorbed layers	28

2.8	Capillary force for the deformable surfaces – a simple analytical model .	30
2.9	Capillary force for the deformable surfaces in presence of adsorbed layers – the new analytical model	30
2.9.1	Rigid sphere in contact with an elastic support including ph- ysisorbed liquid layers on both surfaces	32
2.9.2	Rigid sphere in contact with an elastic hydrophobic support in- cluding a physisorbed liquid layer only on the sphere	34
2.9.3	Relative contributions of meniscus force, adsorbed layer thick- ness, and support deformation	35
2.10	Summary	36
3	Materials and methods	37
3.1	Sample preparation	37
3.1.1	Silicon wafers	38
3.1.2	PDMS samples	38
3.1.3	O ₂ plasma treatment of PDMS samples	39
3.1.4	Polyisoprene samples	40
3.1.5	Pulse Nuclear magnetic resonance (NMR) spectroscopy	41
3.2	Contact angle measurement	43
3.3	Atomic force microscopy	43
3.3.1	Contact mode of AFM	44
3.3.2	Tapping or intermittent contact mode	45
3.3.3	Force spectroscopy and measuring the adhesion force	47
3.3.4	Root-mean-square roughness	49
3.4	Colloidal probe preparation	50
3.5	Thermal noise method: measuring a cantilever spring constant	51
3.6	Ethanol vapor pressure control	52
3.7	Mechanical characterization using stress-strain curves	53
3.7.1	True Stress and Strain	53
3.7.2	Engineering stress and strain	53
3.7.3	Measuring engineering stress-strain curves	54
3.7.3.1	Tensile test	55
3.7.3.2	Compression test	55

3.8	Scanning electron microscopy	56
3.9	Sum frequency generation (SFG) spectroscopy	57
3.10	Finite element method (FEM) simulation	59
3.10.1	Introduction to finite element method simulation	60
3.10.1.1	Discretization	61
3.10.1.2	Linear guess function	61
3.10.1.3	Minimizing the residual function	63
3.10.2	Geometry and the coordinate system	64
3.10.3	Physics governing the finite element method (FEM) model . . .	64
3.10.4	Calculation of the adhesion force	66
3.10.5	Studies made by finite element simulations	67
3.11	Summary	68
4	Results and discussion	69
4.1	Introduction	69
4.2	Experimental results	70
4.2.1	Surface characterization of soft samples using tapping mode imag- ing	70
4.2.1.1	Soft 10:1 and 20:1 PDMS samples	71
4.2.1.2	Soft cis-1,4 PI samples with different molecular weights	71
4.2.2	Determining the elastic moduli of the soft samples	73
4.3	Adhesion force in the ambient condition: effect of cantilever speed and dwell time	73
4.3.1	Dynamic adhesion measurements: dependence of hysteresis and adhesion force on cantilever speed	74
4.3.2	Static adhesion: influence of dwell time	76
4.4	Contact angle measurement	78
4.5	Sum frequency generation (SFG) spectroscopy	78
4.6	Adhesion force-versus-relative vapor pressure of a liquid	80
4.6.1	Adhesion force-versus-relative vapor pressure of water on O ₂ plasma treated 10:1 PDMS sample	81
4.7	Adhesion force-versus- P/P_{sat} of ethanol	85
4.7.1	Adhesion force-versus- P/P_{sat} for a hard substrate	85

4.7.2	Adhesion force-versus- P/P_{sat} for soft PDMS substrates	87
4.7.2.1	The adhesion force-versus-ethanol P/P_{sat} of ethanol: the comparison between Si wafer and soft PDMS samples	88
4.7.3	Adhesion force-versus- P/P_{sat} of ethanol between the silica micro- spheres and the soft cis-1,4 PI samples	89
4.7.3.1	The adhesion force-versus- P/P_{sat} of ethanol: the com- parison between a rigid surface and soft PI samples . . .	91
4.7.3.2	The adhesion forces between a 2 μm radius silica micro- sphere and 2500 kDa cis-1,4 PI polymer sample in the liquid ethanol	91
4.8	Scanning electron microscope (SEM) images from some of colloidal probes	92
4.9	Finite element method simulation results	94
4.9.1	A rigid support	94
4.9.2	Soft elastic support	96
4.9.3	Dependence on elastic modulus for fixed P/P_{sat}	97
4.10	Comparing the FEM simulation as well as analytical results with the experiments	98
4.11	Summary	100
5	Conclusion and outlook	101
5.1	Conclusion	101
5.2	Outlook for future	102
	Bibliography	104

List of Figures

1.1	Morphology of tree frog toe pads. (a) White’s tree frog (<i>Litoria caerulea</i>). (b–d) Scanning electron microscope images of (b) a toe pad, (c) epidermis with hexagonal epithelial cells and (d) high power view of the surface of a single hexagonal cell showing peg-like projections. (e) Tunnelling electron microscope image of a cross-section through cell surface (35).	2
1.2	A torrent frog clinging to a vertical surface flooded by water. The picture was kindly provided by Jon Barnes group in Glasgow.	2
1.3	(a) A schematic showing different components in a wet adhesion measurement between a smooth solid surface and a disc with radius r . (b) The schematic shows the contact angles (θ_1 and θ_2) between the fluid and the two adjoining surfaces (7).	4
1.4	Friction force of single toe pads of <i>Litoria caerulea</i> during a sliding experiment consisting of 20 s sliding toward the body ($500 \mu\text{m s}^{-1}$) followed by 2 minute standstill. Shear forces were recorded (i) at the onset of pad sliding; (ii) during steady sliding (at the end of the movement); and (iii) 2 minutes after the movement had stopped (35).	5
1.5	(a) Images of indentation with the 1.5 mm-diameter sapphire sphere. (b) Effects of indentation depth on effective elastic modulus, open and filled circles represent data from the two mature adult frogs, frogs 1 and 2, respectively. The data were fitted by exponential curves of the form $y = y_0 + ae^{-bx}$ (9).	6

LIST OF FIGURES

2.1	(a) Keesom dipole–dipole interaction, (b) Debye interaction between the dipole–induced dipole, and (c) the London dispersion interaction between the induced dipoles–induced dipoles in the molecules. D is the distance between two molecules.	12
2.2	Geometry for calculation of the vdW force between molecule A and planar surface made from molecules B (19).	14
2.3	Van der Waals potential energy between different macroscopic objects (47).	15
2.4	Two parallel planar half–spaces made from the materials 1 and 2, respectively. The distance between the two parallel half–spaces, D , is filled with the material 3.	16
2.5	Contact between a hard sphere and an elastic surface with no applied force: (a) in the absence of the attractive forces between the two bodies, (b) in the presence of attractive forces, surfaces are drawn together to make contact over a circle of radius a . (14)	18
2.6	Schematic of a sphere/plane geometry. A hard sphere is indenting an elastic half–space support. F is the external load, a is the contact radius and δ is the indentation of hard sphere onto the elastic support.	20
2.7	Surface tension results from the imbalanced molecular forces at the surface of the liquid. High values of the surface tension means the molecules tend to interact strongly.	22
2.8	A schematic defining the contact angle, θ , of a liquid on a solid surface. θ is the measure of liquid affinity with the solid surface.	23
2.9	An stretched rubber membrane at the end of a cylindrical tube with different inside pressure, P_{in} , compared with the outside pressure, P_0 (44).	24
2.10	A meniscus in cylindrical coordinate system with rotational symmetry. The principle radii of curvature are r and l . The meniscus is formed in the contact area between a sphere with radius R and a plane. Θ_1 and Θ_2 are the contact angles of liquid with the sphere and plane, respectively.	25
2.11	The adsorption isotherm for ethanol, 1-butanol, and 1-pentanol as measured by the attenuated total reflectance–IR experiment. The solid blue line is the representative fit for all the three isotherms (4).	27

LIST OF FIGURES

2.12	Circular approximation where the meridional curvature is replaced with a circle with a fixed radius, r . Note that r is negative because the center of the circle is outside the meniscus; so $-r$ is positive. At the position where r and l (cross-sectional radii) are parallel to the substrate, the Pythagorean theorem can be used to relate R , adsorbate thickness h' , r and l	29
2.13	Schematic of an elastically deformed surface indented by a hard sphere in presence of a liquid meniscus and (a) adsorbate layers on both surfaces and (b) only on colloidal probe. r' and z' are the axis of the axisymmetric coordinates system. $\Delta z(r')$ denotes the deflection of the surface and is given by the Hertz contact mechanics model.	31
3.1	(a) Two barrel epoxy dispersion gun applied to create, (b) a rectangular green polyvinylsiloxane mold with the lateral dimensions of $2 \times 3 \text{ cm}^2$ on the clean glass slides.	39
3.2	(a) The surface of a freshly prepared 10:1 PDMS sample with Me denoting the methyl group of CH_3 . (b) The plasma is ignited and the surface modification starts: oxygen breaks some of the Si-CH_3 bonds. (c) Some Si-CH_3 bonds at the surface are substituted by Si-OH bonds. The extent of substitution depends on the plasma treatment conditions.	39
3.3	Different PI isomers known as (1) cis-1,4, (2) trans-1,4, (3) 1,2 and (4) 3,4 PI polymers.	40
3.4	Schematic diagram of a NMR spectrometer showing various components.	41
3.5	One-dimensional 300 MHz ^1H NMR spectrum measured for 800 kDa cis-1,4 PI polymer in CDCl_3 plotted as the signal-versus-chemical shift at 298.34 K.	42
3.6	(a) Working principle of an AFM. (b) Different interaction potentials between the probe atoms and the surface atoms causing different operation modes in an AFM.	43
3.7	Resonance curve of a tapping mode cantilever (a) above and (b) close to the surface. Note that the resonance shifts to lower frequencies and exhibits a drop in amplitude. f_0 is the resonance frequency and ΔA is the change in the amplitude.	46

3.8	Schematic of the different steps in a force–piezo displacement curve: (1) the sample is not in contact with the colloidal probe; (2) the onset of colloidal probe jump–into–contact with the surface; (3) the sample is moved toward the colloidal probe to reach a certain force and the (4, 5) withdraw of sample starts and the colloidal probe undergoes jump–off–contact and (6) again there is no contact between the sample and the colloidal probe. The red lines show the gradient chosen for the sensitivity (α) measurement and the baseline offset for the deflection measurement, respectively. The red lines show the gradient chosen for the sensitivity (α) (20).	47
3.9	D is the actual tip–sample distance. Z_{piezo} is the piezo position. D and Z are not equal because of the cantilever deflection, δ_c , and the sample deformation, δ_s (22).	48
3.10	A schematic illustrating how z_i for calculation of RMS roughness value in eqn. 3.12 is defined.	50
3.11	1-4 shows different steps of a colloidal probe production procedure. . . .	51
3.12	Schematic of the experimental set up to obtain different P/P_{sat} of a ethanol in an AFM liquid cell.	52
3.13	A schematic showing the normal stress (σ), and the shear stresses (τ), acting on a small area of a plane (13).	53
3.14	(a) Schematic of a tensile measurement. $t_0 = 2$ mm and $l_{ini} = 10$ mm are the initial sample thickness and length, respectively. (b) Schematic of compression test. The black arrows show the movements during the experiments.	55
3.15	Schematic of the closed cell designed for SFG experiment.	58
3.16	The schematic plot of the SFG set–up. Both the 10:1 PDMS sample and the gold thin film deposited on a silicon wafer were inside the closed cell. The measurements on gold and 10:1 PDMS samples were performed in air and in a saturated ethanol environment, respectively.	58

3.17	Schematics of an elastically deformed surface indented by a hard sphere in presence of an adsorbate layer either on both surfaces or only on the sphere. The models applied for (a) the analytical approach and corresponding calculations and (b) for the numerical study are compared. The numerical model additionally considers the effect of upward elastic deformation of the soft supports caused by the capillary pressure in the liquid meniscus by a distance D	59
3.18	(a) 3D geometry and (b) the corresponding 2D model. F is external force, $u(x)$ is the displacement, and L_{Tot} is the total length of 2D model (41)	60
3.19	(a) Schematic of the discretization or the approximation of the overall geometry by some simpler geometrical objects. (b) the physical quantities are only solved at nodes.	62
3.20	The spherical shell/elastic support geometry used for FEM simulations. The coordinate axes of r and z are introduced. The axial symmetry is along the latter. The spherical shell is positioned at $(r=0, z=0)$	65
3.21	FEM result showing the deformation of an elastic support ($E = 400$ MPa) due to the indentation of a sphere, here modelled as a shell section. The sphere indentation d is 99 nm and $P/P_{sat} = 0.7$. Thin black lines indicate the non-deformed geometry. The grey shading encodes the normal stress distribution. Dark (negative values) means compressive, bright (positive values) means tensile stress. The highest tensile normal stress (17.5 MPa) occurs in the meniscus area. The zoom-in is a sketch of the deformed surface in the meniscus area (not to scale). The Laplace pressure deforms the surface upward with a value equal to D , on top of the support.	67
4.1	Examples of tapping mode height and phase images recorded from the surface of (a) : 10:1 PDMS and (b) : 20:1 PDMS.	70
4.2	Examples of the tapping mode height and phase images recorded from the surface of (a) : 800 kDa , (b) : 1000 kDa and (c) : 2500 kDa cis-1,4 PI polymer samples.	72

4.3	Force-versus-piezo displacement curves measured on 10:1 PDMS for two different speeds, 0.2 $\mu\text{m/s}$ and 2 $\mu\text{m/s}$, of the cantilever. The hysteresis between the loading and unloading are marked by two arrows in the constant compliance part of the curves. Please note that for the higher cantilever speed, the adhesion force, i.e. the minimum in force-piezo displacement curve, is larger.	74
4.4	The mean values of the adhesion force-versus-different cantilever speeds for (a) 10:1 PDMS and (b) 20:1 PDMS samples. The error bars denote the values of the standard deviation.	75
4.5	The mean values of adhesion force-versus-different cantilever speeds measured in ambient conditions for (a) 800 kDa cis-1,4 PI and 1000 kDa cis-1,4 PI and (b) 2500 kDa cis-1,4 PI polymer samples. The error bars denote the values of the standard deviation.	76
4.6	The mean values of the static adhesion force-versus-dwell time for (a) 10:1 PDMS and (b) different molecular weights of cis-1,4 PI polymer. The error bars denote the values of the standard deviations.	77
4.7	The gold reference spectrum showing the spectral profile of the IR pulse.	79
4.8	The SFG signals obtained from 10:1 PDMS for four polarization combinations. The first, second, and third letter in the polarization combination give the polarization of the SFG, VIS, and IR beams, respectively. .	79
4.9	Sum frequency generation spectrum (SSP polarization) of the 10:1 PDMS sample surface without and with flushing of ethanol vapor over it. . . .	80
4.10	Schematic of (a) a hydrophobic as-prepared 10:1 PDMS sample and (b) an O_2 plasma treated 10:1 PDMS with a hydrophilic glassy surface layer of several nano-meter on top. Water molecules readily form hydrogen bonds with the Si-OH groups present on such hydrophilic layer.	81
4.11	The adhesion force-versus-water P/P_{sat} , measured with a silica microspheres of 2 μm radius on the O_2 plasma treated 10:1 PDMS. The error bars denote the standard deviations found in 420 times repeated measurements at each P/P_{sat}	82

LIST OF FIGURES

4.12	Schematic of the proton exchange mechanism between a silica micro-sphere of 2 μm radius and the O_2 plasma treated 10:1 PDMS. The hydrogen protons dissociate from the silica micro-sphere surface and attach to the O_2 plasma treated 10:1 PDMS surface.	83
4.13	Adhesion force-versus- P/P_{sat} of ethanol, measured with silica micro-sphere of 2 μm radius on naturally oxidized Si wafers.	85
4.14	Ratio of physisorbed layer thickness h' on Si wafer surface to meniscus radius r in dependence on relative vapor pressure. Calculations were done for a silicon wafer surface in presence of an ethanol vapor. The meniscus radius (r) is calculated from Kelvin equation using eqn. 4.3 and h' is calculated from eqn. 2.36.	86
4.15	Adhesion force-versus- P/P_{sat} of ethanol, measured with silica micro-spheres of 2 μm radius on (a) the 10:1 PDMS and (b) the 20:1 PDMS samples. The error bars denote the standard deviations found in 560 times repeated measurements at each constant P/P_{sat}	87
4.16	Schematic of a system in equilibrium with ethanol vapor consisting of (a): a colloidal probe and a soft sample with the ethanol adsorbate layer only on colloidal probe and (b): a colloidal probe and a Si wafer with the ethanol adsorbate layer on both. Note that the adsorbate layer thickness is not to scale.	88
4.17	Adhesion force-versus- P/P_{sat} of ethanol, measured with silica micro-sphere of 2 μm radius on (a) 800 kDa, (b) 1000 kDa and (c) 2500 kDa cis-1,4 PI polymer samples.	90
4.18	The adhesion force measured on the 2500 kDa cis-1,4 PI polymer sample in the liquid ethanol.	92
4.19	SEM images from the probes used for the adhesion-versus- P/P_{sat} of ethanol on the (a) 10:1 PDMS, (b) 800 kDa cis-1,4 PI polymer, (c) 1000 kDa cis-1,4 PI polymer samples and (d) naturally oxidized Si wafer.	92
4.20	A small roughness compared with the meniscus radius, r , on the colloidal probe may result in a big change of the meniscus shape, the area over which the Laplace pressure acts (changing πl_2 to πl_1) and also the contact angle (60).	93

4.21	Comparison between FEM simulation results and analytical calculations (eqn. 2.61) of adhesion force-versus- P/P_{sat} for (a) 170 GPa and (b) 400 MPa elastic supports with (■, -) and without (□, -) presence of an ethanol adsorbate layer on both, surface and colloidal probe. The dotted line is the exact analytical solution of the capillary force-versus- P/P_{sat} of ethanol between a perfectly hard micro-sphere and a perfectly hard support without any deformation.	95
4.22	(a) simulation results of total force-versus indentation for elastic supports with different elastic moduli at $P/P_{sat} = 0.7$. For softer materials the equilibrium indentation as well as adhesion force is higher. (b) Upward surface deformations (D in Fig. 3.17. b) versus r coordinate axis for a fixed indentation of 10^{-4} nm. Surface deformation increases with decreasing elastic modulus. The rising edge is defined by the indenting micro-sphere. The apparent deviation from is only due to different scaling of the axes.	98
4.23	(a) Comparison of analytical solution (eqn. 2.60) and FEM model results of δ_{min} (indentation at which the force-versus-indentation curve has its minimum) for different elastic moduli. (b) Comparison of analytical solution of F_{Adh} (using eqn. 2.61) with values obtained from FEM simulations for different elastic moduli at $P/P_{sat} = 0.7$	99

List of Tables

1.1	Different kinds of bio-adhesion mechanisms.	1
2.1	Contact angles and the corresponding degrees of wetting.	23
3.1	Sylgard 184 base and curing agent components.	38
3.2	The calculated meridional radius of meniscus and Laplace pressure at different relative ethanol vapor pressures, P/P_{sat}	66
4.1	RMS roughness calculated from AFM data	71
4.2	Elastic moduli of different (base:curing agent) PDMS samples and did- derent molecular weights of cis-1,4 PI polymer samples.	73
4.3	Values of the hysteresis between the approach and the retract part of the force-versus-piezo displacement curves for different cantilever speeds measured on 10:1 PDMS surface.	75
4.4	Advancing contact angles of ethanol on different samples.	78
4.5	The change of the water ACA on O ₂ plasma treated 15:1 PDMS sample as a result of the sample hydrophobic recovery.	84
4.6	Comparison of different terms of eqn. 4.5 at two different P/P_{sat}	89

Glossary

1. **ACA:** advancing contact angle
2. **AFM:** atomic force microscope
3. **DC:** direct current
4. **DMT:** Derjaguin, Müller and Toporove
5. **FEM:** finite element method
6. **IR:** infrared
7. **JKR:** Johnson, Kendall, and Roberts
8. **NMR:** nuclear magnetic resonance
9. **PDMS:** polydimethylsiloxane
10. **PI:** polyisoprene
11. **RF:** radio frequency
12. **RMS:** root mean square
13. **Sat:** saturation
14. **SEM:** scanning electron microscope
15. **Si:** silicon
16. **SFG :** sum frequency generation
17. **THF:** Tetrahydrofuran
18. **TMS:** Tetrametylsilane
19. **VdW:** van der Waals
20. **VIS:** visible

1

Introduction

1.1 Motivation

Adhesion is the tendency of dissimilar materials to attach together. The forces that cause adhesion are either physical or chemical in nature (14). Chemical interaction involves covalent bonds, ionic or electrostatic bonds, and metallic bonds. Physical interaction involves the hydrogen bonds, van der Waals bonds and wet adhesion caused by a liquid meniscus in contact area between two solid surfaces. Table 1.1 shows several different kinds of adhesion mechanisms originating from surface forces together with their natural bio-adhesion examples.

The focus of this thesis is on the understanding of temporary wet adhesion. Wet adhesion has two main components: capillary forces (or surface tension forces) and Stefan adhesion force (or viscosity force). Amongst animals, the tree and torrent frogs belong to the physiological category of wet adhesion mechanisms using soft effective adhesive pads developed in the course of biological evolution. The surface of their adhesive pads consists of a hexagonal array of flat-topped 10 μm diameter epithelial

Table 1.1: Different kinds of bio-adhesion mechanisms.

Name	Type	Cause	Natural examples
Gluing	permanent	an intermediate solid layer	mussels, Crucifix Frog
Dry adhesion	temporary	vdW and electrostatic forces, griping	gecko and bees, thorn
Suction	temporary	suction	sea star, octopus
Wet adhesion	temporary	an intermediate liquid layer	snails, tree and torrent frogs

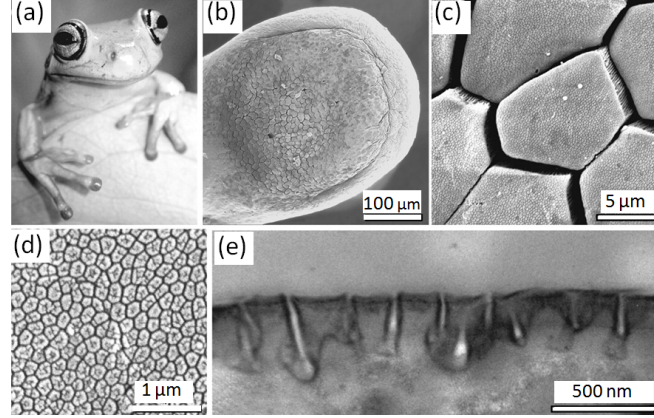


Figure 1.1: Morphology of tree frog toe pads. (a) White's tree frog (*Litoria caerulea*). (b–d) Scanning electron microscope images of (b) a toe pad, (c) epidermis with hexagonal epithelial cells and (d) high power view of the surface of a single hexagonal cell showing peg-like projections. (e) Tunnelling electron microscope image of a cross-section through cell surface (35).

cells separated by 1 μm wide channels and 10 μm deep grooves (Fig. 1.1.c). The surface of each hexagonal cell is not smooth but is covered by a dense array of nano pillars, 300–500 nm in diameter and 300–400 nm in height surrounded by small channels with 40 nm width (Fig. 1.1. d). Pores of mucous glands open into the channels and groves between the hexagonal cells and the mucus spreads over the pads through the channels. Another functionality of such channels at different length scales is to remove any excess fluid as might be encountered by the frogs during the rain fall. In case of tree frogs, the main adhesion contribution is expected to originate from the capillary force (7). In

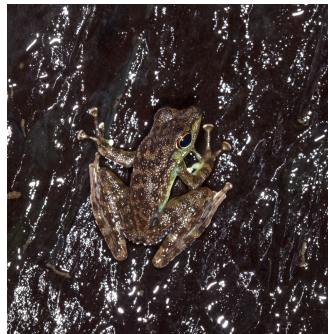


Figure 1.2: A torrent frog clinging to a vertical surface flooded by water. The picture was kindly provided by Jon Barnes group in Glasgow.

addition, the adhesion of torrent frogs is also guaranteed under extreme environmental

1.2 Wet adhesion mechanism of tree frogs – state of art

conditions such as waterfalls (Fig. 1.2).

So far, there is no artificially designed adhesive that combines strong but reversible adhesive properties under different dry (or ambient), wet (after the raining hours) and flooded (in presence of narrow streams of water running on the surface) conditions as the tree and torrent frogs do.

In fact, the adhesion mechanism in tree and torrent frogs is a compromise between adhesion and locomotion. Adhesion exists when it is needed together with an easy release mechanism when the animal needs to take a step. Therefore, the understanding of tree frog adhesion and subsequent development of adhesives inspired by tree frogs will certainly impact a great variety of technological areas. These technological areas include

1. Tire, shoe making and pavement creation industries: for production of safer and non-slippery tires, shoe soles or save pavements.
2. Reversible or permanent bio-compatible plasters for surgery that can adhere to wet tissues during surgery or for wound healing.
3. Adhesive tapes for external prostheses like facial prostheses of ears, noises, and theatrical wigs that they do not fail during application as consequence of skin sweating.

1.2 Wet adhesion mechanism of tree frogs – state of art

Emerson and Diehl (31) were the first to show that the adhesion forces produced by the tree frogs scale with the surface area of their toe pads. They utilised classic formulae for the wet adhesion, applicable to the separation of smooth, rigid plates with both capillarity and transient Stefan forces. Barnes et al. (7) described the capillary force component with the tensile (F_t) and pressure (F_p) forces as (Fig. 1.3)

$$\begin{aligned} F_t &= 2\pi r \gamma \sin \theta_1 \\ F_P &= \pi r^2 \gamma [r^{-1} - (\cos \theta_1 + \cos \theta_2) h^{-1}] \end{aligned} \quad (1.1)$$

where r is the contact area, h is the intermediate fluid thickness and γ is the fluid surface tension. The capillary force is sensitive to the contact angles (θ_1 and θ_2) between the

1.2 Wet adhesion mechanism of tree frogs – state of art

fluid and the two adjoining surfaces.

The transient Stefan adhesion (F_{SA}) is based on the viscosity of the intermediate liquid and is given by (7)

$$F_{SA} = \frac{3\pi r^4 \eta \nu}{2h^3} \quad (1.2)$$

where η is the viscosity of the intervening fluid and ν is the rate of vertical pull. If h , ν and η remain constant then F_{SA} scales with the disk area squared. Since in their experiment, the adhesion force scaled linearly with area rather than area squared, Emerson and Diehl (31) concluded that tree frogs adhered by capillary forces rather than Stefan adhesion. However, for walking frogs or frogs constantly repositioning their pads on a surface, it is expected to provide another effective mechanism.

Barnes et al. (8) also confirmed that tree frogs have area based wet adhesive systems. However, the classic formula for wet adhesion, predicting forces of separation of rigid flat discs, overestimates the adhesion forces that tree frogs produce. Hanna and Barnes (43) reported the maximum adhesion force generated by the tree frogs was 1.2–1.4 mN/mm² for a toe pad with the area of 63 mm² while for a disc with the same area, the maximum wet adhesion is 7 mN/mm². In fact, the equation 1.1 used by Emerson and Diehl and Barnes et al. (7, 31) is only an appropriate simplification of the capillary forces for the structures like tree frog toe pads for which the toe pads are considered totally flat and rigid. Therefore, it is not surprising that the two disk model with intervening liquid gave larger adhesion forces compared to the ones produced by the

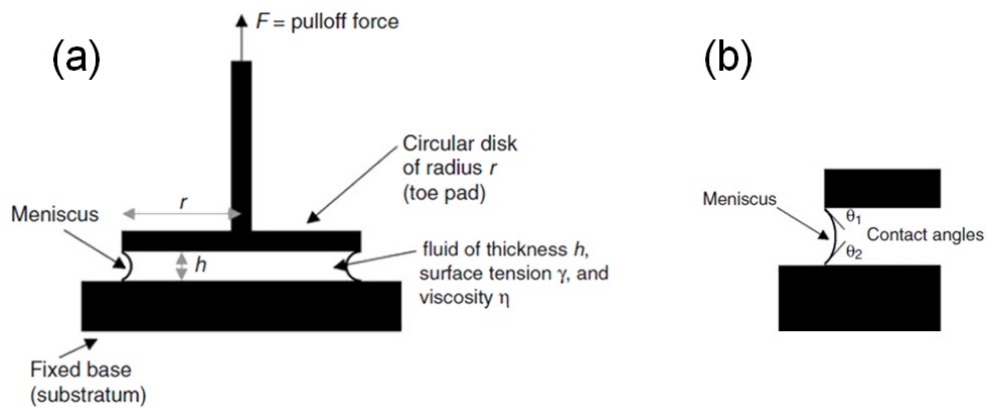


Figure 1.3: (a) A schematic showing different components in a wet adhesion measurement between a smooth solid surface and a disc with radius r . (b) The schematic shows the contact angles (θ_1 and θ_2) between the fluid and the two adjoining surfaces (7).

1.2 Wet adhesion mechanism of tree frogs – state of art

tree frogs.

Moreover, the adhesion force calculated using other contact mechanics models such as Johnson et al. model (49) (a Rigid sphere/rigid plane geometry with attractive van der Waals forces acting in contact area between the sphere and the plane) or peeling models such as Piau et al. model (63) (peeling model for a Newtonian adhesive with a normal traction force of F) predict the scaling of the tree frog adhesion force with toe pads radii and square root of radii, respectively. Both of these results are contradictory with former observations.

Federle et al. (35) measured forces from single toe pads to separate mechanisms of adhesion and friction used by the *Litoria caerulea* frogs. The authors explain their experiment as follows. *Litoria caerulea* frogs were placed in polystyrene Petri dishes (diameter 86 mm, height 17 mm) with 30 holes of 7-10 mm diameter drilled into the bottom. A frog held in the inverted position could easily be made to expose a single toe through one of the holes. By moving the Petri dish attached to a micromanipulator, the toe pads were brought into contact with a 10×12.5 mm glass coverslip mounted on a two-dimensional strain gauge force transducer. The transducer consisted of a phosphor bronze bending beam machined with a 908 twist with two half-bridges of bonded foil strain gauges (BLH Electronics, Heidelberg) to measure normal and shear forces. Friction experiments were conducted by moving the force transducer using a computer-controlled motorized XYZ micromanipulator (M-126, Physik Instrumente). Pad preload was adjusted manually to be approximately 1 mN. A closed loop feed-

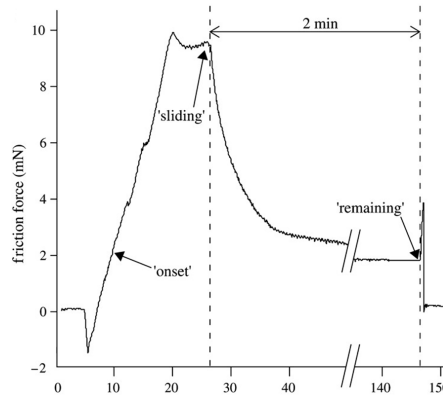


Figure 1.4: Friction force of single toe pads of *Litoria caerulea* during a sliding experiment consisting of 20 s sliding toward the body ($500 \mu\text{m s}^{-1}$) followed by 2 minutes standstill. Shear forces were recorded (i) at the onset of pad sliding; (ii) during steady sliding (at the end of the movement); and (iii) 2 minutes after the movement had stopped (35).

1.2 Wet adhesion mechanism of tree frogs – state of art

back system kept the normal load constant at 0.1 mN during the friction experiment. The glass surface was moved by 10 mm at a constant velocity of 500 $\mu\text{m/s}$. Shear forces were recorded (i) at the onset of pad sliding, (ii) during steady sliding (at the end of the movement), and (iii) 2 minutes after the movement had stopped (see Fig. 1.4). To assess the possibility of very slow, residual sliding after the end of the motor movement, the pad position was measured during the 2 minutes after the motor had stopped and performed a second order polynomial fit. The glass surface was carefully cleaned with distilled water and acetone using lens paper after each trial to remove any mucus residues. An ultrasonic humidifier (Honeywell, BH-860 E) was used to perform the measurements at greater than 80% air humidity (20° C). To calculate shear stress (the ratio of shear force and contact area) the contact area of the toe pads was measured during the force measurements, using reflected light video images (34). From this study, Federle et al. (35) demonstrated that toe pads generate static friction (Fig. 1.4).

Recently, Endlein et al. (32) also confirmed that the adhesion forces generated by the tree frogs toe pads on a surface are the combination of both wet adhesion and the friction forces between the toe pads and the surfaces that they adhere to.

The mechanical properties of tree frogs toe pads were also examined. A micro-indentation tests using 1.5 mm radius sapphire sphere on tree frog toe pads up to an indentation depth of 350 μm yielded elastic moduli of 4–25 kPa, making them the softest known

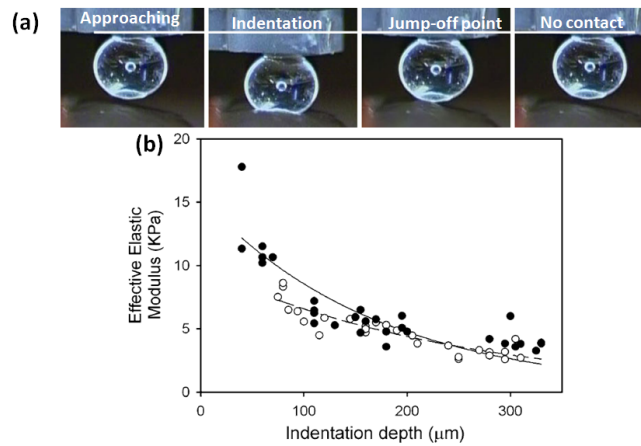


Figure 1.5: (a) Images of indentation with the 1.5 mm-diameter sapphire sphere. (b) Effects of indentation depth on effective elastic modulus, open and filled circles represent data from the two mature adult frogs, frogs 1 and 2, respectively. The data were fitted by exponential curves of the form $y = y_0 + ae^{-bx}$ (9).

adhesion organs of all animals (Fig. 1.5). Previous work using an atomic force microscope as a nano-indenter tool indicated that the outer, 10–15 μm thick, keratinised layer of tree frog toe pads has a modulus of elasticity equivalent to 5–15 MPa (66). It is hypothesized that the outermost layer is stiffer to increase abrasion resistance. It was also observed that the toe pads stiffness (elastic modulus) is lower for the older tree frogs with higher masses. Therefore, understanding the role of softness on capillary adhesion forces in tree frogs in presence of a meniscus would help to figure out the functionality of such soft adhering pads.

1.3 Aim and objectives

So far the role played by the soft, elastic flat surfaces on capillary forces has not been clarified in general. This is also relevant for tree frogs because they have very soft toe pads and use mainly capillary forces to adhere to different surfaces. Therefore, in this thesis a model system is developed to study specifically the effect of capillary forces on the soft and hard surfaces. The model system is defined based on the sphere/plane geometry with a hard sphere in contact with either a hard or a soft half-space planar surface (the so-called support). There is a liquid meniscus in the contact area between the sphere and the support. The meniscus is considered to be formed under thermodynamic equilibrium conditions from the capillary condensation of a liquid in the contact area between the sphere and the support. In such a case, the meniscus radius increases with the relative partial vapor pressure, P/P_{sat} , of liquid (P is the liquid vapor pressure and P_{sat} is the saturation vapor pressure). Some main characteristics of the applied model system are

1. There is not any specific structure on the surfaces in the sphere/plane geometry.
2. The only force considered between the sphere and support is the capillary force.
3. The solid surfaces are considered perfectly smooth and without any surface roughness.
4. The liquid contact angles with both surfaces, sphere and support, are zero.

Up to now, several studies have addressed the effect of a meniscus formed via capillary condensation in presence of small elastic deformations in different contact geometries.

Fogden and White (37) used Hertzian elastic contact mechanics. They used the Kelvin equation (68) to calculate the meniscus radius of curvature. By substituting the meniscus radius of curvature in the Young–Laplace equation (52, 82) the capillary adhesion forces between hard contacting spheres were analyzed. Neglecting the effect of capillary force in the contact zone, they confirmed that F_{Adh} is proportional to the sphere radius. Xue and Polycarpou (79) used the Hertz contact mechanics together with capillary force calculations in a numerical approach, accounting for the effects of both elastic and plastic deformations. They presented a meniscus model for a deformable sphere on a rigid flat surface from non-contact to a fully plastic contact regime. For the elastic contact, the real contact area, the deformed sphere profile, and the projected meniscus area were all determined by the Hertz contact mechanics model. For elastic–plastic contact, a finite element–based spherical solution was used to calculate the real wetted area and meniscus force. The model predicted that due to the spherical deformation, the meniscus force increases with the indentation of sphere.

Butt et al. (21) developed an analytical model along the lines of the numerical study by Xue and Polycarpou and studied the effect of elastic deformation in the presence of capillary forces on adhesion force for the hard sphere/hard sphere geometry.

In all the studies mentioned above, the possible presence of an adsorption layer of liquid molecules that is in equilibrium with the vapor phase and its effect on capillary condensation had been ignored. Kim et al. (4) incorporated equilibrium vapor adsorption for alcohols and analyzed the capillary forces for the sphere/plane geometry. They demonstrated that the presence of an equilibrium adsorption layer of liquid on the solid surfaces has two effects. First, the projected meniscus area is increased. Second, the capillary force becomes strongly vapor pressure dependent, i.e. the adhesion force depends on partial vapor pressure, P/P_{sat} , of the alcohols. Charlaix et al. (25) included vapor adsorption to extend the exact calculation of pendular ring meniscus and calculated capillary adhesion force between hard SiO_2 spheres in sphere/sphere geometries. Their experimental results matched very well with their theoretical work only with incorporating vapor adsorption for the alcohols.

In this thesis, three different approaches i.e. analytical approach, experiments and finite element method (FEM) simulations are applied to study the combined effect of the elastic surface deformability and the presence of an adsorption layer on the capillary force for sphere/plane geometry.

1.4 Overview of thesis

Chapter two contains the introduction of basic terms and theories needed to describe van der Waals forces, solid surface energy, Hertz contact mechanics model and capillary forces. Then, a new analytical model based on the model used by Butt et al. (21) is introduced. This new analytical model accounts for both possible presence of physisorbed layers of liquid on the surfaces prior to capillary condensation and the surface deformation of the planar surface for a sphere/plane geometry. In this model, the increase of the wetted area is due to a Hertzian contact deformation.

Chapter three contains the materials, techniques and methods used in this thesis. It starts with describing the preparation of samples and introduces the experimental techniques used to characterize the prepared samples. Various techniques used in this thesis are nuclear magnetic resonance (NMR), adhesion measurements using atomic force microscope (AFM) both in ambient conditions and in different well-controlled vapor pressure environments of a liquid, sum generation frequency spectroscopy (SFG), contact angle measurements as well as tensile and compression tests. These measurements provided enough data for defining the analytical models which were later implemented in finite element method (FEM) simulations.

Later in this chapter, a model example is solved to introduce the finite element method simulation used for numerical modelling in this thesis. Then, the finite element method (FEM) model developed in this thesis for the detailed studies of Laplace pressure effect on the soft surfaces is introduced. In fact, while the analytical model introduced in chapter two only considers a Hertzian contact deformation, the FEM simulations also account for surface deformations within the meniscus area due to the Laplace pressure induced by a small meniscus radius (large curvature). In such a case, the additional surface deformation leads to a higher indentation of the sphere onto the soft elastic support and therefore a larger contact area forms.

Chapter four starts with presenting the experimental results obtained from adhesion measurements of 2 μm silica micro-spheres on soft polymer surfaces. These experiments were first carried out under ambient conditions to characterize interactions that were not due to capillary forces. Further, the capillary adhesion force were measured between 2 μm silica micro-spheres and different soft and hard surfaces mainly in well-controlled vapor pressure of ethanol. Later in this chapter, the analytical approach as

well as the finite element simulations are compared with the experimental results.

Finally, in **chapter five** a general conclusion summarizes the main results from this research, explains their relevance for tree frogs and presents some perspectives for future research.

2

Basics, principles and analytical models

In this thesis, the capillary adhesion force for a sphere/plane geometry in the presence of an ethanol meniscus is studied. Within the meniscus area, the van der Waals (vdW) forces are shielded by the ethanol and there is a strong capillary force. Yet, the presence of vdW forces in the dry contact area between the sphere and plane cannot be ruled out. Therefore, this chapter starts with the introduction of vdW forces.

2.1 Van der Waals interaction between the molecules

Van der Waals force is an intermolecular force that creates attractive or repulsive interactions between different types of molecules in various environments. Using the average value for random orientation (and not for arrangement along a line as in Fig. 2.1), the three different contributions of vdW force are

1. **Keesom interaction:** it describes the dipole–dipole interactions between the molecules with permanent dipole moments (Fig. 2.1). If the dipoles are free to move, they have the maximum interaction when they are parallel. The dipoles attract each other and tend to orient with their opposite charges facing each other. On the other hand, thermal motion will lead to orientational fluctuations of the dipoles, which reduces their average interaction. For the calculation of the net interaction, one has to do a weighted averaging over all orientations. The

2.1 Van der Waals interaction between the molecules

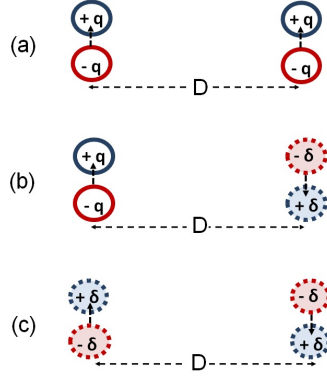


Figure 2.1: (a) Keesom dipole–dipole interaction, (b) Debye interaction between the dipole–induced dipole, and (c) the London dispersion interaction between the induced dipoles–induced dipoles in the molecules. D is the distance between two molecules.

Helmholtz free energy for the Keesom interaction between the molecules is then (50)

$$V = -\frac{\mu_1^2 \mu_2^2}{3(4\pi\epsilon_0)^2 k_B T D^6} = -\frac{C_K}{D^6} \quad (2.1)$$

where μ is the dipole moment, ϵ_0 is the vacuum permeability, k_B is the gas constant, T is the temperature and D is the distance between the two dipoles.

2. **Debye interaction:** it describes the interaction between a molecule with permanent dipole moment and another molecule with induced dipole moment (Fig. 2.1). The Helmholtz free energy for the Debye interaction between two molecules is (19)

$$V = -\frac{\mu^2 \alpha}{(4\pi\epsilon_0)^2 D^6} = -\frac{C_D}{D^6} \quad (2.2)$$

where μ is the permanent dipole moment and α is the polarizability of the molecule without a dipole moment. The Debye interaction also exists between two *identical* polarizable molecules with permanent dipole moments. In this case, eqn. 2.2 is multiplied by a factor of two.

3. **London or dispersion interaction:** it describes the interaction between two molecules with the induced dipole moments (Fig. 2.1). It is a weak force which originates from quantum mechanical fluctuations of the charge distribution of the interacting molecules that do not have permanent dipoles. For two molecules with the ionization energies $h\nu_1$ and $h\nu_2$, the Helmholtz free energy of the dispersion

2.2 Van der Waals interaction between macroscopic objects

interaction can be approximated by (56)

$$V = -\frac{3}{2} \frac{\alpha_1 \alpha_2}{(4\pi\epsilon_0)^2 D^6} \frac{h\nu_1 \nu_2}{(\nu_1 + \nu_2)} = -\frac{C_L}{D^6} \quad (2.3)$$

The dispersion interaction increases with polarizabilities of two molecules, α_1 and α_2 . Optical properties enter in form of the frequencies of the excitation energies i.e. ν_1 and ν_2 . The dispersion interaction also exists along with the Keesom and the Debye interactions.

The van der Waals interaction between molecules is the summation of Keesom, Debye and London dispersion interactions given as

$$V_{vdW}(D) = -\frac{C_{vdW}}{D^6} \text{ with } C_{vdW} = C_K + C_D + C_L \quad (2.4)$$

C_{vdW} is the material specific constant. According to eqn. 2.4, the vdW potential energy between molecules decays with D^{-6} where D is the distance between them.

2.2 Van der Waals interaction between macroscopic objects

2.2.1 Hamaker microscopic approach

The microscopic approach for description of vdW forces between macroscopic bodies was developed by Hamaker (42). Hamaker assumed that the dipole interaction between a pair of molecules is not affected by the presence of a third molecule with permanent or induced dipole moment. This so-called pairwise additivity provides an approximated solution which is only qualitatively matching the exact solution. But, it is instructive because

1. It allows learning about the change of the distance dependence depending on the shape/size of the objects.
2. It allows simple derivation of analytical equations.
3. The Hamaker constant is introduced in this approach.

The potential energy of vdW interaction between two molecules A and B is given by equation 2.4. Now consider two infinite planar solids made from molecules A and B,

2.2 Van der Waals interaction between macroscopic objects

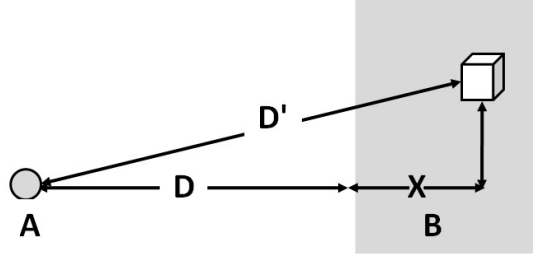


Figure 2.2: Geometry for calculation of the vdW force between molecule A and planar surface made from molecules B (19).

respectively. In order to calculate the vdW interaction between these two macroscopic planar solids, first the vdW interaction energy between molecule A and all molecules in infinite planar surface made from molecules B are summed up as (19)

$$\begin{aligned} V_{MolA/PlaneB} &= -C_{AB} \iiint_V \frac{\rho_B}{D'^6} dV \\ &= -C_{AB}\rho_B \int_0^{+\infty} \int_0^{+\infty} \frac{2\pi r dx dr}{[(D+x)^2 + r^2]^3} = -\frac{\pi \rho_B C_{AB}}{6D^3} \end{aligned} \quad (2.5)$$

The important point is that for this molecular/plane geometry (Fig. 2.2), the vdW interaction potential is now a function of D^3 and not D^6 . Next, the vdW potential per unit area between two infinitely extended planar solids made from molecules A and B at a distance D from each other is calculated as

$$\begin{aligned} \frac{V_{PlaneA/PlaneB}}{A} &= \frac{V}{A} = -\frac{\pi C_{AB}\rho_B}{6} \int_0^{+\infty} \frac{1}{(D+x)^3} dx \\ &= -\frac{\pi C_{AB}\varrho_A\varrho_B}{12D^2} \end{aligned} \quad (2.6)$$

With the definition of Hamaker constant as

$$A_H = \pi^2 C_{AB}\varrho_A\varrho_B \quad (2.7)$$

One gets

$$\frac{V_{PlaneA/PlaneB}}{A} = -\frac{A_H}{12D^2} \quad (2.8)$$

which has D^2 dependence. Figure 2.3 shows the vdW potential interactions between macroscopic objects with different geometries including the sphere/plane geometry. For

2.2 Van der Waals interaction between macroscopic objects

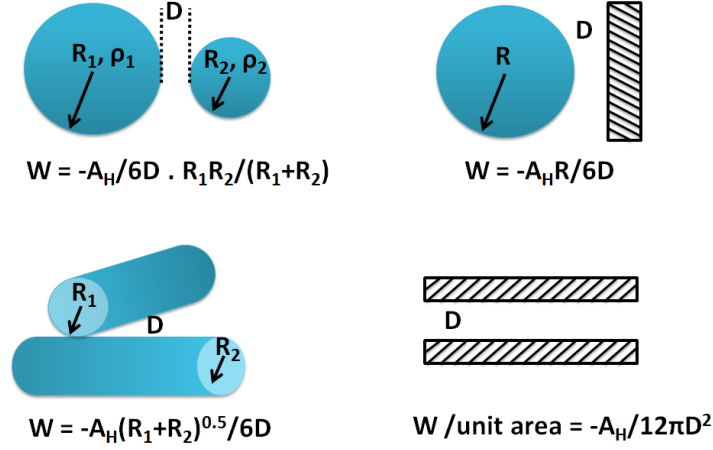


Figure 2.3: Van der Waals potential energy between different macroscopic objects (47).

all four cases shown in figure 2.3, the vdW interaction dependence on the distance is significantly different from the D^{-6} for the molecular interaction. In fact, for macroscopic objects, the vdW force can reach to a significant value if D is small. This is also in principle true for molecules, since for $D^{-6} > 0$, one also gets large values of van der Waals forces. Only the distance dependence is steeper.

2.2.2 Lifshitz theory

The assumption of the Hamaker pairwise additivity ignores the existence of multiple interactions between the molecules. In order to illustrate this fact, consider three neutral molecules, labelled as 1, 2, and 3. At a sufficiently close distance, molecule 1 induces a dipole moment in the molecule 2. The induced dipole moment of 2 induces a dipole moment in the molecule 3 which is close to that. It then means that the electric field of molecular 1 reaches to the molecular 2 directly and to the molecule 3 via induction of the molecule 2. The Hamaker pairwise additivity considers only the direct influences of molecular electric fields and not the influences of the induced molecular electric fields. Instead, Lifshitz theory (55) is a continuum theory that calculates the Hamaker constant based on all kinds of molecular interactions between two dielectric half-space parallel planes made from materials 1 and 2 separated by a distance D in vacuum. This theory was extended together by Dzyaloshinskii and Pitaevskii (29) to include the effect of the third dielectric material filling the gap between the plates (Fig. 2.4). Tabôr and Winterton (72) used the following approximation to calculate the Hamaker

2.2 Van der Waals interaction between macroscopic objects

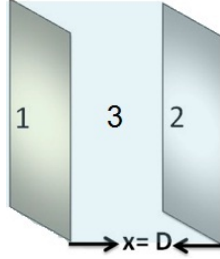


Figure 2.4: Two parallel planar half-spaces made from the materials 1 and 2, respectively. The distance between the two parallel half-spaces, D , is filled with the material 3.

constant, A_H between two parallel half-spaces of materials 1 and 2 separated by a distance D filled with the material 3 as

$$A_H \approx \frac{3}{4}kT\left(\frac{\varepsilon_1 - \varepsilon_2}{\varepsilon_1 + \varepsilon_3}\right)\left(\frac{\varepsilon_2 - \varepsilon_3}{\varepsilon_2 + \varepsilon_3}\right) + \frac{3\hbar v_e}{8\sqrt{2}} \frac{(n_1^2 - n_3^2)(n_2^2 - n_3^2)}{\sqrt{n_1^2 + n_3^2} \cdot \sqrt{n_2^2 + n_3^2} \cdot (\sqrt{n_1^2 + n_3^2} + \sqrt{n_2^2 + n_3^2})} \quad (2.9)$$

where n_i is the refractive index, ε_i is the dielectric constant, and v_e is the plasma frequency of 3×10^{15} Hz. In such a configuration, the materials 1 and 2 interact with exchanging of virtual photons produced by the electromagnetic fluctuations. If the refractive index of the material 3 is larger than one, the virtual photons have to travel through a longer optical path, which means a larger physical distance and therefore, the interaction forces are reduced.¹

The main finding using Lifshitz theory is that the form of the equations derived from Hamaker approach are still valid. But now the Hamaker constant should be determined from the magnetic and electric properties of materials and could be either positive or negative depending on the exact combination of materials.

2.2.3 Retarded van der Waals forces

The finite velocity of light affects the vdW interaction and leads to the so-called retardation phenomena. Effects of retardation should be considered when the separation between the interacting bodies are larger than 10 nm. The retardation effect can be discussed by the following example. Consider the half-space plane 1/half-space plane 2

¹Equation 2.9 is an approximate equation to estimate the Hamaker constant. For exact calculations of Hamaker constant, the full spectral method (38) together with spectroscopic data about the frequency dependent dielectric function must be used.

2.3 Free surface energy theory of adhesion

geometry with 1 and 2 indicating materials 1 and 2, respectively. The D^{-2} dependence of the vdW interaction for this geometry is only valid for small distances of D . When D is larger than 5–10 nm, the finite speed of the virtual photons lead to the retardation. It means that the time for electric field of plate 1 to be influenced by the plate 2 and return back to the plate 1 is comparable with the fluctuation period of dipole moments in the plate 1. In this case, only the London interaction is affected and the interaction decay is faster than D^{-2} . In order to establish the retarded vdW interaction with the dependency of vdW interaction on D , eqn. 2.8 changes to (19)

$$\frac{V_{PlaneA/PlaneB}}{A} = -\frac{A_H}{12D^n} \quad (2.10)$$

The result of eqn. 2.10 is that the Hamaker constant, A_H , depends on the distance. This leads to a steeper distance dependence for an intermediate range with $n = 3$. At distances larger than the thermal de Broglie wavelength of $\Lambda = 7.8 \mu\text{m}$, only the contribution of the static polarizability remains. Then we have the original value of the exponent ($n = 2$) but a smaller value of A_H with only the first term of eqn. 2.9 remaining.

2.3 Free surface energy theory of adhesion

As the detailed calculation of van der Waals forces is difficult, generally a simpler approach based on the concept of free surface energy is used (14). If one cleaves a crystalline solid like mica along its cleavage plane, two highly chemically active surfaces are generated. The cleavage process causes the fracture of cohesive bonds across the cleavage interface. These fractured bonds leave the surface in a highly energetic state which means that the energy which is normally associated with bonding to other atoms (like in the bulk solid) is now available at the atoms on the surface. This energy which is required to create a new surface is called free surface energy.

Free surface energy influences the probability of adhesive bonds formation for the solids which are in contact. When a contact is formed between two materials with free surface energies of γ_1 and γ_2 , the surface energy of the two interfaces per unit area changes to the interfacial surface energy of γ_{12} . The work of adhesion or the energy of adhesion

per unit area is defined as (6, 16)

$$W_{1,2} = \Delta\gamma = \gamma_1 + \gamma_2 - \gamma_{1,2} \quad (2.11)$$

where $\Delta\gamma$ is equal to the reduction in the surface energy by the formation of interface in mJ/m^2 . In other words, $\Delta\gamma$ is the energy needed to separate a unit area of the interface or to create new surfaces. For two identical materials, $\Delta\gamma$ becomes the work of cohesion, and is equal to 2γ . The important thermodynamic relation in eqn. 2.11 is valid for both solid and liquid interfaces. The only difference is that γ is generally called free surface energy for solids and surface tension for liquids.

2.4 Contact mechanics

Consider a hard elastic sphere which is in contact with an elastic half-space planar support, as shown in Fig. 2.5.a–b.

When there are neither external loads on the sphere nor the attractive surface forces in the contact area between the sphere and the support, a point-like contact forms (Fig. 2.5.a). In this case, if an external force is applied on the sphere, Hertz contact mechanics model will be used to calculate the contact radius formed between the sphere and support, indentation of sphere onto the support and also the pressure distribution in contact area.

However, when there are no external loads on the sphere but the attractive surface forces are present in the contact area, a finite contact radius is formed such that there is an energy balance between the released surface energy and the stored elastic energy

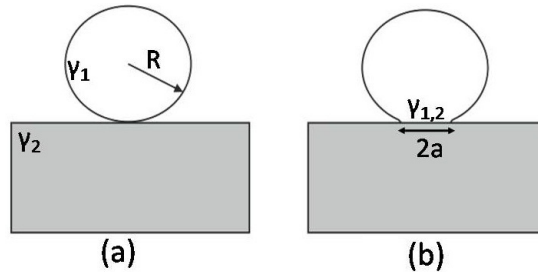


Figure 2.5: Contact between a hard sphere and an elastic surface with no applied force: (a) in the absence of attractive forces between the two bodies, (b) in the presence of attractive forces, surfaces are drawn together to make contact over a circle of radius a (14).

around the interface (Fig. 2.5.b). The loss in free surface energy E_s is given by (14)

$$E_s = -\pi a^2 \Delta\gamma \quad (2.12)$$

The attractive force F_s associated with this energy is

$$F_s = -\frac{dE_s}{d\delta} \quad (2.13)$$

where δ is the normal indentation which can be substituted from Hertz model to determine F_s . In presence of an external load, a modified Hertz contact mechanics must be used to calculate the contact radius formed between the sphere and the support, indentation of the sphere onto the support and the pressure distribution in the contact area.

In this thesis, it is assumed that there are no attractive forces between the sphere and the support. Therefore, in presence of an external load, the Hertz contact mechanics model is used to describe the deformation of support as a result of sphere indentation onto it.

2.4.1 Hertz model

The problems of the elastic contacts for sphere/sphere and sphere/plane geometries were solved by Hertz in 1882 (59). The main assumptions in this contact mechanics model are

1. Surfaces are continuous, smooth and elastic.
2. The strains are small and within the elastic limit.
3. The contact radius is much smaller than the characteristic radius of bodies.
4. The contact is frictionless.
5. There are no surface forces in the contact area.

For a sphere/sphere geometry with an applied load, F_{ext} , Hertz derived an equation for the contact radius, a , between the spheres as

$$a^3 = \frac{3F_{ext}R^*}{4E^*} \quad (2.14)$$

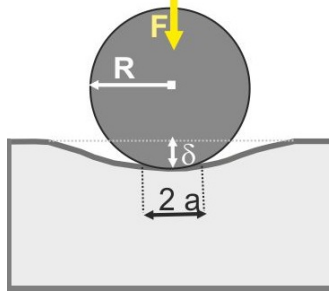


Figure 2.6: Schematic of a sphere/plane geometry. A hard sphere is indenting an elastic half-space support. F is the external load, a is the contact radius and δ is the indentation of hard sphere onto the elastic support.

E^* and R^* are the reduced elastic modulus and the reduced radius, respectively. For the contact between material 1 and 2, with elastic moduli E_1 and E_2 and Poisson ratios of ν_1 and ν_2 , R^* and E^* are defined as

$$\frac{1}{R^*} = \frac{1}{R_1} + \frac{1}{R_2} \quad (2.15)$$

and

$$E^* = \left(\frac{1 - \nu_1^2}{E_1} + \frac{1 - \nu_2^2}{E_2} \right)^{-1} \quad (2.16)$$

The indentation, δ , is given by

$$\delta = \frac{a^2}{R^*} = \left(\frac{9F_{ext}^2}{16E^{2*}} \right)^{1/3} \quad (2.17)$$

According to eqn. 2.17, the contact area, πa^2 increases as $F_{ext}^{2/3}$. Moreover, the relation between external force and the corresponding indentation, δ , is

$$F_{ext} = \frac{4}{3} E^* \sqrt{R^*} \delta^{3/2} \quad (2.18)$$

For a sphere/plane geometry (Fig. 2.6) with an elastic support made from material 1 and a rigid sphere made from material 2, E^* simplifies to

$$E^* = \frac{E_1}{1 - \nu_1^2} \quad (2.19)$$

and R^* to

$$R^* = R_1 \quad (2.20)$$

because the radius of a planar support is infinite. In this case the vertical displacement of the elastic support outside the contact area and for $r > a$ is

$$\Delta z(r) = \frac{a^2}{\pi R_1} \left[\sqrt{\frac{r^2}{a^2} - 1} + \left(2 - \frac{r^2}{a^2}\right) \arcsin \frac{a}{r} \right] \quad (2.21)$$

In addition, the normal stress distribution in the contact region has an elliptical shape which can be described as

$$\sigma_z = \frac{3F_{ext}}{2a\pi} \sqrt{1 - \frac{r^2}{a^2}} \quad (2.22)$$

from which the maximum pressure at $r = 0$ is

$$p_{max} = \frac{3F_{ext}}{2a\pi} = \frac{3}{2}P_0 \quad (2.23)$$

where P_0 is the average contact pressure. The contact stiffness can be also obtained from the slope of $F_{ext}(\delta)$ as

$$\frac{dF_{ext}}{d\delta} = 2E^*a \quad (2.24)$$

For derivation of all above equations, it is assumed that $a \ll R$. The indentation of a rigid sphere into an elastic support without the condition of $a \ll R$ was studied by Sneddon (69) and Ting models (73).

Later, Johnson, Kendall, and Roberts added the additional adhesive forces inside the contact area (Fig. 2.5.b) to the Hertz contact mechanics model (the so-called JKR model). Further, Derjaguin, Müller and Toporove used the Hertz model for description of the contact area between two spheres but incorporated the surface forces outside of the contact region (the so-called DMT model) (26).

The JKR analysis is used if the elastic deformation of the surfaces, δ_a , caused by the surface forces is large compared with their effective range of action, h_a . Johnson and Greenwood (48) gave the following criteria for the start of JKR model zone

$$\left| \frac{\delta_a}{h_a} \right| = 20 \quad (2.25)$$

whereas the DMT model is valid when the elastic deformation due to adhesion forces, δ_a , is small compared with their effective range of action, h_a . The Johnson and Green-

woods' criteria for the validity of DMT zone is (48)

$$\left| \frac{\delta_a}{h_a} \right| \leq 0.05 \quad (2.26)$$

In this thesis, the Hertz contact mechanics is applied as an approximation model for describing the contact between 2 μm micro-spheres and different hard and soft elastic supports. The capillary forces produced from a liquid meniscus are introduced outside of the contact area between the sphere and the support. The aim is to study how the capillary forces affect elastic supports with different elastic moduli.

2.5 Capillary forces

In micro- and nano-meter scale the capillary forces originate from the presence of a small liquid meniscus in the contact area between two solid objects. In the following sections, several terms as well as the theories developed so far to understand and describe such forces are presented.

2.5.1 Liquid surface tension

Liquid surface tension causes the liquid surface to behave like an elastic surface which is under tension at the liquid-liquid or air-liquid interfaces. It has the unit of $[\frac{N}{m}]$ or $[\frac{J}{m^2}]$. In the microscopic scale, the concept of surface tension at a liquid-air interface can be interpreted as follows. All the molecules in a liquid bulk attract each other by forces such as hydrogen bonding or vdW interactions in all directions. However, the molecules located at liquid-air surface, are only partially surrounded by other liquid molecules and the number of their adjacent molecules are fewer. (Fig. 2.7). This

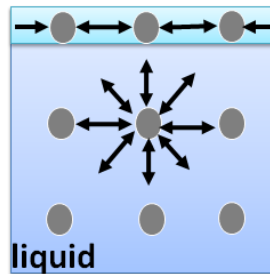


Figure 2.7: Surface tension results from the imbalanced molecular forces at the surface of the liquid. High values of the surface tension means the molecules tend to interact strongly.

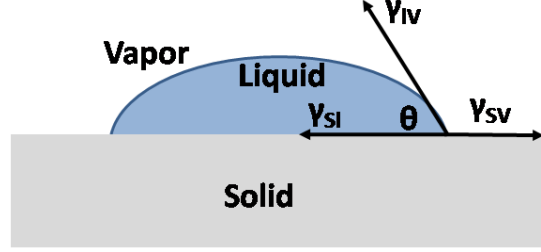


Figure 2.8: A schematic defining the contact angle, θ , of a liquid on a solid surface. θ is the measure of liquid affinity with the solid surface.

is energetically unfavourable and one needs the energy, γ_l , to bring the molecules from the liquid bulk to the surface to produce a new surface. γ_l is called the liquid surface energy. Throughout this thesis however, γ_l is called liquid surface tension rather than liquid surface energy to avoid confusion with the solid surface energy.

Another important term is the so-called liquid contact angle. When a liquid drop is deposited on a planar solid surface, the contact angle between the outline tangent of the drop at contact location and the solid surface, θ , is the measure of a liquid ability to spread on a solid surface (Fig. 2.8). Young equation (44) relates θ to solid surface energy γ_{sv} , liquid surface γ_{lv} and the liquid–solid interfacial surface energy γ_{sl} as

$$\gamma_{sv} = \gamma_{sl} + \gamma_{lv} \cos \theta \quad (2.27)$$

If a liquid forms a contact angle smaller or equal to 90° , the solid surface is called lyophilic. Correspondingly a lyophobic surface exhibits a contact angle larger than 90° . If $\theta = 0$, the liquid spreads over the solid surface and there is a full wetting. Thus contact angle is an inverse measure of wetting (67). Table 2.1 gives the relationship between contact angles and the different wetting degrees.

Table 2.1: Contact angles and the corresponding degrees of wetting.

Contact angle	Degree of wetting
$\theta = 0$	full wetting
$0 < \theta < 90^\circ$	partial wetting
$90^\circ \leq \theta < 180^\circ$	low wetting
$\theta = 180^\circ$	non-wetting

2.5.2 Young–Laplace equation

In equilibrium, if a liquid surface is curved, then there is a pressure difference across it. It can be illustrated by the following example (44). If one takes a tube and closes one end of it with a piece of stretched rubber, the rubber membrane forms a planar surface. It will stay planar as long as there is no pressure difference across it. If the pressure inside the tube increases or decreases, the membrane bulges in and out of the tube, respectively (Fig. 2.9). The same concept holds for a liquid in a tube held in air. The surface tension tends to minimize the surface area and to produce a planar surface. To produce a curved liquid surface, the pressure on one side has to be larger than on the other side. The Young–Laplace (52, 82) equation relates the Laplace pressure difference, ΔP , between the two phases and the surface curvature as

$$\Delta P = \gamma_l \cdot \left(\frac{1}{R_1} + \frac{1}{R_2} \right) \quad (2.28)$$

where γ_l is the liquid surface tension and R_1 and R_2 are the principle radii, respectively. When applying the Young–Laplace equation to the simple geometries, it can be determined at which side the pressure is higher. For example, consider a meniscus in the cylindrical coordinate system with the rotational symmetry (Fig. 2.10). The meniscus is formed in the contact area between a sphere with radius R and a half-space planar solid surface. For a small meniscus with the contact angles of $\Theta_1 = \Theta_2 = 0$ with both the sphere and the planar surface respectively, and principle radii of $R_1 = -r$ and $R_2 = l$, the Young–Laplace equation simplifies to

$$\Delta P = -\frac{\gamma_l}{r} + \frac{\gamma_l}{l} \quad (2.29)$$

$R_1 = -r$ and $R_2 = l$ are counted negative and positive, respectively according to their

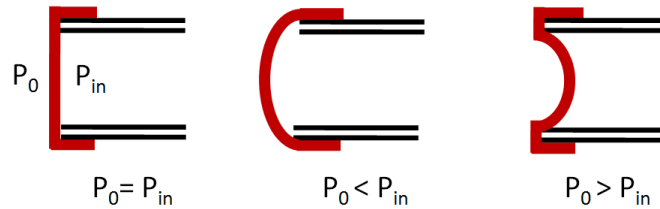


Figure 2.9: An stretched rubber membrane at the end of a cylindrical tube with different inside pressure, P_{in} , compared with the outside pressure, P_0 (44).

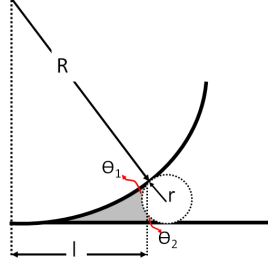


Figure 2.10: A meniscus in cylindrical coordinate system with rotational symmetry. The principle radii of curvature are r and l . The meniscus is formed in the contact area between a sphere with radius R and a half-space planar solid surface. Θ_1 and Θ_2 are the contact angles of liquid with the sphere and plane, respectively.

curvatures with respect to the liquid. As $|l| \gg |r|$, one can ignore $\frac{1}{l}$ which then leads to

$$\Delta P = -\frac{\gamma l}{r} \quad (2.30)$$

Where the pressure difference across the meniscus can simply be calculated by knowing the meniscus curvature radius, r .

2.5.3 Kelvin equation

Kelvin equation (68) relates the vapor pressure of a liquid to its curvature

$$\ln \frac{P}{P_{sat}} = \frac{2v_m}{RT} \cdot \left(\frac{1}{R_1} + \frac{1}{R_2} \right) \quad (2.31)$$

where P is the vapor pressure of the curved surface, P_{sat} is the saturation vapor pressure for a planar surface, γ_l is the liquid surface tension, v_m is the liquid molar volume, R is the universal gas constant, T is the temperature and R_1 and R_2 are the two principle radii of curvature.

One important phenomena explained by Kelvin equation (eqn. 2.31) is the spontaneous condensation from the vapor phase into the curved liquid surfaces even below saturation vapor pressure, the so-called capillary condensation. In order to relate the P/P_{sat} to a meniscus curvature, r , formed from the capillary condensation of a liquid vapor in the contact area between a sphere and a planar surface (Fig. 2.10), Kelvin equation changes to

$$\ln \frac{P}{P_{sat}} = \frac{2v_m}{RT} \left(\frac{1}{l} - \frac{1}{r} \right) \quad (2.32)$$

2.6 Equilibrium vapor adsorption on solid surfaces: liquid physisorption

assuming a meniscus with $|l| \gg |r|$, eqn. 2.32 simplifies to

$$\ln \frac{P}{P_{sat}} = -\frac{2v_m}{RT r} \quad (2.33)$$

from which

$$r = -\frac{2v_m}{RT \ln \frac{P}{P_{sat}}} \quad (2.34)$$

In this study at each P/P_{sat} of ethanol: (i) eq. 2.34 was used to calculate the radius of meniscus curvature, r ; (ii) by substituting r for each P/P_{sat} in eqn. 2.30, the Laplace pressure was calculated; (iii) the capillary force was then obtained by the integration of Laplace pressure over the area, πl^2 , that it acts at each individual P/P_{sat} of ethanol (cf. Fig. 2.10). Nonetheless, in thermodynamic equilibrium conditions, it is also possible to have equilibrium vapor adsorption on the solid surfaces exposed to a specific liquid vapor prior to the occurrence of the capillary condensation.

2.6 Equilibrium vapor adsorption on solid surfaces: liquid physisorption

Consider a solid surface made from molecules A, which is at thermal equilibrium with a gaseous environment containing the molecules B. There is the possibility for the molecules B to adsorb onto the solid surface A (2, 3, 11, 70). In this case, the solid surface is called adsorbent and the gas molecules are adsorbate. If there is only a moderate interaction between adsorbate and adsorbent, i.e., no chemical bonds are formed, we talk about physisorption. Physisorption is characterized by

1. It does not need an activation energy.
2. Its sublimation energy is in the order of 20-40 [kJ/mol].
3. The adsorbate molecules are free to diffuse and rotate on the adsorbent surface.
4. No surface reactions are involved.
5. It is a reversible process which can be controlled by decreasing or increasing the pressure.

2.6 Equilibrium vapor adsorption on solid surfaces: liquid physisorption

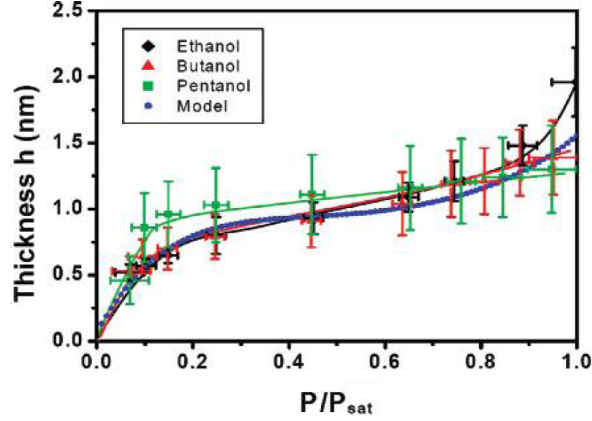


Figure 2.11: The adsorption isotherm for ethanol, 1-butanol, and 1-pentanol as measured by the attenuated total reflectance–IR experiment. The solid blue line is the representative fit for all the three isotherms (4).

At a constant temperature, the thickness of the equilibrium adsorbate layer on the adsorbent surface versus the relative partial vapor pressure, P/P_{sat} , is called an adsorption isotherm (Fig. 2.11).

In this study, the ethanol vapor is in thermodynamic equilibrium with the SiO_2 surfaces such as non-porous SiO_2 colloidal probes and naturally oxidized Si wafers. The physisorption of first ethanol layer starts by forming hydrogen bonds with the pre-adsorbed water on such hydrophilic surfaces (10, 23). The formation of the next ethanol layers occurs as a result of vdW interactions between the ethanol molecules. The following adsorption isotherm introduced by Kim et al. was used to quantify the thickness of ethanol physisorbed layer (4)

$$h'(\frac{P}{P_{sat}}) = (7.03(\frac{P}{P_{sat}})^5 - 22.97(\frac{P}{P_{sat}})^4 + 31.76(\frac{P}{P_{sat}})^3 - 21.40(\frac{P}{P_{sat}})^2 + 7.10(\frac{P}{P_{sat}}) - 0.003)[nm] \quad (2.35)$$

This fifth order polynomial is an empirical equation obtained from the adsorption measurements for different short length alcohols (blue line in Fig. 2.11) on silica surfaces.

2.7 Capillary forces between a rigid sphere and a rigid plane: the influence of physisorbed layers

2.7 Capillary forces between a rigid sphere and a rigid plane: the influence of physisorbed layers

In the so-called circular approximation, the meridional profile of the meniscus is replaced by a circle of fixed radius, r , and the azimuthal radius is l . For each P/P_{sat} of a liquid, r is calculated from the Kelvin equation (eqn. 2.31). In presence of the adsorbate layers on both rigid sphere and rigid planar surfaces, one can relate r and l with the sphere radius R and the adsorbate thickness $h'(P/P_{sat})$ using the Pythagorean relation using

$$[R - h'(P/P_{sat}) + r]^2 + [l - r]^2 = [R + h'(P/P_{sat}) - r]^2 \quad (2.36)$$

Note that r is negative because the center of circle is outside of meniscus whereas $-r$ is a positive value. This equation can be solved for l as

$$l = 2\sqrt{R(h'(P/P_{sat}) - r)} + r \quad (2.37)$$

Once the adsorption thickness, $h'(P/P_{sat})$, is determined experimentally, one can calculate l from eqn. 2.37. Once l is found, then both the axial surface tension force, F_T , the Laplace pressure force, F_P , are calculated as

$$F_T = 2\pi\gamma l \quad (2.38)$$

$$F_P = - \left(\frac{RT}{V_m}\right) \ln \frac{P}{P_{sat}} \pi l^2 \quad (2.39)$$

The importance of incorporating the adsorbate layers can be proved by the following calculations. At $P/P_{sat} = 0.7$ for ethanol, $-r$ and h' are 1.45 nm and 1.04 nm, respectively. For a micro-sphere with $R = 2 \mu\text{m}$, in absence of adsorbed layers

$$\begin{aligned} l = 2\sqrt{(-r)R} + r &= 2\sqrt{1.45 \text{ nm} * 2000 \text{ nm}} - 1.45 \text{ nm} \\ &= 106.25 \text{ nm} \end{aligned} \quad (2.40)$$

whereas in presence of the adsorbed layers

$$\begin{aligned} l = 2\sqrt{R(h'(P/P_{sat}) - r)} + r &= 2\sqrt{(1.45 + 1.04) \text{ nm} * 2000 \text{ nm}} - 1.45 \text{ nm} \\ &= 139.69 \text{ nm} \end{aligned} \quad (2.41)$$

2.7 Capillary forces between a rigid sphere and a rigid plane: the influence of physisorbed layers

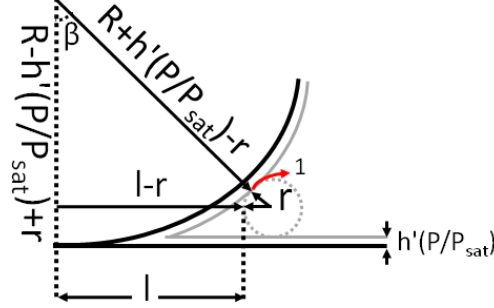


Figure 2.12: Circular approximation where the meridional curvature is replaced with a circle with a fixed radius, r . Note that r is negative because the center of the circle is outside the meniscus; so $-r$ is positive. At the position where r and l (cross-sectional radii) are parallel to the substrate, the Pythagorean theorem can be used to relate R , adsorbate thickness h' , r and l .

Comparing eqn. 2.40 with eqn. 2.41 shows that in the presence of adsorbed layers, the Laplace pressure acts over a larger area and therefore, the Laplace pressure force is larger. Further, in presence of adsorbed layers, the Laplace pressure force depends on P/P_{sat} through the dependencies of both r and h' to it.

Using the formulae in eqs. 2.38 and 2.39, the forces are calculated for the point where r is parallel to the substrate (Fig. 2.12). To calculate the forces at point '1' of Fig. 2.12, the filling angle β is found from

$$\beta = \sin^{-1}\left(\frac{l-r}{r+h'-r}\right) \quad (R-h' > -r) \quad \text{or} \quad (2.42)$$

$$\beta = \frac{\pi}{2} \sin^{-1}\left(\frac{-r-(R-h')}{R+h'-r}\right) \quad (-r > R-h') \quad (2.43)$$

The distance from the z -axis to point '1' is

$$r' = l - r(1 - \sin\beta) \quad (2.44)$$

Therefore, the forces F_T , and F_P change to the following equations

$$F_T = 2\pi\gamma_l r' \sin\beta \quad (2.45)$$

$$F_P = - \left(\frac{RT}{V_m}\right) \ln \frac{P}{P_{sat}} \pi r'^2 \quad (2.46)$$

The difference between F_P calculated from eqn. 2.39 and 2.46 is very little and negligible compared with the typical experimental errors in the AFM measurements (4).

2.8 Capillary force for the deformable surfaces – a simple analytical model

2.8 Capillary force for the deformable surfaces – a simple analytical model

Butt et al. used an approximate analytical approach to calculate the capillary force of water in presence of Hertzian surface deformation for sphere/plane geometry (21). They figured out that the capillary adhesion force for the non-deformable sphere/plane geometry which is (21)

$$F_{adh} = 4\pi\gamma_l R \quad (2.47)$$

where γ_l is liquid surface tension and R is the sphere radius, changes to (21)

$$F_{adh} = 4\pi\gamma_l R + \left(\frac{\pi\gamma_l}{2r}\right)^3 \frac{2R^2}{3E^{*2}} \quad (2.48)$$

where E^* is the elastic modulus and r is the radius of meniscus curvature. According to eqn. 2.48, the capillary force increases more steeply compared to eqn. 2.47 and scales with R^2 . The analytical model of Butt et al. accounted for the surface deformation for a sphere/plane geometry, taking into account the increase of wetted area due to a Hertzian contact deformation. However, it did not include the possible presence of adsorbed layers of a liquid on the contacting surfaces. It is accounted for in the new extended analytical model presented in detail in the next section.

2.9 Capillary force for the deformable surfaces in presence of adsorbed layers – the new analytical model

In general, the capillary force originating from a liquid meniscus in a sphere/plane geometry has two contributions: the surface tensional force F_T which arises from the liquid surface tension that is pulling along the contact line and the Laplace pressure force F_P which is obtained by integrating the Laplace pressure over the area covered by the meniscus. These forces are given by (36)

$$F_T = 2\pi\gamma_l R \sin^2 \beta \quad (2.49)$$

$$F_P = \left(\frac{\gamma_l}{r}\right)\pi R^2 \sin^2 \beta \quad (2.50)$$

R is the radius of sphere, γ_l is surface tension of condensed liquid, β filling angle and r is the meniscus radius (Fig. 2.13). For the case of a meniscus formed by capillary

2.9 Capillary force for the deformable surfaces in presence of adsorbed layers – the new analytical model

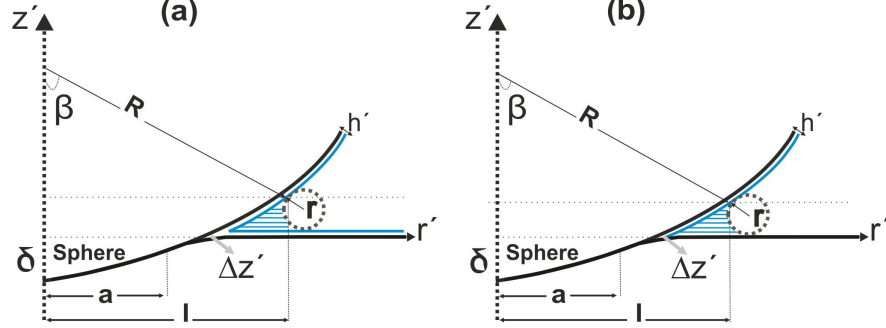


Figure 2.13: Schematic of an elastically deformed surface indented by a hard sphere in presence of a liquid meniscus and (a) adsorbate layers on both surfaces and (b) only on colloidal probe. r' and z' are the axis of the axisymmetric coordinates system. $\Delta z(r')$ denotes the deflection of the surface and is given by the Hertz contact mechanics model.

condensation of a liquid between a micro-sphere in contact with a planar surface, F_P is by far dominating. Therefore, only the Laplace pressure contribution is considered in the following calculations.

Considering the presence of a physisorbed layer of liquid, two different cases can be differentiated. In the first case, physisorption is assumed on both surfaces. This is the relevant case for a silicon wafer interacting with a silica sphere.

In the second case, it is assumed that only the sphere is covered by an ethanol adsorbate layer. The second case is relevant for a silica sphere interacting with the soft polymer samples where the low surface energy of the polymer surface hinders the adsorption. For both models, the analytical expressions of the total force F_{Tot} between the sphere and an elastic support is derived. It is given as the sum of the attractive Laplace pressure force and the elastic restoring forces given by Hertz contact mechanics (21). The meniscus size is derived from the vapor pressure of the liquid via the Kelvin equation. The total force, F_{Tot} , is the function of the indentation, δ , of the sphere onto the elastic support. By finding the minimum of F_{Tot} with respect to δ , the adhesion force between the sphere and the elastic support as well as the corresponding indentation, δ_{min} , are obtained. In all calculations, it is assumed that $\delta \ll R$ and the meniscus contact angle with both the sphere and the planar surface is zero. Besides, in the presence of an ethanol meniscus with the dielectric constant of $\varepsilon = 25.3$, the vdW forces can be simply neglected compared to the meniscus force (19).

2.9 Capillary force for the deformable surfaces in presence of adsorbed layers – the new analytical model

2.9.1 Rigid sphere in contact with an elastic support including physisorbed liquid layers on both surfaces

Consider a rigid sphere indenting an elastic support in the presence of a liquid meniscus (Fig. 2.13). The vertical coordinate is denoted as z' , the radial one as r' . δ is the indentation of sphere onto the elastic support, a is radius of contact, R is the sphere radius and h is the height of meniscus. β is the so-called filling angle. The thicknesses of both adsorbate layers are assumed to be equal; it is denoted as h' . To take advantage of the radial symmetry, cylindrical coordinates are used to calculate the capillary force (58). The curvature of the liquid meniscus is characterized by two radii: the azimuthal radius l and the meridional radius r , perpendicular to it. The total curvature of the liquid is $(\frac{1}{l} - \frac{1}{r})$. The height h of the meniscus can be expressed as

$$\begin{aligned} h &= r(\cos(\beta) + 1) + h' \\ h &= R(1 - \cos \beta) - \delta + \Delta z(l + r) \end{aligned} \quad (2.51)$$

The adsorbate layer only changes the height of meniscus and does not change its curvature.

The shape of the deformed surface is given by the Hertz model and can be described by its deflection Δz from the plane (59)

$$\Delta z(r') = \frac{\delta}{\pi} \left[\sqrt{\frac{r'^2}{\delta R} - 1} + \left(2 - \frac{r'^2}{\delta R}\right) \arcsin \frac{\sqrt{\delta R}}{r'} \right] \quad \text{for } r' \geq a \quad (2.52)$$

where a denotes the contact area radius. Combining eqns. 2.51, 2.52 and approximating $l + r \approx l = (R + h') \sin \beta$, the radius of curvature is given by

$$\begin{aligned} r &= \frac{R(1 - \cos \beta) - \delta - h'}{(1 + \cos \beta)} + \frac{\delta}{\pi(1 + \cos \beta)} \left[\sqrt{\frac{(R + h')^2 \sin^2 \beta}{\delta R} - 1} \right. \\ &\quad \left. + \left(2 - \frac{(R + h')^2 \sin^2 \beta}{\delta R}\right) \arcsin \frac{\sqrt{\delta R}}{(R + h') \sin \beta} \right] \end{aligned} \quad (2.53)$$

2.9 Capillary force for the deformable surfaces in presence of adsorbed layers – the new analytical model

Furthermore, two assumptions are made to simplify the analytical approach. First, it is assumed that $l + r \approx l = R \sin \beta$, which leads to

$$r = \frac{R(1 - \cos \beta) - \delta - h'}{(1 + \cos \beta)} + \frac{\delta}{\pi(1 + \cos \beta)} \left[\sqrt{\frac{R \sin^2 \beta}{\delta} - 1} + \left(2 - \frac{R \sin^2 \beta}{\delta} \right) \arcsin \frac{\sqrt{\delta}}{\sqrt{R \sin \beta}} \right] \quad (2.54)$$

Second, by assuming that $\delta \gg r$ and using the fact that at $r' = a$, $\Delta z = \frac{\delta}{2}$ one can calculate r , the meniscus radius, as

$$r = \frac{R(1 - \cos \beta) - \frac{\delta}{2} - h'}{(1 + \cos \beta)} \quad (2.55)$$

it follows that

$$\cos \beta = \frac{R - r - \frac{\delta}{2} - h'}{(R + r)} \quad (2.56)$$

and

$$\begin{aligned} \sin^2 \beta &= 1 - \cos^2 \beta = 1 - \left(\frac{R - r - \frac{\delta}{2} - h'}{R + r} \right)^2 \\ &= \frac{(2r + \frac{\delta}{2} + h')(2R - \frac{\delta}{2} - h')}{(R + r)^2} \approx \frac{2(2r + \frac{\delta}{2} + h')}{R} \end{aligned} \quad (2.57)$$

The total force acting on the sphere for a given indentation δ is the sum of the restoring elastic force from Hertz contact model (eqn. 2.18) and the Laplace pressure force F_P (eqn. 2.50)

$$\begin{aligned} F_{Tot} &= \frac{4}{3} E^* \sqrt{R \delta^3} - \pi R \frac{\gamma_l}{r} (4r + \delta + 2h') \\ &= \frac{4}{3} E^* \sqrt{R \delta^3} - 4\pi R \gamma_l \left(1 + \frac{\delta + 2h'}{4r} \right) \end{aligned} \quad (2.58)$$

The attractive forces are counted negative and the repulsive forces are counted positive. In order to find the adhesion force, i.e. the minimum in the total force-versus-indentation curve, the respective derivative is set to zero

$$\frac{dF_{Tot}}{d\delta} = 2E^* \sqrt{R \delta_{min}} - \pi R \frac{\gamma_l}{r} = 0 \quad (2.59)$$

2.9 Capillary force for the deformable surfaces in presence of adsorbed layers – the new analytical model

Therefore,

$$\delta_{min} = R \left(\frac{\pi \gamma_l}{2r E^*} \right)^2 \quad (2.60)$$

By substituting eqn. 2.60 into eqn. 2.58, one gets an expression for the absolute value of adhesion force

$$| F_{Adh} | = 4\pi \gamma_l R + \left(\frac{\pi \gamma_l}{2r} \right)^3 \frac{2R^2}{3E^{*2}} + 2\pi R h' \frac{\gamma_l}{r} \quad (2.61)$$

The first term of eqn. 2.61 is the capillary adhesion force between a hard sphere in contact with a hard surface. It is proportional to the sphere radius, R , and does not depend on the vapor pressure. The second term describes the additional contribution due to the elastic deformation of the soft elastic support that leads to an increased wetted area. It scales with R^2 and is inversely proportional to E^{*2} . This implies that it contributes much more significant for soft materials and vanishes for non-deformable materials. These two terms were already obtained by Butt et al. (21). The last term which takes into account the increase of effective meniscus size in presence of an adsorbed layer of liquid on solid surfaces is the additional term added to their analytical model because of the existence of the adsorbed layers. It is equal to the Laplace pressure, $\frac{\gamma_l}{r}$, multiplied by the additional area covered by the meniscus due to the adsorbed layers. It is proportional to R and vanishes for $h' \rightarrow 0$. Its relative contribution to the total capillary force depends on the ratio of $(\frac{h'}{r})$. If the adsorbed layer thickness is larger than the meniscus radius, this term will contribute significantly. The last two terms in eqn. 2.61 reflect the dependency of the capillary force on P/P_{sat} through the dependency of r and h' on P/P_{sat} .

2.9.2 Rigid sphere in contact with an elastic hydrophobic support including a physisorbed liquid layer only on the sphere

The same approach and assumptions as in the previous section are applied. The only difference is that a physisorbed layer of liquid exists only on the sphere (Fig. 2.13. b). In this case, eqn. 2.61 changes to

$$| F_{Adh} | = 4\pi \gamma_l R + \left(\frac{\pi \gamma_l}{2r} \right)^3 \frac{2R^2}{3E^{*2}} + \pi R h' \frac{\gamma_l}{r} \quad (2.62)$$

2.9 Capillary force for the deformable surfaces in presence of adsorbed layers – the new analytical model

As expected, the only difference lies in the missing factor of two in the last term. The existence of an adsorbate layer either on sphere or elastic support causes a faster increase of the filling angle and this effect also determines the dependency of adhesion on P/P_{sat} . For a quantitative description of the thickness of the physisorbed layer for the special case of ethanol, the adsorption isotherm introduced by Kim et al. (eqn. 2.36) is used.

At this point, it is instructive to compare the values of F_P and F_T to manifest that F_P is indeed the dominating term in the presented analytical models so far. Consider a simple case with no indentation and no adsorbate layer: $\delta = h' = 0$. In this case, the eqn. 2.57 changes to

$$\cos \beta = \frac{R}{r + R} \quad (2.63)$$

For a colloidal probe with radius of $2 \mu m$ and a meniscus curvature with the radius of $r = 2 \text{ nm}$, one gets $\beta = 2.56^\circ$ from eqn. 2.63. Substituting $\beta = 2.56^\circ$ and $\gamma_l = 0.022$ for the surface tension of ethanol into eqn. 2.50 gives

$$\begin{aligned} F_T &= 2\pi\gamma_l R \sin^2 \beta = 0.55 \times 10^{-9} N \\ F_P &= \pi \frac{\gamma_l}{r} R^2 \sin^2 \beta = 0.28 \times 10^{-6} N \end{aligned} \quad (2.64)$$

Eqn. 2.64 clearly shows that F_P is three orders of magnitude larger than F_T . Therefore, one can simply consider F_P as the dominating force compared with F_T .

2.9.3 Relative contributions of meniscus force, adsorbed layer thickness, and support deformation

What is the relative magnitude of the three different contributions to the total capillary force in eqs. 2.61 and 2.62? Only if the second and third term contribute significantly, a deviation from the simple case of rigid bodies without adsorption layer is expected. The third term that describes the effect of the adsorbed layer can be expected to be of the same order of the first one if h' is similar to r . For a hard rigid sphere/a hard rigid support, which is in thermodynamic equilibrium with ethanol, F_{Adh} is

$$|F_{Adh}| = 4\pi\gamma_l R + 2\pi R\gamma_l \frac{h'}{r} \quad (2.65)$$

If the support is deformable, and one includes the deformation of elastic support, eqn. 2.65 changes to eqn. 2.61 with the $(\frac{\pi\gamma_l}{2r})^3 \frac{2R^2}{3E^{*2}}$ term being pre-dominant for softer materials. The value of E^* for which support softness leads to a significant effect can be estimated by equating this term with the capillary force caused by the liquid meniscus as well as the adsorbate layer

$$\left(\frac{\pi\gamma_l}{2r}\right)^3 \frac{2R^2}{3E^{*2}} = 4\pi\gamma_l R + 2\pi R h' \frac{\gamma_l}{r} \quad (2.66)$$

Rearranging eqn. 2.66 yields

$$E^* = \frac{\pi\gamma_l}{2r} \sqrt{\frac{R}{6(2r + h')}} \quad (2.67)$$

In thermodynamic equilibrium, eqn. 2.67 can be used to find the E^* values for which either eqn. 2.61 or eqn. 2.62 holds. At $P/P_{sat} = 0.7$, substituting the values of ethanol surface tension, 0.022 N/m, ethanol meniscus radius, 1.45 nm, and adsorbate layer thickness, 1.04 nm, together with $R = 2 \mu\text{m}$, yields $E^* \approx 221 \text{ MPa}$. This implies that only for supports with an elastic modulus much larger than 221 MPa, one can neglect the effects of surface deformation.

2.10 Summary

In this chapter all the basic terms and theories needed to describe van der Waals forces, solid surface energy, Hertz contact mechanics model and capillary forces were introduced. Further, within a new analytical approach, the effect of ethanol physisorbed layer with the isotherm introduced by Kim et al. (4) was considered and combined with the earlier work considering capillary forces for a sphere/plane geometry, incorporating surface deformations due to Hertzian contact mechanics (21). The analytical approach reveals, three different constituent forces which sum up to the total adhesion force (eqn. 2.61): *first*, capillary adhesion force between a hard sphere in contact with a hard surface, *second*, a contribution due to the deformation of the elastic support leading to an increased wetted area and *third*, an additional capillary force contribution in presence of adsorbed ethanol layers.

3

Materials and methods

In this chapter materials, methods, and the techniques employed in the current PhD research are introduced. The main aim of the experimental part was to use colloidal probe technique to compare the capillary forces measured on hard surfaces to the ones measured on soft surfaces. The capillary forces originate from the capillary condensation of ethanol in well-defined relative partial vapor pressure (P/P_{sat}) of ethanol. Ethanol has low contact angles on soft polydimethylsiloxane (PDMS) and polyisoprene (PI) surfaces as well as on hard naturally oxidized silicon (Si) wafers without the need of further surface modifications.

Later in this chapter, it would also be explained how the analytical model introduced in chapter two is implemented step by step in the Comsol multiphysics software for the subsequent finite element method (FEM) simulations.

3.1 Sample preparation

The atomic force microscope (AFM) measurements on soft samples were carried out on two different classes of rubbers, cross-linked polydimethylsiloxane (PDMS) and the non-cross-linked cis-1,4 polyisoprene (PI) polymers. The cleaned surfaces of the naturally oxidized Si wafers were selected as hard substrates. Following, it is described how the smooth and homogeneous samples were prepared from PDMS and PI polymers. The cleaning process of Si wafers is also explained

3.1.1 Silicon wafers

Naturally oxidized silicon wafers with (100) crystallographic direction were cleaned by immersion in piranha solution of 50:50 sulphuric acid (H_2SO_4) and H_2O_2 (30%) overnight (*Warning: piranha solution is hazardous and highly reactive. It may explode on contact with organic solvents. Extreme care and precaution must be taken at all times.* Afterwards, the wafers were rinsed several times with milli-Q water (resistance: 18.2 M Ω cm).

3.1.2 PDMS samples

Polymers containing inorganic and organic components are named hybrid polymers. One of the best known examples is PDMS, which is composed of cross-linked chains of the form $[\text{O-Si}(\text{CH}_3)_2]_n$, with siloxane monomers based on silicon and oxygen.

The PDMS samples were prepared from different weight mixtures of a siloxane base and a cross linker agent (Sylgard Elastomer 184, Dow Corning Corporation, Midland, MI) that are stirred for 20 minutes at room temperature. According to the information given by the company (<http://drajput.com/research/sylgard184-pdms.php>), the base and the curing agent are composed of different compounds as presented in table 3.1.

By means of an epoxy dispenser (Coltène/Whaledent AG, Switzerland), lines of polyvinylsiloxane with the height of about 2 mm were deposited on the glass slides to form the walls of a rectangular mold with lateral dimensions of $2 \times 3 \text{ cm}^2$ (Fig. 3.1). In order to prepare PDMS samples, glass slides were cleaned with ethanol and acetone followed by argon (Ar) plasma cleaning for one minute (Expanded plasma cleaner PDC - 001/002 (115/230 V), Harrick scientific product, USA). Different mixing ratios of (base:curing agent) PDMS were then cast into such a mold, degassed for 1 hour in vacuum and then cured for another 45 minutes at 100 °C in vacuum. After that, samples were kept

Table 3.1: Sylgard 184 base and curing agent components.

Base	Curing agent
1. Dimethyl siloxane, dimethylvinyl terminated	1. Dimethyl, methylhydrogen siloxane
2. Dimethylvinylated and trimethylated silica	2. Dimethyl siloxane, dimethylvinyl terminated
3. Tetra (trimethoxysiloxy) silane	3. Dimethylvinylated and trimethylated silica
4. Ethyl benzene	4. Tetramethyl tetravinyl cyclotetra siloxane
	5. Ethyl benzene

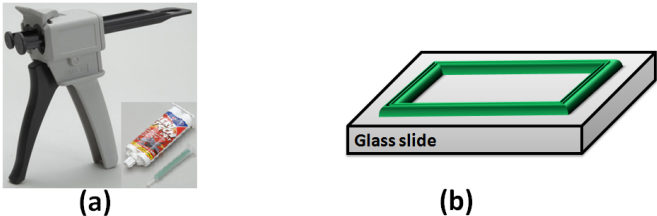


Figure 3.1: (a) Two barrel epoxy dispersion gun applied to create, (b) a rectangular green polyvinylsiloxane mold with the lateral dimensions of $2 \times 3 \text{ cm}^2$ on the clean glass slides.

immersed in an ethanol bath overnight to wash away all the non-cross-linked species from the top surface of the PDMS samples. Finally, the samples were dried for 3 hours in vacuum at room temperature before the experiment. During all processes the PDMS samples remained on the glass substrates. The final thickness of PDMS sample is about 2 mm.

3.1.3 O₂ plasma treatment of PDMS samples

The O₂ plasma treatment was performed some 10:1 PDMS, 15:1 PDMS and 20:1 PDMS samples in 0.1 mbar vacuum, at 80% power setting of the maximum O₂ plasma power of 100 W and for 5 s. During the O₂ plasma treatment of the PDMS samples, a silica layer forms on top of the sample surfaces. The silica layer increases the sample surface

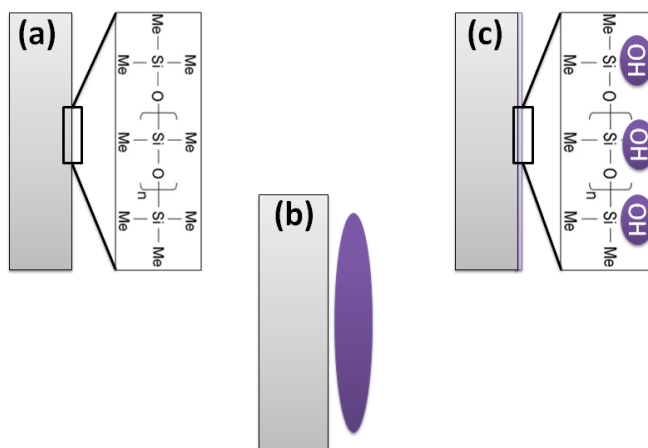


Figure 3.2: (a) The surface of a freshly prepared 10:1 PDMS sample; (b) the plasma is ignited and the surface modification starts: oxygen breaks some of the Si-CH₃ bonds; (c) some Si-CH₃ bonds at the surface are substituted by Si-OH bonds. The extent of substitution depends on the plasma treatment conditions.

energy and thus its wettability by water.

3.1.4 Polyisoprene samples

Polyisoprene is a synthetic rubber with the monomer of $\text{CH}_2=\text{C}(\text{CH}_3)-\text{CH}=\text{CH}_2$. PI polymer has four isomers and each of them has a unique set of properties (Fig. 3.3). Cis-1,4 and trans-1,4 PI polymers are the most important isomers. The cis-isomer is an elastomer polymer and the trans-isomer is a glassy solid polymer. For this study, cis-1,4 PI polymers with different molecular weights of 800 kDa, 1000 kDa and 2500 kDa were synthesized by the anionic reaction polymerization with butyl lithium. The polymerization was terminated by adding methanol. The synthesized PI polymers with different molecular weights of 800 kDa, 1000 kDa and 2500 kDa were all studied by proton nuclear magnetic resonance (NMR) spectroscopy (30).

The PI polymer samples were prepared on glass slide substrates by the solvent casting method. The glass slides were cut to $3 \times 3 \text{ cm}^2$ squares using a diamond knife. All glass slides were cleaned with ethanol and acetone followed by Ar plasma cleaning for one minute. These glass substrates were then placed at the bottom of a teflon mold to act as a support for the PI polymer thick films.

From each synthesized molecular weights of PI polymer, 0.2 mg was dissolved in 7 ml tetrahydrofuran (THF). The mixture were kept in small closed bottles with openings sealed with parafilm. It takes 4 and 12 hours for 800 kDa and 2500 kDa cis-1,4 PI polymers, respectively, to fully dissolve in THF, while being stirred at the speed of 250–300 rpm (round per minute) at room temperature. The cis-1,4 PI polymers dissolved in

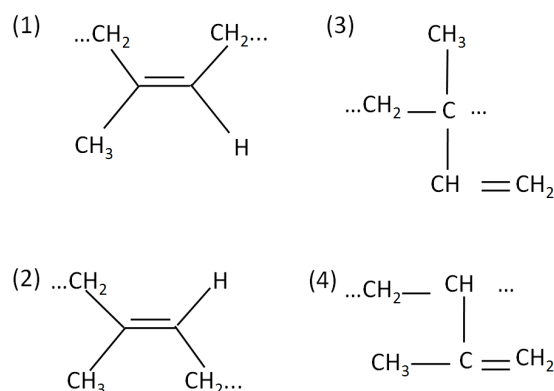


Figure 3.3: Different PI isomers known as (1) cis-1,4, (2) trans-1,4, (3) 1,2 and (4) 3,4 PI polymers.

the THF were then poured into similar molds with the glass substrates at the bottom. The molds containing cis-1,4 PI polymers-solvent solutions were placed for two days in a desiccator at room temperature, then kept for one day at 50 °C and another day at 30 °C in vacuum to remove traces of the solvent. The thickness of the PI samples obtained with this method is about 200 μm . During all processes the thick films of cis-1,4 PI polymers remained on the glass substrates.

cis-1,4 PI polymer is sensitive to light and undergo photo oxidation. Therefore, in all sample preparation processes, the bottles, molds, desiccator and oven window were wrapped by aluminium foil.

3.1.5 Pulse Nuclear magnetic resonance (NMR) spectroscopy

The synthetic cis-1,4 PI polymers with different molecular weights of kDa were dissolved in the deuterium labelled chloroform (CDCl_3). The solution of each sample was then transferred to the 5 mm uniform glass tubes. The samples were placed in the center of a superconducting NMR magnet mounted on the probe head (Fig. 3.4). The glass tube spins in the external magnetic field and thereby averages out both the variations of the created magnetic field between the two poles of magnet and the glass tube imperfections.

The probe head contains the transmitter and receiver coils. The transmitter is a radiofrequency (RF) generator that operates at the fixed frequency of $\nu_1 = 300 \text{ MHz}$. However, if the RF generator is switched for a short time, τ_p , one obtains a pulse which contains not just the frequency $\nu_1 = 300 \text{ MHz}$ but a continuous bands of frequencies symmetrical about the center frequency $\nu_1 = 300 \text{ MHz}$. In an NMR experiment the

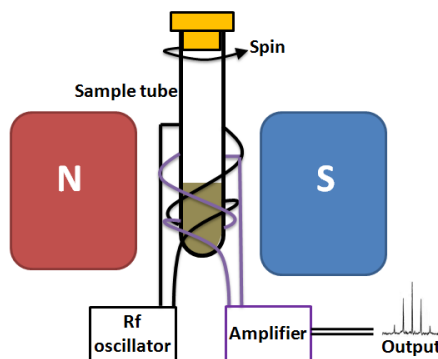


Figure 3.4: (Schematic diagram of a NMR spectrometer showing various components.

3.1 Sample preparation

pulse duration, τ_p , is of order of a few μs . The radiofrequency (RF) pulse radiation is then broadcast to the sample from an antenna coil.

The emission of adsorbed RF radiation by 1H is collected by the receiver coil. In a NMR spectrum, a nucleus shielded by more electrons appears at a larger frequency. If the zero of x axis represents the internal standard signal from tetramethylsilane (TMS) material, the corresponding chemical shift for each signal is calculated with (Fig. 3.5)

$$\delta = \left(\frac{\nu_{sample} - \nu_{ref}}{\nu_{ref}} \times 10^6 \right) ppm \quad (3.1)$$

ν_{sample} and ν_{ref} are the frequencies of RF signal detected from sample and the reference, respectively. The chemical shift has the unit of parts per million or ppm.

A NMR spectrum has two traces, one is the spectrum of adsorption signals at different δ values and the other is the integration trace. The integral trace calculates the area under each individual peak in the spectrum which is then proportional to the number of protons contributing to that signal.

The NMR spectra of the synthesized cis-1,4 PI polymers confirmed that they are mainly consisted of cis-1,4 PI polymer (Fig. 3.5). There is also a small amount of 3,4 PI polymer that does not change intensively when comparing 800 kDa cis-1,4 PI and 2500 kDa cis-1,4 PI polymers.

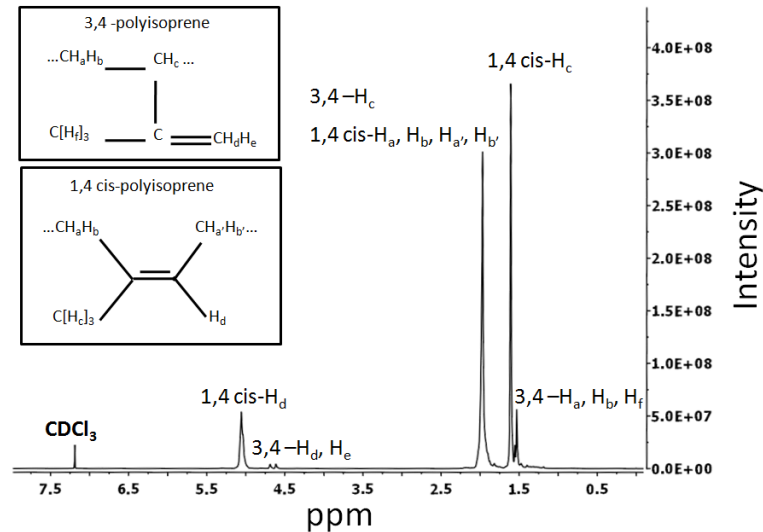


Figure 3.5: One-dimensional 300 MHz 1H NMR spectrum measured for 800 kDa cis-1,4 PI polymer in $CDCl_3$ plotted as the signal-versus-chemical shift at 298.34 K.

3.2 Contact angle measurement

The static advancing contact angles (ACA) of ethanol and water were measured on both soft PI samples with different molecular weights and different (base:curing agent) PDMS samples and also on the Si wafer by the sessile drop method (OCA 30, Data Physics, Germany). The obtained values are reported in section 4.4. It should be noted that during the contact angle measurements on different (base:curing agent) PDMS samples, a problem was encountered as the contact line could not be fully inhibited on different (base:curing agent) PDMS surface. Therefore, the advancing contact angles were measured by depositing a 2 mL droplet of ethanol on the PDMS surface.

3.3 Atomic force microscopy

Atomic force microscope (AFM) was invented by Gerd Binnig et al. (15) in 1986 is widely used to study different surface properties. The important characteristics of this scanning probe technique are its atomic resolution, sensitivity and manipulation capabilities.

An atomic force microscope uses a probe that interacts with the sample surface forces (Fig. 3.6.a). The probe is usually a sharp small tip with the radius of 5–10 nm that sits at the free end of a cantilever. The force on the cantilever results in corresponding deflection. The cantilever deflection is detected by reflecting a laser beam from the backside of the cantilever onto a photo detector. The raster movement of the cantilever

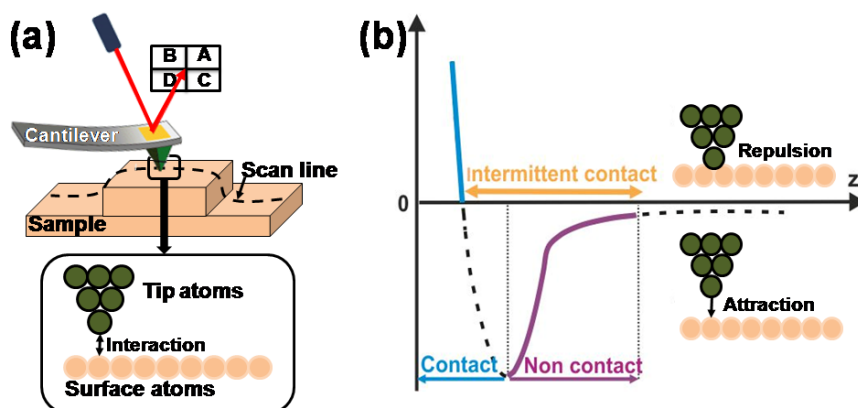


Figure 3.6: (a) Working principle of an AFM. (b) Different interaction potentials between the probe atoms and the surface atoms causing different operation modes in an AFM.

as well as the vertical deflection are controlled by x - y and z piezoelectric scanners. The cantilevers are usually made from silicon (Si) or silicon nitride (Si_3N_4). The use of silicon (nitride) is mainly because they can be processed with standard photolithography methods.

Topography images are recorded both in the *static* and the *dynamic* modes (65). In the *static* or the *contact* mode, the cantilever is in direct physical contact with the sample. In dynamic mode also called the tapping mode, the damping of an oscillating cantilever is used to record a topography image (Fig. 3.6.b). Following is a brief introduction of these different imaging modes. The imaging can be performed in different environments like air, liquid or vacuum.

3.3.1 Contact mode of AFM

In contact mode, the tip is raster-scanned over the sample surface line by line while it is in direct contact with the surface. A user defined deflection set-point value for the cantilever deflection and thus the force acting between the tip and the sample is applied by pushing the cantilever against the sample surface with a piezoelectric positioning element. During the measurement, the cantilever deflection is sensed and compared in a direct current (DC) feedback amplifier to the user defined set-point value of deflection. If the measured deflection differs from the set-point value, the feedback amplifier applies a voltage to the piezo to either raise or lower the sample relative to the cantilever to restore the user defined value of the set-point deflection. The voltage that the feedback amplifier has to apply to the z piezoscanner is a measure of sample height at the corresponding point. By recording the piezo movement for each point of the image, the sample topography can be reconstructed.

This normal forces create a substantial frictional force as the probe scans over the sample. In practice, these frictional forces are far more destructive than the normal force and can damage the sample, dull the cantilever probe and distort the resulting data. For polymer samples, the deflection set-point value is usually chosen less than 10 nN to reduce the effect of undesired tracking force of the tip on the sample surface.

Under ambient conditions, the contact mode AFM measurements should be performed with care because

1. The hydrophilic surfaces are covered by a pre-adsorbed water layer. When the tip touches this water layer, a meniscus forms and the cantilever is pulled by capillary forces toward the sample surface. The magnitude of the capillary forces depend on the details of the tip geometry. The capillary forces can be neutralized by performing the measurement in water.
2. Semiconductor and insulator samples can trap electrostatic charges. This charge can contribute to the additional attractive forces between the probe and sample. Such electrostatic forces can be partially dissipated and screened in liquid.

For the contact mode AFM imaging, the cantilevers should on one hand be soft enough to allow imaging at low forces, but still have a high enough resonance frequency to have low sensitivity to acoustic noise. Typical values for spring constants and resonance frequencies of the cantilevers used in this mode are 0.1-1 N/m and 10–100 kHz, respectively.

3.3.2 Tapping or intermittent contact mode

In the tapping mode, the cantilever is oscillated at or close to its resonance frequency, ω_0 , with the free amplitude of A_0 . The oscillations are excited by a piezoelement. The motion of the cantilever can be modelled as a damped harmonic oscillator as

$$m\ddot{z} + kz + \gamma\dot{z} = F_{ext} = k\Delta = ku_0\cos(\omega t) \quad (3.2)$$

where z is the position, γ is cantilever damping factor, and $\Delta = u_0\cos(\omega t)$ is the cantilever deflection. Multiplying eqn. 3.2 with $1/m$ and using the definitions

$$\omega_0 = \sqrt{k/m} \quad (3.3)$$

and defining the quality factor Q by

$$Q = \frac{\omega_0 m}{\gamma} \quad (3.4)$$

one gets

$$\ddot{z} + \omega_0^2 z + \frac{\omega_0}{Q} \dot{z} = \omega_0^2 u_0 \cos \omega t \quad (3.5)$$

The solution can be found in the form of

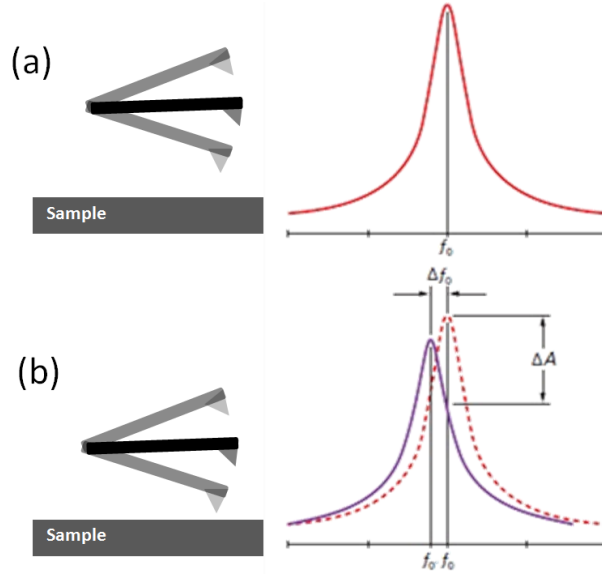


Figure 3.7: Resonance curve of a tapping mode cantilever (a) above and (b) close to the surface. Note that the resonance shifts to lower frequencies and exhibits a drop in amplitude. f_0 is the resonance frequency and ΔA is the change in the amplitude.

$$z(t) = z_0 + A(\omega)\cos(\omega t + \varphi) \quad (3.6)$$

with the amplitude

$$A(\omega) = \frac{u_0\omega_0^2}{\sqrt{(\omega_0^2 - \omega^2)^2 + \frac{\omega_0^2\omega^2}{Q^2}}} \quad (3.7)$$

and the phase shift

$$\varphi(\omega) = \arctan \frac{\omega_0\omega}{Q(\omega_0^2 - \omega^2)} \quad (3.8)$$

if $\omega = \omega_0$, $A(\omega_0) = Qu_0$ and $(\varphi(\omega_0)) = \pi/2$. When the cantilever is not in contact with the surface, the amplitude of its oscillation is equal to its free resonance amplitude A_0 . The oscillating tip then approaches the surface until it begins to lightly touch or tap the surface, which leads to the change of resonance frequency and therefore, the reduction of the oscillation amplitude.

During the tapping mode topography measurement, the instant amplitude minus the set-point amplitude results in an error signal, ΔA . For $\pm\Delta A$, the feedback loop system applies a voltage to the piezopositioning element to either increase/decrease the sample distance relative to the cantilever to increase/decrease the damping. The vertical adjustments of a z piezopositioning element are recorded as the height.

In the tapping mode phase imaging, the phase shift of the cantilever oscillation, relative to the input drive signal of piezopositioning element is recorded while the feedback loop maintains the amplitude at a fix value. For a cantilever oscillating freely in air the phase offset between these two signals is zero. As the probe tip engages the sample surface, the phase angle between these two signal changes. The phase shift is proportional to energy dissipation as a result of tip– sample interaction. Therefore, different components of a sample with different adhesive and mechanical properties show a phase contrast.

In this thesis, the surface properties of different polymer samples were investigated by the tapping mode AFM imaging (Nanowizard, JPK, Germany) to calculate surface roughness of the soft samples. The applied silicon cantilevers (OMCLAC 160 TS–W2, Olympus, Japan; 160 μm long, 50 μm wide, 4.6 μm thick) had the resonance frequencies of ~ 300 kHz and the spring constants of $k = 42$ N/m. The height of the tip was 7–15 μm and the tip radius of curvature was less than 10 nm.

3.3.3 Force spectroscopy and measuring the adhesion force

The AFM can not only be used for imaging but also to measure surface forces in the so-called force spectroscopy mode. The force–distance curves obtained in a force spec-

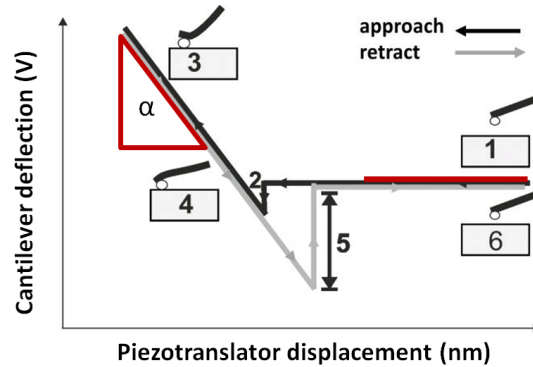


Figure 3.8: Schematic of the different steps in a force–piezo displacement curve: (1) the sample is not in contact with the colloidal probe; (2) the onset of colloidal probe jump–into–contact with the surface; (3) the sample is moved toward the colloidal probe to reach a certain force and the (4, 5) withdraw of sample starts and the colloidal probe undergoes jump–off–contact and (6) again there is no contact between the sample and the colloidal probe. The red lines show the gradient chosen for the sensitivity (α) measurement and the baseline offset for the deflection measurement, respectively. The red lines show the gradient chosen for the sensitivity (α) (20).

3.3 Atomic force microscopy

troscopy measurement are the representation of the surface forces versus the distance between sample surface and the AFM probe.

To measure a force–distance curve, one of the components, either the sample or the probe, is fixed and the other is kept free to move towards and away from the fixed component by a piezopositioning element. The deflection of the cantilever is then monitored by the reflection of a laser beam from the back of the cantilever on a photodiode. Each force–displacement curve can be interpreted with six different steps that are presented in Fig. 3.8. A cantilever deflection–piezo displacement curve (Fig. 3.8) can be transformed to a force–piezo displacement curve with the known deflection sensitivity, α and the cantilever spring constant, k as

$$F = \alpha \left[\frac{nm}{V} \right] \times v[V] \times k \left[\frac{N}{m} \right] \quad (3.9)$$

where v is the deflection of the cantilever. The deflection sensitivity, α , for each cantilever was determined from a linear fit of the constant compliance part (denoted with 3 in Fig. 3.8) of a deflection–piezo displacement curve measured on a Si wafer substrat. This slope is the conversion factor between the detector signal in volts and the cantilever deflection in nanometer.

In order to obtain a force–versus–distance curve, the piezo displacement Z_{piezo} have to be converted to the separation distance, D (Fig. 3.9). To do so, first a line is fitted on the flat part of the cantilever deflection–versus–piezo displacement curve. This part is related to where the cantilever is far from the surface (step 1, Fig. 3.8). This fit gives an offset value, δ_c which is either due to initial setting of the equipment or the thermal drift. It should be subtracted from all deflection data (19). The tip–sample separation

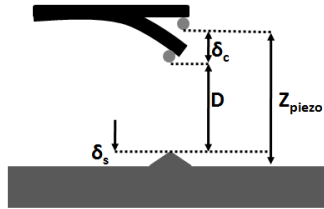


Figure 3.9: D is the actual tip–sample distance. Z_{piezo} is the piezo position. D and Z are not equal because of the cantilever deflection, δ_c , and the sample deformation, δ_s . δ_s as drawn here will usually be negligible while the probe is not in contact (22).

distance is then (22)

$$D = Z_{piezo} - (\delta_c + \delta_s) \quad (3.10)$$

From eqn. 3.10, the cantilever deflection is

$$\delta_c = Z_{piezo} - \delta_s + D \quad (3.11)$$

Fig. 3.9 gives an illustration of the Z_{piezo} , D , δ_s and δ_c . After measuring the cantilever deflection, the spring constant of the cantilever must be calibrated to get the actual force values.

In the case of soft polymer samples, like PDMS and cis-1,4 PI polymers, some reference force vs. piezo displacement curves were first recorded on clean Si wafers to obtain the correct values of deflection sensitivity and account for the elastic deformation of soft samples, δ_s .

In this thesis, the force-versus-piezo displacement curves were recorded to measure the adhesion forces between 2 μm silica micro-spheres as colloidal probes and different soft and hard surfaces. The measurements were performed using a commercially available atomic force microscope with a liquid cell (Nanowizard, JPK, Germany) in ambient conditions and either in a well-controlled vapor environment of a ethanol or water. The adhesion force between a sample and the probe tip is the minimum force in the retract part of force-piezo displacement curve (minimum of grey curve in Fig. 3.8) prior to the colloid probe snap-off from the surface. In fact the adhesion force is the pull-off force needed to fully remove the probe from the surface in the jump-off-contact step.

3.3.4 Root-mean-square roughness

The root-mean-square (RMS) roughness values for 6 different $1 \times 1 \mu\text{m}^2$ scan areas on 3 different samples was calculated using version 2.19 of Gwyddion AFM image analysis software (<http://gwyddion.net>)¹ The mathematical definition of RMS roughness is

$$R_{RMS} = \sqrt{\frac{\sum_{i=1}^n z_i^2}{n}} \quad (3.12)$$

Z_i is the height value with respect to the mean height value (Fig. 3.10). The RMS

¹The recorded topography images were levelled using the mean plane subtraction function provided by the software.

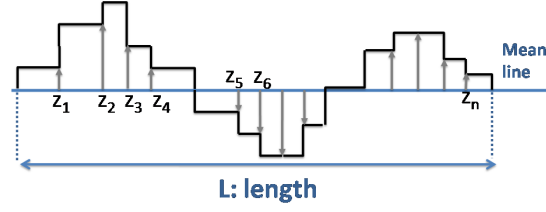


Figure 3.10: A schematic illustrating how z_i for calculation of RMS roughness value in eqn. 3.12 is defined.

roughness value depends on the length scale, L , over which it is calculated. The results are presented in chapter four.

3.4 Colloidal probe preparation

The colloidal probe technique was developed independently by Butt (17) and Ducker (28). In this technique a colloidal probe consisting of a colloidal particle of few micrometers in diameter that is attached to an AFM cantilever is used in combination with a standard AFM. The colloidal probe technique is widely used to measure surface forces and to investigate the mechanical properties of interfaces, bubbles, capsules, membranes, or cell walls for the sphere/plane or sphere/sphere geometries.

In this research, a micromanipulator (Narishige MMO - 203, Japan) is used to attach silica micro-spheres ($4.0 \pm 0.2 \mu\text{m}$ diameter, polysciences, Germany) to the tipless AFM cantilevers (μmasch , NSC12, tipless, no Al, EU, nominal spring constants of 7.5 N/m) by using the Epikote 1004 glue (Momentive Specialty Chemicals, Columbus, Ohio) to form the colloidal probes. Prior to the attachment, the silica micro-spheres were washed with water and ethanol in centrifuge. Centrifugation was done to separate particles after washing from its supernatant solution.

A droplet from the suspension of silica micro-spheres in ethanol is deposited on one corner of a clean glass slide. After the evaporation of ethanol, the $2 \mu\text{m}$ silica micro-spheres deposited on the glass slide are cleaned by Ar plasma cleaning for one minute. These cleaning treatments remove the adsorbed organic contaminations on the silica micro-spheres.

Steps 1–4 in figure 3.11 depict different steps of a colloidal probe production. The glass slide with the deposited silica particles is placed on a heating stage under an optical microscope. A small piece of Epicote 1004 glue is immediately set on the left hand side

3.5 Thermal noise method: measuring a cantilever spring constant

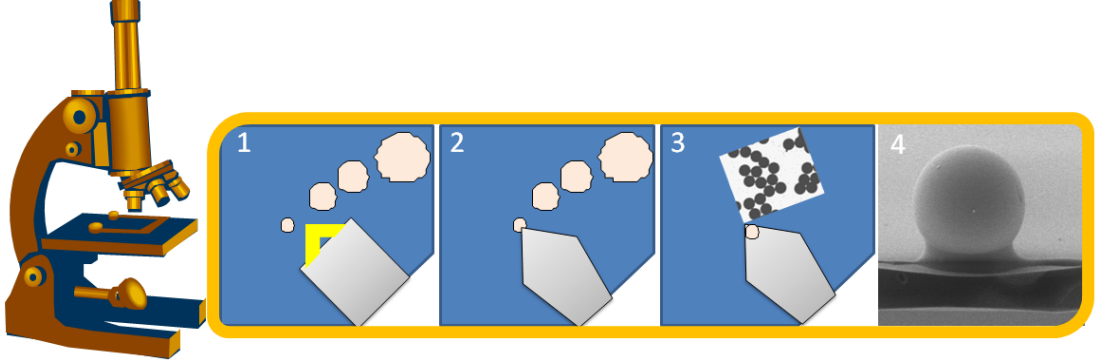


Figure 3.11: 1-4 shows different steps of a colloidal probe production procedure.

of the same glass slide. The glue melts at 90°C. The temperature of the heating stage is set to 100°C degree. Then, the first cantilever is used to touch the edge of the large glue droplet to pick up a small amount of glue. By touching the glass slide repeatedly with the cantilever, smaller and smaller droplets are deposited onto the glass slide (step 1). After that, the first cantilever is substituted with another one to pick up a small glue droplet (step 2). Afterwards, by using the micro-manipulator, the cantilever with a small droplet of glue on its tip is moved towards a silica particle (step 3). By pressing the cantilever on top of a silica particle, a colloidal probe consisting of the silica sphere attached to the free end of an AFM cantilever is prepared (step 4).

3.5 Thermal noise method: measuring a cantilever spring constant

The thermal noise method is a popular calibration method to measure the spring constant of a cantilever. This method is applicable to most types of the cantilevers. Modelling the cantilever as a simple harmonic oscillator, Bechhoefer and Hutter (46) applied the equipartition theorem and related the Brownian motion of its first oscillation mode to its thermal energy by

$$\frac{1}{2}k\langle Z_c^2 \rangle = \frac{1}{2}k_B T \quad (3.13)$$

from which

$$k = \frac{k_B T}{\langle Z_c^2 \rangle} \quad (3.14)$$

3.6 Ethanol vapor pressure control

where k is the cantilever spring constant, k_B is the Boltzmann constant and $\langle Z_c^2 \rangle$ is the mean square displacement of the cantilever. $\langle Z_c^2 \rangle$ is obtained by carrying out a power spectral density analysis of the cantilever oscillations and integrating the area under the peak of the first oscillating mode.

Later eqn. 3.14 was corrected by Butt and Jaschke (18) by considering the bending shapes of each mode. These authors also recognized that the optical detection system results in an additional error because it detects cantilever inclination rather than true displacements. Taking both of these correction factors into account, the final corrected equation for the first mode oscillation of a rectangular cantilever is (61)

$$k = 0.817 \frac{k_B T}{\langle Z_c^{*2} \rangle} \cos^2 \theta \quad (3.15)$$

where $\langle Z_c^{*2} \rangle$ is the displacement measured by the optical cantilever detection and θ is the cantilever tilt angle.

In this thesis, the spring constants of individual colloid probes were obtained by the thermal noise calibration method integrated in the AFM control software. The measured spring constants were in range of 6.2 N/m to 7.7 N/m which were in a good agreement with the range given by the manufacturer (5–12 N/m).

3.6 Ethanol vapor pressure control

To control the ethanol vapor pressure inside the closed volume of a liquid cell, the mixing ratio of two gas streams of dry nitrogen and nitrogen saturated with ethanol vapor were adjusted using two mass flow controllers (GFC mass flow controller, AALBORG, USA) (Fig. 3.12). The relative vapor pressure of ethanol (P/P_{sat}) was changed from 0 % to

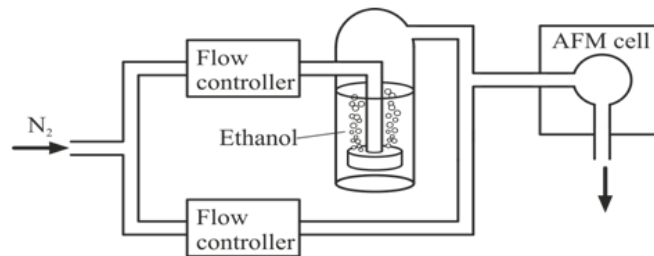


Figure 3.12: Schematic of the experimental set up to obtain different P/P_{sat} of a ethanol in an AFM liquid cell.

100 %. The water vapor pressure was controlled in the same way as the ethanol vapor pressure.

3.7 Mechanical characterization using stress–strain curves

3.7.1 True Stress and Strain

Consider a solid rectangular slab which is stretched by two forces, F_1 and F_2 (Fig. 3.13). The force acting on each face of a small volume element of the slab can be resolved into three components: one normal to the cube face and two parallel to the cube face (13). A normal force component divided by the area of a cube face over which it acts gives the normal stress (σ). The parallel force components divided by the cube face area over which they act give the shear stresses (τ).

Strain is the response of a system to an applied stress. The true strain measures the changes in the cross-sectional area by using the instantaneous values for the area. Usually, engineering stress and strain data are used because it is easier to generate the data and the tensile properties are adequate for engineering calculations.

3.7.2 Engineering stress and strain

Engineering stress and strain use a fixed, undeformed initial cross-sectional area in the calculations. The term stress is used to express the load applied to the cross-sectional

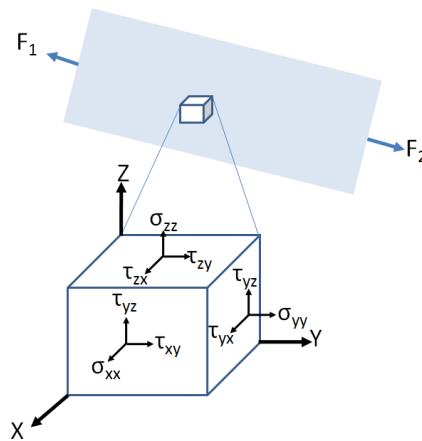


Figure 3.13: A schematic showing the normal stress (σ), and the shear stresses (τ), acting on a small area of a plane (13).

3.7 Mechanical characterization using stress–strain curves

area of a sample which tends to deform it. From the perspective of what is happening within a material, stress is the internal distribution of forces within a body that balance and react to the loads applied to it.

The stress for an axially loaded 'dog–bone' shaped sample (3.14) is simply equal to the applied load, P , divided by its initial cross-sectional area, A_{ini} (27)

$$\sigma_e = \frac{P}{A_{in}} \quad (3.16)$$

The engineering strain is defined as the amount of deformation in the direction of the applied load divided by the initial length of the material. This results in a unit–less number. Respectively, the engineering strain is defined as (27)

$$\epsilon_e = \frac{l_i - l_{in}}{l_{in}} = \frac{\Delta l}{l_{in}} \quad (3.17)$$

When σ_e is plotted against the ϵ_e , a stress–strain curve is obtained.

The elastic modulus of a material can be obtained by fitting the linear region of a stress–strain curve where the material obeys Hooke's law to a reasonable approximation as (27)

$$\sigma_e = E\epsilon_e \quad (3.18)$$

where the constant of proportionality, E , is the elastic modulus. If a sample is loaded within the linear elastic region, it deforms elastically and it will return to its original shape when the load is removed. However, if a material is loaded beyond its yield strength, then it undergoes plastic deformation and will not regain its original shape when the load is removed.

3.7.3 Measuring engineering stress–strain curves

Engineering stress–strain curves were measured to study different soft samples. For these experiments the following soft samples were prepared

1- PDMS sample preparation. Teflon molds of $3 \times 3 \times 3$ cm³ were filled with different weight mixing ratios of (base:curing agent) PDMS. The samples were cured with the same cring procedure described in section 3.1. The cross–linked polymer samples can be easily removed from the mold teflon and used for further experiments. The thickness of each PDMS sample was about 4 mm.

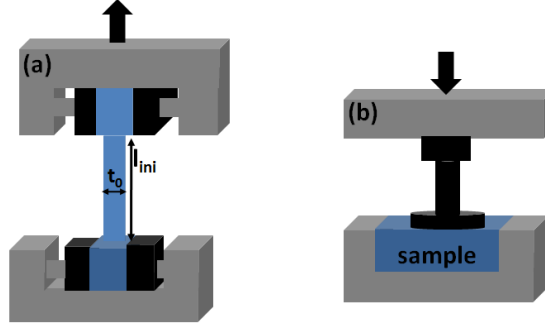


Figure 3.14: (a) Schematic of a tensile measurement. $t_0 = 2$ mm and $l_{ini} = 10$ mm are the initial sample thickness and length, respectively. (b) Schematic of compression test. The black arrows show the movements during the experiments.

2- Cis–1,4 PI sample preparation. Different molecular weights of cis–1,4 PI polymer were dissolved in THF and treated as explained in section 3.1. The ultimate thickness of the sample was about $200\text{ }\mu\text{m}$.

3.7.3.1 Tensile test

Tensile tests (27) were performed to measure the elastic modulus of different soft samples. In tensile test a 'dog–bone' shaped sample was mounted by its ends into holding grips of the testing device (Material–Pruefmachine Allround–line 5 kN rheometer, Zwick/Roel, Germany). The sample is then stretched by an increasing uni–axial load along the long axis of sample. Simultaneously, the elongation is measured by a transducer. The load and elongation data are converted to engineering stress and strain, respectively.

3.7.3.2 Compression test

Compression tests (27) were used to study the materials' behaviour under a compressive stress. By convention a compressive force is negative and it yields a negative strain, since the initial length l_{in} is always larger than the instantaneous length. Compressive strain–stress curves were only measured for the 10:1 PDMS sample to determine its compressive strength. In this experiment, the 10:1 PDMS samples were compressed using the flat discs with different radii of 1 mm, 2.5 mm and 5 mm, respectively. The deformation at various loads in range of 0–70 kN were recorded. The sample had a transition from rubbery state to plastic hardening behavior while being compressed

with the same force but with different disc radii of 5 mm and 1 mm, respectively. Such transition is caused by the change of strain in the contact area between different discs and a sample.

In fact, for a specific load, P , applied on two different discs with radii A_1 and A_2 which are compressing a material with elastic modulus of E , one can write

$$\frac{P/A_1}{P/A_2} = \frac{E\varepsilon_1}{E\varepsilon_2} \quad (3.19)$$

where ε_1 and ε_2 are the strains under the two discs with radii A_1 and A_2 , respectively. By cancelling out the equal quantities in the numerator and denominator and rearranging this equation, one gets

$$\frac{A_2}{A_1} = \frac{\varepsilon_1}{\varepsilon_2} \quad (3.20)$$

or

$$A_1\varepsilon_1 = A_2\varepsilon_2 \quad (3.21)$$

Equation 3.21 shows the decrease/increase of strain with disk radii. In this experiment, the use of samples with high aspect ratios (length/cross sectional radius) was avoided to prevent buckling, shearing and barrelling modes of deformation (27).

3.8 Scanning electron microscopy

Low-voltage high-resolution scanning electron microscope (SEM) (Leo 1530 Gemini, Zeiss, Germany) was used to record images from the colloidal probes after adhesion measurement between the 2 μm radius silica micro-spheres and soft samples in the controlled vapor pressure of ethanol.

In the SEM measurements in this thesis, the cantilevers were mounted on a pre-tilted 90° sample holder which is covered with a carbon conductive tape. The colloidal probe surface was probed with a focused electron beam with electron energies of 2–3 keV. The probing electrons are emitted from a field emission cathode. In order to obtain the SEM images, the secondary electrons are detected with an Everhart-Thornley detector (ETD). The beam resolution is ~ 4 nm at 1 keV.

3.9 Sum frequency generation (SFG) spectroscopy

Sum frequency generation (SFG) spectroscopy is a non-linear optical technique to study the properties of surfaces and interfaces (51). In a typical SFG set-up, two laser beams, an infrared and a visible light beam, mix at a surface and generate an output beam with a frequency equal to the sum of the two input frequencies (Fig. 3.16). In such infrared-visible SFG experiments, the surface is simultaneously subjected to two intense electric fields. The induced polarization is expressed using the electric-dipole approximation as

$$P = \varepsilon_0(\chi^{(1)}(E_1 + E_2) + \chi^{(2)}(E_1 + E_2)^2 + \dots) \quad (3.22)$$

Here, P is the polarization vector, E_i is the electric field vector, and $\chi^{(1)}$ and $\chi^{(2)}$ are the first- and second-order electric susceptibility tensors of the medium. Substituting $E_1 = E_1^0 \cos(\omega_1 t)$ and $E_2 = E_2^0 \cos(\omega_2 t)$ and considering only the second-order term of polarization, $P^{(2)}$, one gets

$$P^{(2)} = \varepsilon_0 \chi^{(2)} (E_1 \cos \omega_1 t + E_2 \cos \omega_2 t)^2 \quad (3.23)$$

With a trivial trigonometric rearrangement, it is easily seen that eqn. 3.23 has a sinusoidal component $\frac{1}{2} E_1 E_2 \cos(\omega_1 + \omega_2) t$ which shows that the light is emitted at the sum of the incident frequencies, $\omega_1 + \omega_2$.

From symmetry arguments it can be shown that the third-rank tensor, $\chi^{(2)}$, has a value of zero in centrosymmetric media if it can be assumed that only electric-dipole moments are responsible for $\chi^{(2)}$, and the contributions from higher-order multipoles and magnetic dipoles are negligible (a usually good approximation). This is why SFG is forbidden in the bulk of substances, but it is allowed at the interface between bulk phases where there will be no centrosymmetry. Therefore, SFG spectroscopy allows the detection of physical and chemical adsorption of molecules even with sub-nanometer thicknesses at the interfaces between the bulks of different substances.

The SFG spectroscopy measurements were performed to check if there was an ethanol physisorbed layer adsorbed to a 10:1 PDMS sample surface which was exposed to ethanol vapor at saturated conditions. In order to perform this experiment, a closed cell with a 2 mm thick CaF_2 window was designed, allowing the penetration of both

3.9 Sum frequency generation (SFG) spectroscopy

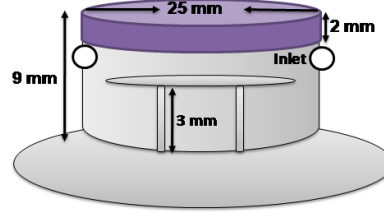


Figure 3.15: Schematic of the cell designed for SFG experiment.

infrared and visible light (Fig. 3.15). High vapor pressure of ethanol was introduced in the close cell around a free standing 10:1 PDMS sample. The infrared laser pulses (~ 7 mJ/pulse, bandwidth ~ 400 cm^{-1}) were generated by white light seeded optical parametric amplification (TOPAS, Light Conversion) in combination with a difference frequency generation stage. The TOPAS was pumped by part of the 800 nm output of a ~ 40 fs amplified Ti:Sa laser system working at 1 kHz (Spitfire Ace, Spectra-Physics). Another part of the output of the Ti:Sa laser was passed through an etalon to obtain narrow band visible pulses (~ 20 mJ/pulse, bandwidth ~ 10 cm^{-1}) determining the frequency resolution of the experiment. The infrared (IR) and the visible (VIS) beams were combined at the surface under a co-propagating geometry with incident angles of roughly 25–30 degrees with respect to the surface normal for the IR and VIS beams, respectively. Fig. 3.16 depicts different parts of the SFG set-up used in this work. Four different polarization combinations are used in this study: SSP (s-polarized SFG output, s-polarized visible input, p-polarized infrared input), PPP, PSS and SPS. The data are normalized to an SSP signal from a 40 nm thick gold film. The SFG signal is dispersed in a spectrometer and detected by a CCD camera. A computer is used for

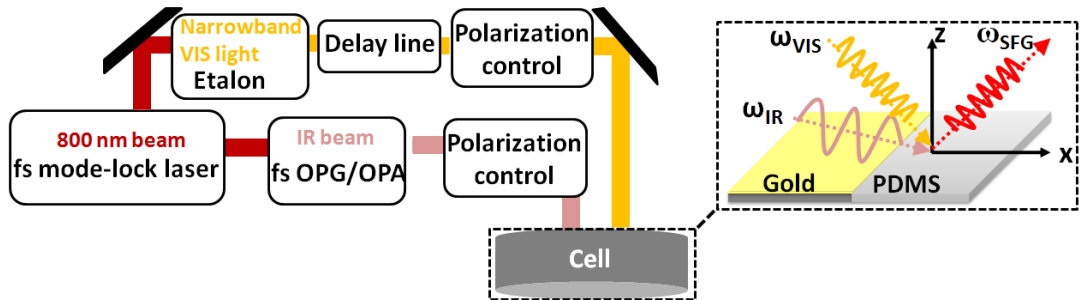


Figure 3.16: The schematic plot of SFG set-up. Both the 10:1 PDMS sample and the gold thin film deposited on a silicon wafer were inside the closed cell. The measurement on gold and 10:1 PDMS were performed in air and in a saturated ethanol environment, respectively.

data acquisition and analysis.

3.10 Finite element method (FEM) simulation

Finite element method (FEM) simulations were carried out by means of the Comsol multiphysics package, version 4.2.a ([http:// www.comsol.com](http://www.comsol.com)) using structural mechanics module with linear elastic material properties.

FEM simulations were performed to calculate the adhesion forces between a rigid sphere and different hard and soft supports in the presence of ethanol meniscus. The ethanol meniscus originates from the capillary condensation of ethanol in the contact area between the sphere and different hard and soft supports. Figure 3.17 compares the analytical model presented in section 2.9 which only considered a Hertzian contact deformation to the FEM simulations which additionally account for surface deformations within the meniscus due to the Laplace pressure (distance D in Fig. 3.17.b). This effect

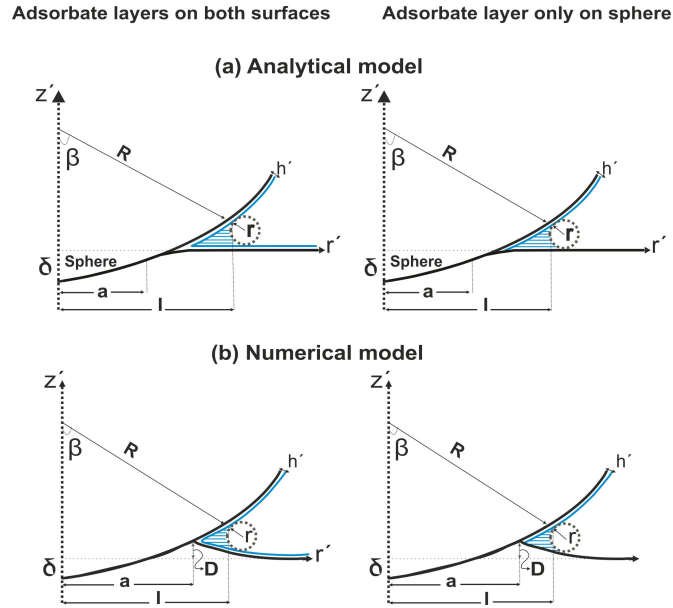


Figure 3.17: Schematics of an elastically deformed surface indented by a hard sphere in presence of an adsorbate layer either on both surfaces or only on the sphere. The models applied for (a) the analytical approach and corresponding calculations and (b) for the numerical study are compared. The numerical model additionally considers the effect of upward elastic deformation of the soft supports caused by the capillary pressure in the liquid meniscus by a distance D .

is not considered in the analytical model and has significant consequences for soft ma-

materials exposed to a relatively high Laplace pressure induced by a small meniscus radius (large curvature). In such a case, the additional surface deformation leads to the higher indentation of the sphere onto a soft elastic support and therefore, a larger contact area forms. In order to solve such problems without analytical solutions, one has to use the numerical methods like finite element method (FEM) simulations (13, 41).

3.10.1 Introduction to finite element method simulation

The idea of finite element method (FEM) analysis is introduced with solving an example which also has an analytical solution (41): First, this example is solved analytically and then numerically, using FEM analysis.

Consider a three-dimensional (3D) object as given in (Fig. 3.18.a). $F(x)$ is an external load pressing the object. With exploiting the rotational symmetry the 3D model can be mapped onto a two-dimensional (2D) model (Fig. 3.18.b). The aim is to find the total displacement of the object, u_{Tot} caused by the external load compared to the case of $F(x) = 0$. For the axial force of $F(x)$, the displacement is only in x direction, $u = u(x)$. In this example, the displacement is only along the x axis. Therefore, there is no Poisson's ratio effect. With K , the stiffness of the material and A , the cross sectional area on which the external force is applied, one gets

$$\varepsilon(x) = \frac{du(x)}{dx} = \frac{F(x)}{AK} \quad (3.24)$$

where ε is the strain, and $\frac{F(x)}{A}$ is the normal stress. If the two cylinders are made from the same material, the stiffness is equal to the elastic modulus, $K = E$. Using eqn.

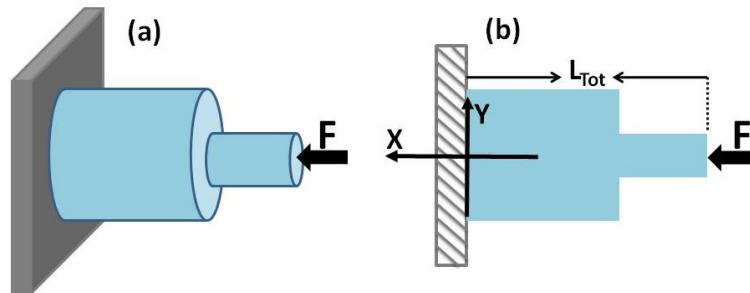


Figure 3.18: (a) 3D geometry and (b) the corresponding 2D model. F is external force, $u(x)$ is the displacement, and L_{Tot} is the total length of 2D model (41).

3.10 Finite element method (FEM) simulation

3.24, $u(x)$ can be calculated as

$$u(x) = \int_0^{L_{Tot}} \frac{F(x)}{AK} dx \quad (3.25)$$

Substituting $F(x) = 20 \text{ kN}$, $l_1 = 10 \text{ m}$, $l_2 = 5 \text{ m}$, $K = 300 \times 10^6 \frac{N}{m^2}$, $A_1 = \pi r_1^2$, and $A_2 = \pi r_2^2$ with $r_1 = 5 \text{ m}$ and $r_2 = 2.5 \text{ m}$, the analytical solution for this problem is

$$u(x) = \int_0^{l_1} \frac{F(x)}{K\pi r_1^2} dx + \int_{l_1}^{l_1+l_2} \frac{F(x)}{K\pi r_2^2} dx = 24.78 \times 10^{-6} \text{ m} \quad (3.26)$$

To introduce the idea of FEM, the above mentioned problem is also solved numerically with FEM i.e. the partial differential equation (PDE) in eqn. 3.24 is solved numerically. It starts with the introduction of a PDE as

$$f(u'(x), u(x)) = 0 \quad (3.27)$$

in the general case, higher derivatives can be involved as well. However, here the simplest case is considered. The prime indicates the derivative with respect to x . The PDE of our example model can be defined as

$$u'(x) - \frac{F}{AK} = 0 \quad (3.28)$$

Next, the so-called discretization process is needed to solve this equation .

3.10.1.1 Discretization

In order to solve eqn. 3.28, the overall model geometry is approximated by the simpler geometrical objects (Fig. 3.19) which are called elements. After defining the elements, the nodes are defined. With the definition of nodes, a physical quantity like displacement is only calculated at the nodes. In this example model, there are three nodes, 1-3. By first approximation, the displacement between these nodes can be interpolated linearly with a guess function introduced in the next section.

3.10.1.2 Linear guess function

A general linear guess function for the displacement of the i th element is defined by

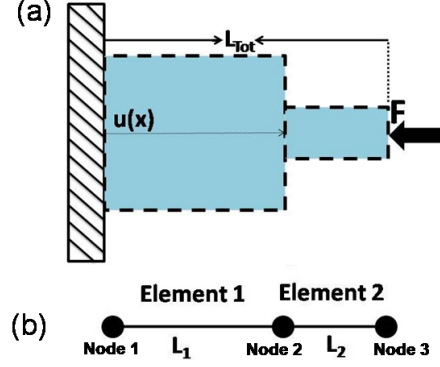


Figure 3.19: (a) Schematic of the discretization or the approximation of the overall geometry by some simpler geometrical objects. (b) the physical quantities are only solved at nodes.

$$\tilde{u}_i(x) = ax + b \quad i : \text{number of element} \quad (3.29)$$

For the first element in this mode example, the constants a , b are obtained from

$$\begin{aligned} \tilde{u}_1(0) &= u_1 = b \\ \tilde{u}_1(l_1) &= u_2 = a \cdot l_1 + b \quad \Rightarrow \quad a = \frac{u_2 - u_1}{l_1} \end{aligned} \quad (3.30)$$

where u_i is the displacement of i th node. By substituting eqn. 3.30 in eqn. 3.29 one gets

$$\tilde{u}_1(x) = u_1 \left(1 - \frac{x}{l_1}\right) + u_2 \left(\frac{x}{l_1}\right) \quad x \in [0, l_1] \quad (3.31)$$

with the definition of so-called form functions as

$$\begin{aligned} N_1(x) &= \left(1 - \frac{x}{l_1}\right) \\ N_2(x) &= \left(\frac{x}{l_1}\right) \end{aligned} \quad (3.32)$$

One can write

$$\tilde{u}_1(x) = \begin{pmatrix} N_1(x) \\ N_2(x) \end{pmatrix} \cdot \begin{pmatrix} u_1 \\ u_2 \end{pmatrix} \quad (3.33)$$

With the same approach, for the second element one can get

$$\tilde{u}_2(x) = u_3 \left(\frac{x - l_1}{l_2}\right) + u_2 \left(\frac{l_1 - x + l_2}{l_2}\right) \quad x \in [l_1, l_2] \quad (3.34)$$

3.10 Finite element method (FEM) simulation

By assembling the results from eqs. 3.31 and 3.34 for both elements, the overall guess function is

$$\tilde{u}(x) : \quad \begin{cases} \tilde{u}_1(x) = u_1(1 - \frac{x}{l_1}) + u_2(\frac{x}{l_1}) & x \in [0, l_1], \\ \tilde{u}_2(x) = u_3(\frac{x - l_1}{l_2}) + u_2(\frac{l_1 - x + l_2}{l_2}) & x \in [l_1, l_2] \end{cases} \quad (3.35)$$

or in matrix form

$$\tilde{u}(x) = \begin{pmatrix} \frac{l_1 - x}{l_1} & \frac{x}{l_1} & 0 \\ 0 & \frac{l_1 - x}{l_2} & \frac{x - l_1}{l_2} \end{pmatrix} \cdot \begin{pmatrix} u_1 \\ u_2 \\ u_3 \end{pmatrix} \quad (3.36)$$

Using finite element method one can find a $\tilde{u}(x)$ for which

$$f(\tilde{u}'(x), x) \approx 0 \quad x \in [0, L_{Tot}] \quad (3.37)$$

The difference from $r = 0$ is the error introduced in the calculation from the approximation of the guess function. To calculate the total error, the total residual error, R , is defined.

3.10.1.3 Minimizing the residual function

In FEM simulation, the total residual error for the displacements of the nodes 1–3 is defined as

$$\begin{aligned} R(u_1, u_2, u_3) &= \int_0^{L_{Tot}} (f(\tilde{u}'(x), x))^2 dx \\ &= \int_0^{l_1} (\frac{u_2 - u_1}{l_1} - \frac{F}{A_1 k})^2 dx + \int_{l_1}^{l_1 + l_2} (\frac{u_3 - u_2}{l_2} - \frac{F}{A_2 k})^2 dx \end{aligned} \quad (3.38)$$

The displacement for each individual node i.e. u_1, u_2 and u_3 is then calculated from

$$R_{u_i} = \frac{dR(u_1, u_2, u_3)}{du_i} = 0 \quad i = 1, 2, 3 \quad (3.39)$$

from which we get

$$\begin{pmatrix} K & -K & 0 \\ -K & 2K & -K \\ 0 & -K & K \end{pmatrix} \cdot \begin{pmatrix} u_1 \\ u_2 \\ u_3 \end{pmatrix} = \begin{pmatrix} -\frac{Fl_1}{A_1} \\ \frac{Fl_1}{A_1} - \frac{Fl_2}{A_2} \\ \frac{Fl_2}{A_2} \end{pmatrix} \quad (3.40)$$

3.10 Finite element method (FEM) simulation

To find the definite values for u_1 , u_2 and u_3 from the system of linear equations in 3.40, one must apply the boundary conditions. Here, it can be assumed that node 1 is fixed and substitutes $F = 20$ kN, $l_1 = 10$ m, $l_2 = 5$ m, $K = 300 \times 10^6 \frac{kN}{cm^2}$, $A_1 = \pi r_1^2$, $A_2 = \pi r_2^2$ with $r_1 = 5$ m and $r_2 = 2.5$ m

$$\begin{pmatrix} 1 & 0 & 0 \\ -1 & 2 & -1 \\ 0 & -1 & 1 \end{pmatrix} \cdot \begin{pmatrix} 0 \\ u_2 \\ u_3 \end{pmatrix} = \begin{pmatrix} 0 \\ -9.18 \times 10^{-6} \\ 16.98 \times 10^{-6} \end{pmatrix} \quad (3.41)$$

which gives

$$\begin{aligned} u_3 &= 24.78 \times 10^{-6} \text{ m} \\ u_2 &= 7.8 \times 10^{-6} \text{ m} \end{aligned} \quad (3.42)$$

the value of u_3 matches perfectly with the analytical result in eqn. 3.26.

3.10.2 Geometry and the coordinate system

The rigid isotropic indenter is pushed into the surface of the elastic isotropic homogeneous support. The indenting sphere was modelled as an isotropic, homogeneous rigid shell made from two 40° sectors of two spheres, with radii of $2 \mu\text{m}$ and $1.8 \mu\text{m}$, respectively. The model dimensions of the elastic support were $40 \mu\text{m}$ in depth and $8.5 \mu\text{m}$ in radial direction, respectively.

A cylindrical coordinate system with rotational symmetry was used. By exploiting the axial symmetry, the displacement field has only non-zero components in r and z directions of coordinate system

$$u(r, z) = u_r \hat{r} + u_z \hat{z} \quad (3.43)$$

3.10.3 Physics governing the finite element method (FEM) model

By using an inner iteration, the indentation of a rigid sphere onto an elastic support is successively increased. Without any other forces, the contact area between the shell and the elastic support would increase according to the Hertz contact mechanics model. Yet, in the present model an additional force is introduced by considering the Laplace

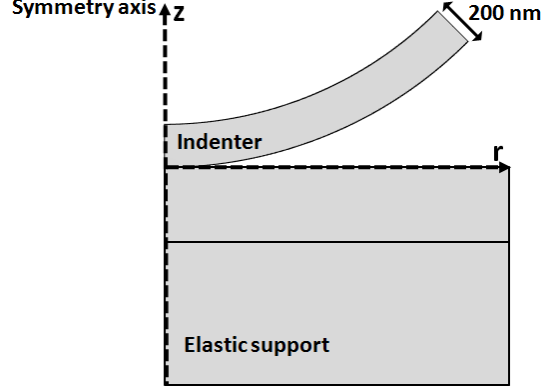


Figure 3.20: The spherical shell/elastic support geometry used for FEM simulations. The coordinate axes of r and z are introduced. The axial symmetry is along the latter. The spherical shell is positioned at $(r=0, z=0)$

pressure acting over the wetted area. In the present quasi-static context, the fluid dynamics within the condensed liquid can safely be neglected. Instead, the radius l of the wetted area is obtained by considering that the respective gap between the elastic support and the sphere has to be equal to twice the meniscus radius r in order to accommodate the meniscus, cf. Figure 3.17. Since for a given saturation pressure P/P_{sat} the meniscus radius r is given by the Kelvin equation, one can in this way identify the wetted area. Multiplying it with the known Laplace pressure, the corresponding forces on the substrate and sphere are obtained. The additional surface deformation arising from these forces pushes the position of the meniscus further out and this new position is then used in the next step. This inner iteration is continued until convergence occurs at the relative tolerance of 0.001 for the solution. The adsorbate thickness, h' , does not change the meniscus curvature. It only has a geometrical effect causing the meniscus to act over a larger area (Fig. 3.17). In this way the wetted area is identified and Laplace pressure force between the elastic support and the rigid sphere is calculated within each iteration step.

The meniscus radius size increases with P/P_{sat} and is calculated using the Kelvin equation (table 3.2). The simulation starts from $P/P_{sat} = 0.1$, where the size of the meniscus radius is only 0.22 nm. At this P/P_{sat} , the meniscus diameter, $2r = 0.44$ nm, is equal to one ethanol molecule. At $P/P_{sat} = 0.9$, the thickness of adsorbate layer is 1.29 nm, corresponding to 3 monolayers of ethanol. A contact angle of zero has been

3.10 Finite element method (FEM) simulation

Table 3.2: The calculated meridional radius of meniscus and Laplace pressure at different relative ethanol vapor pressures, P/P_{sat} .

Ethanol	P/P_{sat}	$r_{meniscus}$ (nm)	$P_{Laplace}$ (MPa)
	0.1	0.22	99.9
	0.15	0.27	81.4
	0.2	0.32	68.7
	0.3	0.43	51.1
	0.4	0.56	39.2
	0.5	0.75	29.3
	0.6	1.01	20
	0.7	1.45	15.2
	0.8	2.32	9.5
	0.9	4.92	4.5

assumed in the simulations. Note, the simplifying assumption of a zero contact angle may lead to slightly higher adhesion forces in the simulations compared to scenarios with finite contact angles (45). Another boundary condition is that the bottom part of the elastic support is fixed. The other boundaries are free. In addition, the contact between the sphere and the support is frictionless.

3.10.4 Calculation of the adhesion force

In order to calculate the adhesion force, the following forces were calculated

1. Laplace pressure force, F_p , is integrated over the area πl^2 on the surface of the elastic support taking into account the upwards surface deformation (Fig. 3.17.b). This force is in $+z$ direction.
2. The $-F_{REF}$ with REF standing for restoring elastic force on the sphere. $-F_{REF}$ is the force by which the rigid spherical shell indents onto the surface. This force is in $-z$ direction (Fig. 3.21).

The total force acting,

$$F_{Tot} = F_p - F_{FEF} \quad (3.44)$$

is calculated for each indentation controlled by the inner iteration which produces a graph of F_{Tot} -versus-indentation. Adhesion force is by definition, the minimum in the F_{Tot} -versus-indentation curve. By several pre-tests it has been assured, that the FEM

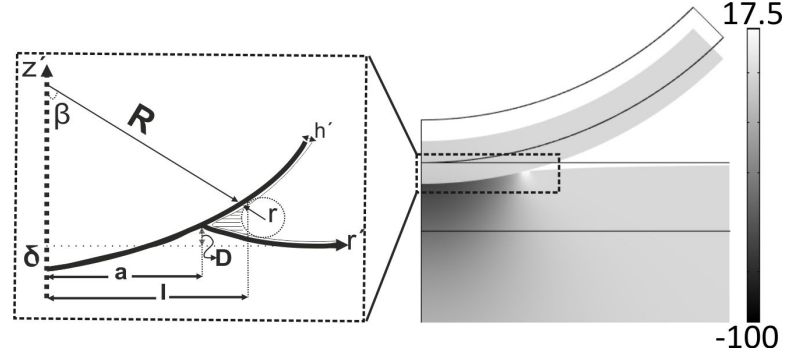


Figure 3.21: FEM result showing the deformation of an elastic support ($E = 400$ MPa) due to the indentation of a sphere, here modeled as a shell section. The sphere indentation d is 99 nm and $P/P_{sat} = 0.7$. Thin black lines indicate the non-deformed geometry. The grey shading encodes the normal stress distribution. Dark (negative values) means compressive, bright (positive values) means tensile stress. The highest tensile normal stress (17.5 MPa) occurs in the meniscus area. The zoom-in is a sketch of the deformed surface in the meniscus area (not to scale). The Laplace pressure deforms the surface upward with a value equal to D , on top of the support.

results are not notably influenced by the model dimensions and boundary conditions. Simulations were carried out with different types of mesh elements at different domain sizes to provide best mesh stability and minimize mesh size effects. Final simulation results were derived with a total number of mesh elements of 58,408 and the total number of degrees of freedom of 384,667.

3.10.5 Studies made by finite element simulations

FEM simulations were performed

1. To show the importance of taking the adsorbate layer into account for the rigid sphere/rigid support geometry. The adhesion forces are calculated for both cases of with and without adsorbate layers for a 170 GPa support. The P/P_{sat} of ethanol is varied from 0.1 to 0.9.
2. To compare the adhesion forces for two different supports, a hard one with a 170 GPa elastic modulus resembling Si wafer and a soft one with an elastic modulus of 400 MPa. Here again the ethanol P/P_{sat} is varied from 0.1 to 0.9.
3. To study the effect of softness on adhesion force through the effect of meniscus on soft surfaces and the corresponding upward surface deformation of the soft

elastic supports. In this part of study, the P/P_{sat} is kept constant at 0.7 and the elastic modulus of the elastic support is varied over a wide range.

The results of all these studies are presented and discussed in the next chapter.

3.11 Summary

In this chapter all the techniques and methods used both to study and compare the effect of a liquid meniscus on hard and soft surfaces were presented. The preparation of both soft cis-1,4 PI and PDMS polymer samples as well as hard Si wafer were explained. Different techniques such as NMR spectroscopy, AFM tapping mode imaging, and SEM imaging were used to characterized either the samples or the colloidal probes.

The colloidal probes preparation procedure was explained. It was also described how such colloidal probes were used to perform force spectroscopy measurements in different environments and conditions. Further it was shown how the adhesion forces can be measured by analyzing the force-versus-piezo displacement curves obtained from a force spectroscopy measurement. The results obtained from the experiments performed with the techniques introduced in this chapter are presented in chapter four.

Finally, the finite element method (FEM) model developed for the studying the effect of Laplace pressure on soft and hard surfaces was introduced. With this model system, the detailed effect of Laplace pressure on the soft surfaces was investigated. In fact, while the analytical model introduced in section 2.8 only considers a Hertzian contact deformation, the FEM simulations also account for surface deformations within the meniscus area due to the Laplace pressure. This effect is not considered in the analytical model and would be investigated by the model introduced in this chapter.

Results and discussion

4.1 Introduction

This thesis was inspired by the following question: '*what is the effect of a soft, deformable surface on capillary forces?*' In order to answer to this question, several experiments and FEM simulations were performed. The experimental results and FEM simulation results were then compared with the analytical model introduced in chapter two.

In the experimental part, the PDMS samples with different mixing ratios of (base:curing agent) as well as cis-1,4 PI polymer samples with different molecular weights are denoted as 'soft samples'. As a hard reference surface, the naturally oxidized Si wafer was selected. In this thesis, first the topography and surface roughness of the soft samples was characterized. Second, the adhesion forces in ambient conditions between the 2 μm radii silica micro-spheres and the soft samples were studied as a function of different (i) cantilever speeds and (ii) dwell times at the peak load. These two sets of experiments together with bulk tensile and compression tests, provided information about the inherent properties of the soft samples in absence of capillary forces. Further, the capillary forces between the 2 μm radius silica micro-spheres and either a silicon wafer or soft samples were measured in the presence of a well-defined ethanol vapor pressure. The interpretation and understanding of these results proved not only the importance of capillary forces but also the role of pre-existing physisorbed layer in the thermodynamic equilibrium conditions. The presence of the physisorbed layers do not change the meniscus curvature but affects the overall geometry of problem (cf.

section 3.8). To check if there is any physisorption of ethanol on the soft samples, SFG spectroscopy was carried out.

FEM simulations were also carried out to calculate the meniscus force for sphere/plane geometry for both hard and soft surfaces. The simulations performed for a hard support with $E = 170$ GPa (similar to that of a Si wafer) showed clearly the importance of the adsorbate layers. In addition, simulations for the soft substrates included both elastic surface deformation of the soft substrate caused by the capillary pressure in the liquid meniscus and the adsorbate layer. While the analytical model introduced in chapter two only considers a Hertzian contact deformation, the FEM simulations also account for surface deformations within the meniscus area due to the Laplace pressure.

4.2 Experimental results

4.2.1 Surface characterization of soft samples using tapping mode imaging

The tapping mode images were recorded on $1 \times 1 \mu\text{m}^2$ areas on top of the soft samples to study their surface morphologies and roughness (Figures 4.1 and 4.2).

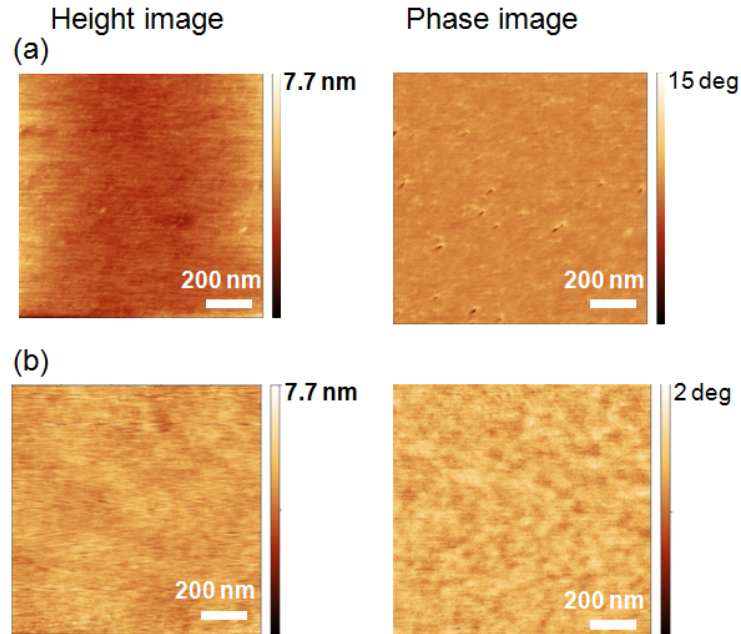


Figure 4.1: Examples of tapping mode height and phase images recorded from the surface of (a): 10:1 PDMS and (b): 20:1 PDMS.

4.2.1.1 Soft 10:1 and 20:1 PDMS samples

The tapping mode height as well as phase images recorded for the 10:1 PDMS and 20:1 PDMS samples indicated that the soft samples' surfaces were smooth and homogeneous with the least amount of contaminations (Fig. 4.1). Therefore, the PDMS samples were reliably used for further adhesion experiments.

The RMS roughness values evaluated from the tapping mode height images were smaller for the 20:1 PDMS samples compared to 10:1 PDMS samples. One possible explanation is that, the 20:1 PDMS sample contains more non-cross-linked species compared to 10:1 PDMS sample because of lower degree of cross-linking. Such non-cross-linked species migrate to the surface creating a smoother surface.

4.2.1.2 Soft cis-1,4 PI samples with different molecular weights

The typical height and phase tapping mode images recorded from the surface of 800 kDa, 1000 kDa and 2500 kDa cis-1,4 PI polymers are shown in Fig. 4.2. The surfaces of the 800 kDa and 1000 kDa cis-1,4PI polymers were smooth and homogeneous without any special surface features. However, the surface of 2500 kDa cis-1,4 PI polymer was covered with fibres, originating from the bulk polymer matrix (cf. Fig. 4.2.c). The formation of such fibril structures is explained by the stress-driven crystallization of the 2500 kDa cis-1,4 PI polymers caused by solvent evaporation (57). From phase images, it was concluded that in comparison with the rest of the matrix, the fibres have different damping properties which can originate from several different factors such as differences in elastic/adhesion properties, different wetting properties, etc.

The evaluated RMS roughness values for different soft cis-1,4 PI polymers samples are given in table 4.1.

Table 4.1: RMS roughness calculated from AFM data

Sample	AFM RMS (nm)	\pm (nm)
10:1 PDMS	0.65	0.15
20:1 PDMS	0.4	0.15
800kDa PI polymer	0.42	0.05
1000kDa PI polymer	0.67	0.08
2500kDa PI polymer	1.2	0.37

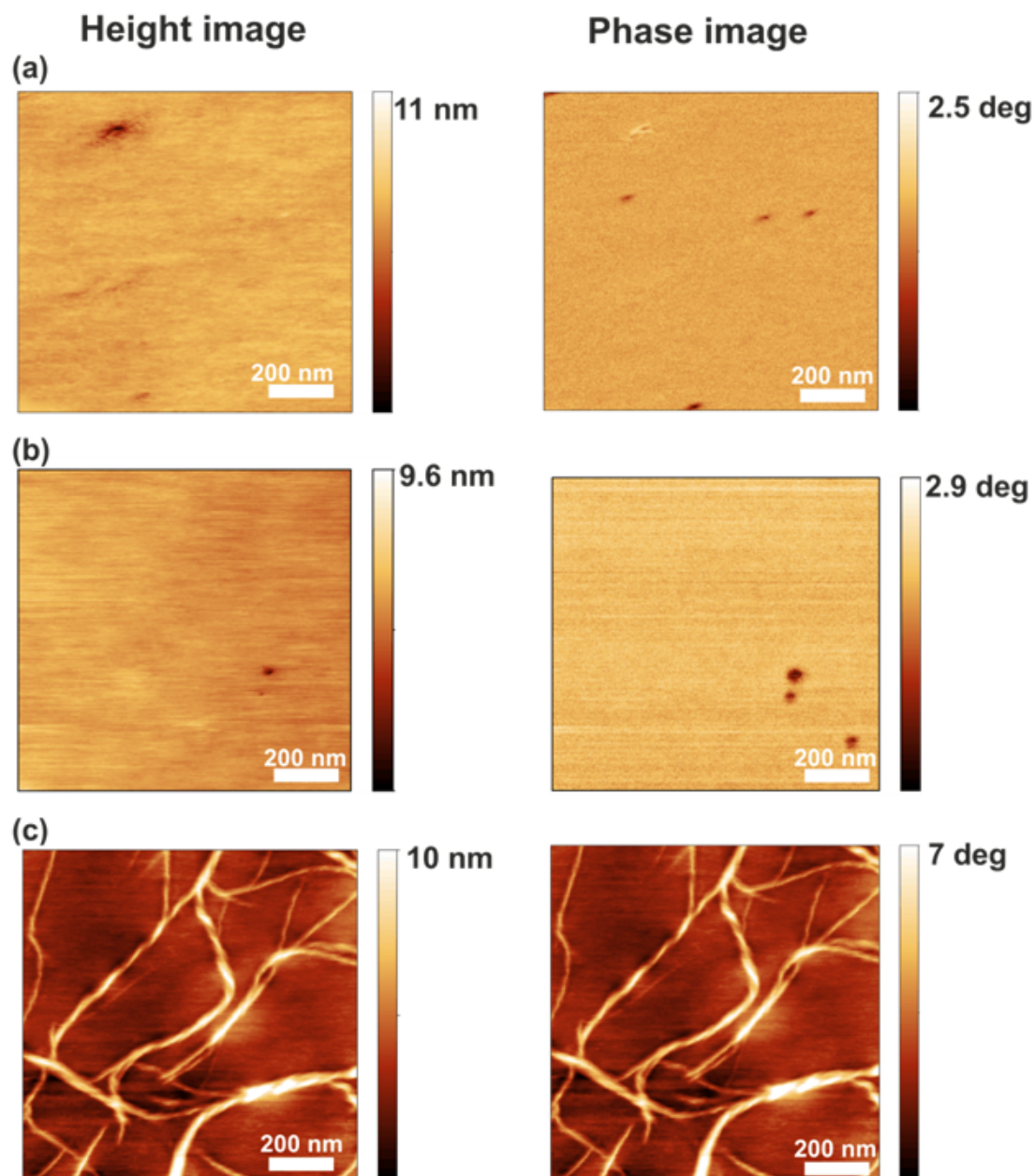


Figure 4.2: Examples of the tapping mode height and phase images recorded from the surface of (a): 800 kDa , (b): 1000 kDa and (c): 2500 kDa cis-1,4 PI polymer samples.

4.3 Adhesion force in the ambient condition: effect of cantilever speed and dwell time

4.2.2 Determining the elastic moduli of the soft samples

The elastic moduli of soft samples were determined from the engineering stress-strain curves recorded in tensile test. The average measured elastic moduli are summarized in the table 4.2. The uncertainty is the standard deviation of the measured elastic moduli.

The highest elastic modulus value was found for to the 10:1 PDMS with the elastic modulus of 1 ± 0.1 MPa. Therefore, for further experiments it is assured that the samples are indeed very soft.

Table 4.2: Elastic moduli of different (base:curing agent) PDMS samples and didderent molecular weights of cis-1,4 PI polymer samples.

Sample	elastic modulus (kPa)	\pm (kPa)
5:1 PDMS	600	–
10:1 PDMS	1000	10
15:1 PDMS	600	–
20:1 PDMS	350	7
PI 800k	458	16
PI 1000k	545	14
PI 2500k	674	11

4.3 Adhesion force in the ambient condition: effect of cantilever speed and dwell time

Two sets of experiments were performed to study the adhesion forces between $2 \mu\text{m}$ radius silica micro-spheres and the soft samples in ambient conditions.

1. *Dynamic adhesion force:* the adhesion forces-versus-different speeds of the cantilever were measured.
2. *Static adhesion force:* the adhesion forces-versus-different dwell times were measured at the peak load. The dwell time is the time for which the silica micro-spheres remained in contact with a soft surface at the peak force before the cantilever was retracted from the sample surface.

These experiments determined the influence of (i) various mixing ratios of (base:curing agent) of PDMS and (ii) different molecular weights of cis-1,4 PI polymer on adhesion

4.3 Adhesion force in the ambient condition: effect of cantilever speed and dwell time

force values in ambient conditions. For both dynamic and static adhesion measurements in ambient conditions, each data point represents the adhesion force which is the mean value obtained from fifteen individual force–piezo displacement curves each recorded at an arbitrary spot on different sample surfaces. The error bars denote the standard deviation obtained from these fifteen force–versus–piezo displacement curves.

4.3.1 Dynamic adhesion measurements: dependence of hysteresis and adhesion force on cantilever speed

The measurements were performed in ambient conditions on 10:1 PDMS, 20:1 PDMS and different molecular weights of cis-1,4 PI polymer samples (800 kDa cis-1,4 PI, 1000 kDa cis-1,4 PI and 2500 kDa cis-1,4 PI polymers). In general, there was always a hysteresis between the loading and unloading part of the force–versus–piezo displacement curves (Fig. 4.3). Such hysteresis in the force curves manifests that more energy is required to separate the silica micro-spheres from the soft surfaces in adhesive contact than is released when they come into contact (5, 75). In fact, when the colloidal probe indents onto the polymer surface, the main energy dissipation is caused by viscoelastic relaxation process in the bulk polymer, whereas when the colloidal probe retracts, relaxation processes also occur at the colloidal probe–polymer interface in addition to the viscoelastic processes in the bulk polymer (71).

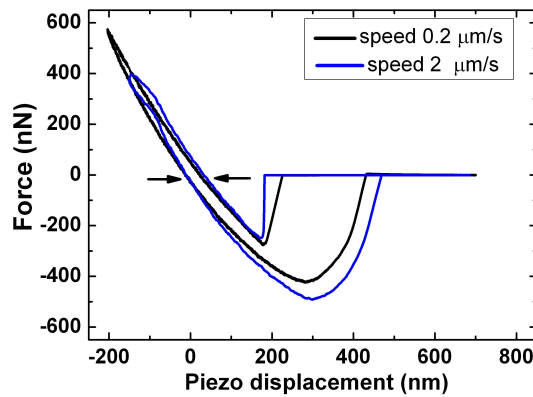


Figure 4.3: Force–versus–piezo displacement curves measured on 10:1 PDMS for two different speeds, 0.2 $\mu\text{m/s}$ and 2 $\mu\text{m/s}$, of the cantilever. The hysteresis between the loading and unloading are marked by two arrows in the constant compliance part of the curves. Please note that for the higher cantilever speed, the adhesion force, i.e. the minimum in force–piezo displacement curve, is larger.

4.3 Adhesion force in the ambient condition: effect of cantilever speed and dwell time

Table 4.3: Values of the hysteresis between the approach and the retract part of the force-versus-piezo displacement curves for different cantilever speeds measured on 10:1 PDMS surface.

Cantilever speeds ($\mu\text{m/s}$)	10:1 PDMS (nm)
47.6	120
15.3	120
2	60
0.44	20
0.3	20
0.22	20

For all soft samples, the size of the hysteresis loop between loading and unloading parts decreased with the drive speed of the cantilever. In fact, for the lower cantilever speeds, the system matches better to the static equilibrium conditions for which viscoelastic effects can be ignored and the loading and unloading curves must coalesce (71). Table 4.3 shows the trend of decrease of hysteresis with speed for the 10:1 PDMS sample. Figures 4.4 and 4.5 show that, the adhesion force increases with the cantilever speed. In fact, with the increase of cantilever speed, the system was given less time to equilibrate, and thus the viscoelastic effect became more evident causing the adhesion force to increase. In this case, the increased frictional resistance to the motion (as a result of viscous resistance to the polymer chain slippage) increases with colloidal probe separation speeds causing higher adhesion forces (40).

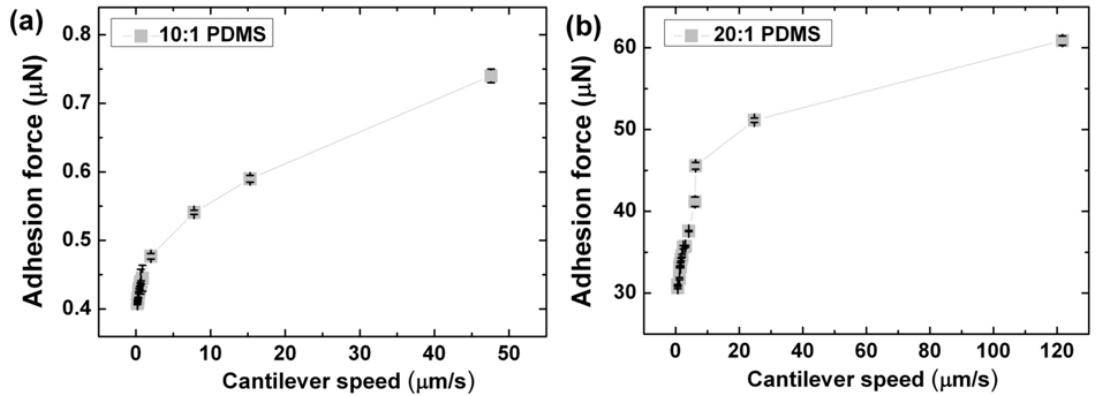


Figure 4.4: The mean values of adhesion force-versus-different cantilever speeds for (a) 10:1 PDMS and (b) 20:1 PDMS samples. The error bars denote the values of the standard deviation.

4.3 Adhesion force in the ambient condition: effect of cantilever speed and dwell time

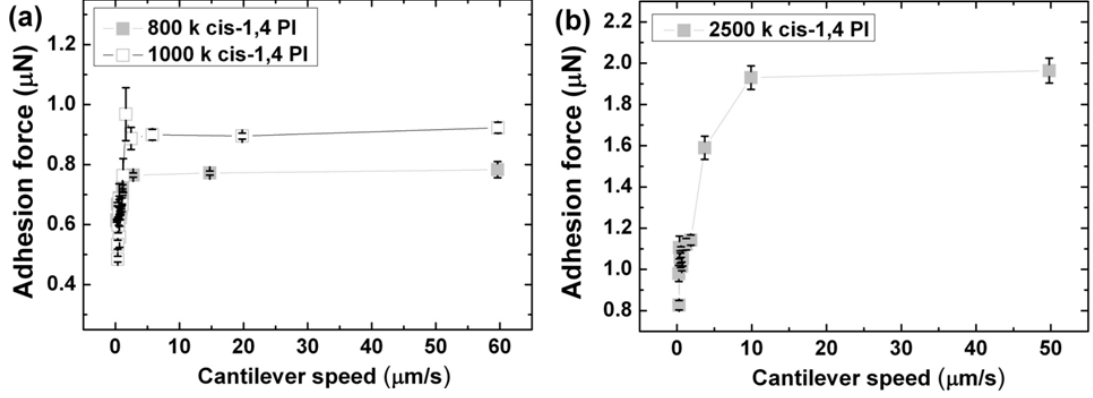


Figure 4.5: The mean values of adhesion force—versus—different cantilever speeds measured in ambient conditions for (a) 800 kDa cis-1,4 PI and 1000 kDa cis-1,4 PI and (b) 2500 kDa cis-1,4 PI polymer samples. The error bars denote the values of the standard deviation.

The maximum value of the adhesion force measured for 20:1 PDMS at the cantilever speed of 2 $\mu\text{m/s}$ was ~ 73 times larger than the one for the 10:1 PDMS sample (Fig. 4.4). The reason for such a huge difference is that the 20:1 PDMS sample contains small molecular weight species that are not cross-linked. Such molecules migrate to sample surface and create a sticky liquid-like viscous layer on top of 20:1 PDMS sample. The adhesion forces between the colloidal probes and such sticky layer is much larger compared to the ones between colloidal probes and the elastic 20:1 PDMS sample itself without such viscous top layer.

For cis-1,4 PI samples, the value of adhesion force at each individual cantilever speed increases with the molecular weight. Former studies (40, 75) have shown that by increasing the molecular weight, more numerous and longer free chains are present at the surface, favouring the enhancement of the interaction between the colloidal probe and the polymer chains. Subsequently, the adhesion forces between the 2 μm radius silica micro-spheres and cis-1,4 PI samples increases with the molecular weight.

4.3.2 Static adhesion: influence of dwell time

To investigate the viscous behavior in more detail, a series of quasi-static adhesion measurements were performed. In these experiments, a colloidal probe was kept in contact with the surfaces of the soft samples at a specific peak load for different time intervals (dwell times). The peak load is the maximum force between a colloidal probe

4.3 Adhesion force in the ambient condition: effect of cantilever speed and dwell time

and the soft samples in the loading part of the force–versus–displacement curve. Figure 4.6 shows that the adhesion force increases with dwell time both for 10:1 PDMS sample and different molecular weights of cis-1,4 PI polymer samples. All measurements were performed with a single cantilever with the peak force of 700 nN.

The trend of increase of adhesion force with the dwell time originates from the fact that for a longer dwell time, the relative viscous flow of soft materials toward the contact area between the colloidal probe and the soft samples is more. Therefore, there are more polymer surface chains motions and molecular rearrangement during the prolonged contact time. These movements allow a better chain adsorption onto the colloidal probe, leading to stronger interactions and higher adhesion forces (40).

Comparing the results of dynamic adhesion measurements in figures 4.4 and 4.5 with the results of static adhesion measurements in figure 4.6 shows that the dwell time has much less effect than cantilever speed for the 10:1 PDMS sample. The adhesion force measured between the colloidal probe and the 10:1 sample for the dwell time of 120 s is only 10 % larger than the one measured for the dwell time of 0.2 s. However, for the cis-1,4 PI polymer samples, the change in adhesion force with the increase of dwell time is much more significant.

Here again, because of the enhanced capability of larger molecular weights of the PI polymer to attach to the colloidal probe, the adhesion forces measured between the colloidal probe and the PI polymer samples increase with the cis-1,4 PI polymer molecular weight at each individual dwell time (40, 75).

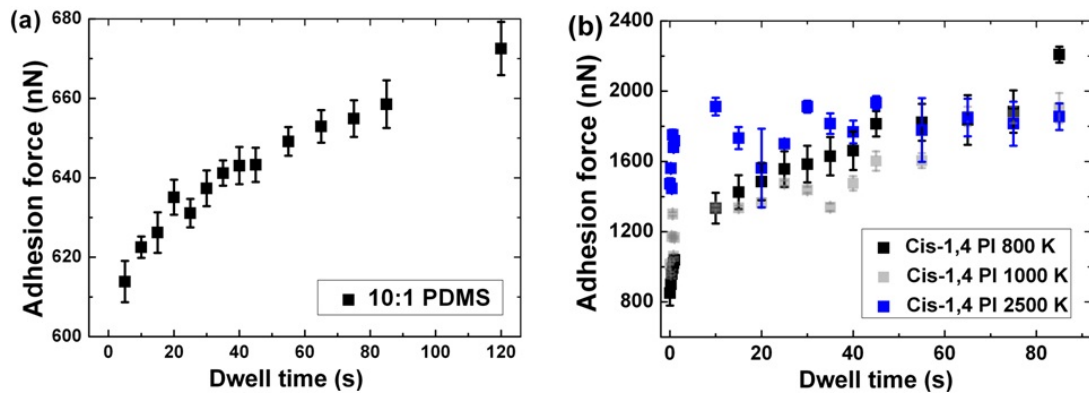


Figure 4.6: The mean values of the static adhesion force–versus–dwell time for (a) 10:1 PDMS and (b) different molecular weights of cis-1,4 PI polymer. The error bars denote the values of the standard deviations.

4.4 Contact angle measurement

The advancing contact angle (ACA) of ethanol on a cleaned 10:1 PDMS sample, a O₂ plasma treated 10:1 PDMS sample, a 800 kDa cis-1,4 PI polymer sample and a cleaned Si wafer were measured by the sessile drop method. The measured values are reported in the table 4.4.¹ These results suggest that assuming zero contact angle for the ethanol on different soft and hard surfaces used in this thesis is a good approximation.

Table 4.4: Advancing contact angles of ethanol on different samples.

Sample	Contact angle (degree)
10:1 PDMS	0
O ₂ treated 10:1 PDMS	<10
20:1 PDMS	0
800 kDa cis-1,4 PI	<10
Cleaned Si wafer	0

4.5 Sum frequency generation (SFG) spectroscopy

sum frequency generation (SFG) vibrational spectroscopy is a technique to study the structure of molecules at surfaces and interfaces. In this thesis, the SFG measurements were performed to check if there was physisorption of ethanol on top of the 10:1 PDMS sample as an example of a CH₃- terminated hydrophobic surface. On one hand, ethanol wets the 10:1 PDMS sample and one expects adsorption of ethanol to its surface to some degree. On the other hand, it is a hydrophobic surface without any pre-adsorbed water layer or hydroxyl groups on its CH₃- terminated surface to initiate physisorption by first forming hydrogen bonds with the first layer of ethanol molecules (10, 11). Therefore, the question arose whether the ethanol physisorption occurs on hydrophobic CH₃- terminated surfaces such as PDMS and cis-1,4 PI polymer surfaces. Figure 4.7 shows the reference SFG signal intensity versus the IR beam frequency from the gold substrate at the air-gold interface. Such a reference spectrum was used to correct for the IR profile in the SFG measurement on the 10:1 PDMS sample. It is known that the SFG signal from the gold reference film is equally strong at all

¹Contact angle measurements were performed in air rather than at saturated vapor pressures of ethanol.

4.5 Sum frequency generation (SFG) spectroscopy

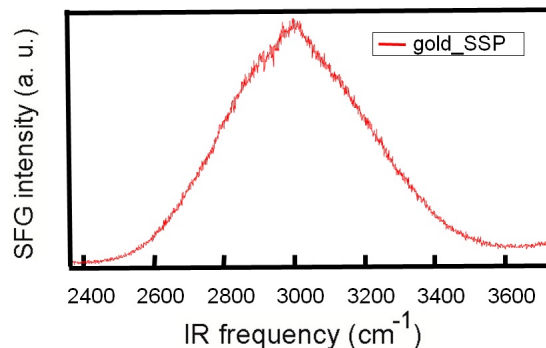


Figure 4.7: The gold reference spectrum showing the spectral profile of the IR pulse

the frequencies and thus a good measure for the spectral profile of the broadband IR pulse. Figure 4.8 depicts the SFG signals measured from four different polarization combinations for the 10:1 PDMS–air interface. The first, second, and third letter in different polarization combinations give the polarization of the SFG, VIS, and IR beams, respectively. The spectrum consisted of one peak at $\sim 2910\text{ cm}^{-1}$, assigned to the symmetric C–H stretch mode of the methyl groups observed in SSP and PPP polarizations (1). The asymmetric stretch mode around 2970 cm^{-1} was only observed under PPP,PSS and SPS polarizations (1).¹

Specific polarizations combinations of the electric fields of SFG, VIS, and IR beams,

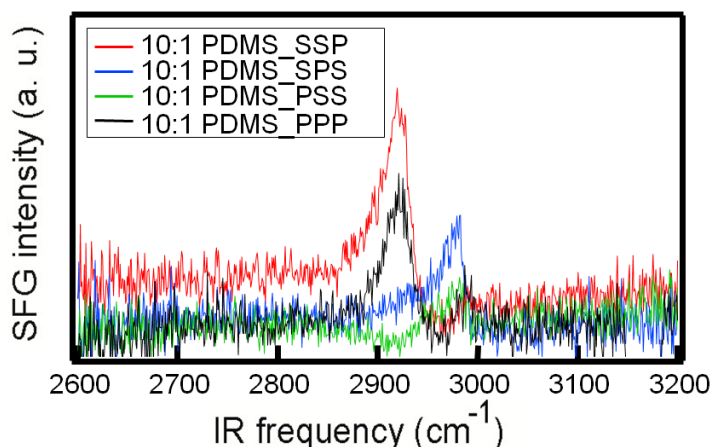


Figure 4.8: The SFG signals obtained from 10:1 PDMS for four polarization combinations. The first, second, and third letter in the polarization combination give the polarization of the SFG, VIS, and IR beams, respectively.

¹The stretching refers to the change in the length of the CH_3 bond. In fact, due to dielectric nature of PDMS, it is possible to observe a SFG signal for all different combinations of polarizations.

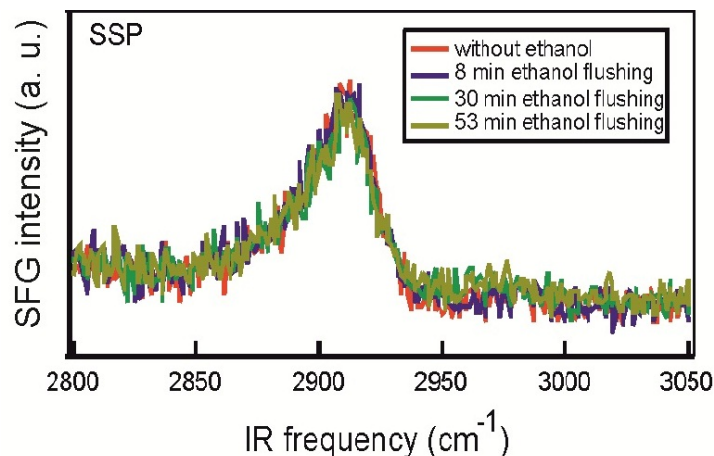


Figure 4.9: Sum generation frequency spectrum (SSP polarization) of the 10:1 PDMS–air interface without and with flushing of ethanol vapor over it.

respectively provide informations about the orientation of such vibrations.

Upon introducing the ethanol vapor in the sample cell, the SFG spectrum did not change: no vibrational resonance was observed for the ethanol adsorption both in the C–H and O–H spectral range. Also, in PPP polarization no signals belonging to ethanol was observed. Clearly ethanol did not adsorb to the hydrophobic 10:1 PDMS surface. Following, based on the SFG experiments, it was assumed that no adsorption of ethanol occurs on soft hydrophobic organic samples. The reason could be that on such surfaces, there is no pre-adsorbed water layer or appropriate adsorption sites for the ethanol molecules. Therefore, the absorption of ethanol could be more favored compared with its adsorption.

4.6 Adhesion force—versus—relative vapor pressure of a liquid

All measurements of adhesion force—versus— P/P_{sat} of a liquid were performed from $P/P_{sat} = 0$ to $P/P_{sat} = 1$ with the colloidal probe technique. Each data point on the plot of adhesion force—versus— P/P_{sat} represents the mean value of the adhesion forces obtained from 420 individual force—piezo displacement curves recorded at 6 different arbitrary spots on each sample surface. The error bars denote the standard deviations found in 420 times repeated measurements at each constant P/P_{sat} . The colloidal

probe was a silica micro–sphere with the radius of 2 μm .

4.6.1 Adhesion force–versus–relative vapor pressure of water on O_2 plasma treated 10:1 PDMS sample

In most practical applications, water vapor is the molecular species that undergoes capillary condensation. But all the soft samples studied so far are hydrophobic, for which neither the physisorption nor the capillary condensation of water occurs (64, 74). Therefore, the first attempt was to make the samples' surfaces hydrophilic to measure the adhesion forces in different partial relative humidities.

The adhesion force–versus– P/P_{sat} of water measured on the surface O_2 plasma treated 10:1 PDMS sample is shown in Fig. 4.11. Water molecules form hydrogen bonds with the Si–OH groups available on the surface of the O_2 plasma treated 10:1 PDMS sample (62). The increase of adhesion force with partial relative humidity can be explained as follows. Both the meniscus radius of curvature, r , and the thickness of water physisorbed layers on both O_2 plasma treated 10:1 PDMS and the colloidal probe, h' , increase monotonically with water P/P_{sat} so that h'/r also increases monotonically with P/P_{sat} of water (12, 81). Ignoring the surface deformation, eqn. 2.61 changes to

$$|F_{Adh}| = 4\pi\gamma_l R + 2\pi R\gamma_l \frac{h'}{r} \quad (4.1)$$

The first term is constant. Therefore, one expect the increase of the adhesion force as a result of the increase of h'/r value with water P/P_{sat} . The interval between

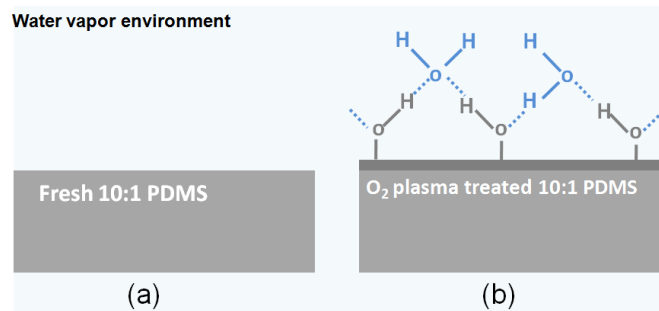


Figure 4.10: Schematic of (a) a hydrophobic as–prepared 10:1 PDMS sample and (b) an O_2 plasma treated 10:1 PDMS with a hydrophilic glassy surface layer of several nano–meter on top. Water molecules readily form hydrogen bonds with the Si–OH groups present on such hydrophilic layer.

4.6 Adhesion force—versus—relative vapor pressure of a liquid

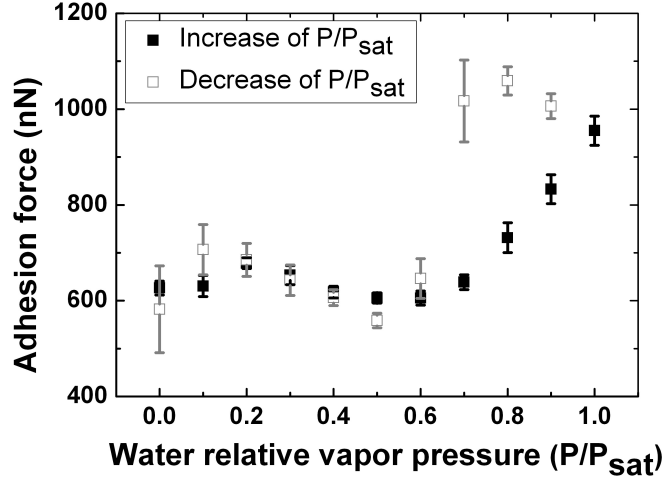


Figure 4.11: The adhesion force—versus—water P/P_{sat} , measured with a silica micro-sphere of $2\ \mu\text{m}$ radius on the O_2 plasma treated 10:1 PDMS. The error bars denote the standard deviations found in 420 times repeated measurements at each P/P_{sat} .

the adhesion measurements at each P/P_{sat} of water was 20 minutes. However, the hysteresis in the measured values of adhesion forces during the decrease of water P/P_{sat} from the saturated condition indicates that it takes a longer time for the water molecules to leave the sample surface.

The experiment also yielded charged surfaces and associated field leading to strong long range attractive forces for $P/P_{sat} < 0.4$. Such a charging effect observed in several experiments, is the result of proton exchange mechanism between the O_2 plasma treated 10:1 PDMS and the silica micro-sphere as the colloidal probe (24, 77, 80, 83). The working hypothesis for the charging mechanism is illustrated in figure 4.12. It is known that the plasma treatment attacks Si-OH bonds on the surface of the PDMS, creating reactive silyl radicals that capture O, OH, and oxygen radicals forming a highly polar surface. On the other hand the silica micro-spheres yield the opposite polarity since silica has an abundance of the hydroxide groups making it more acidic compared with O_2 plasma treated 10:1 PDMS. The existence of unsaturated charges at the interfaces creates the long range electrostatic forces in addition to the interfacial forces between the O_2 plasma treated 10:1 PDMS and the silica micro-sphere.

The O_2 plasma treatment of 10:1 PDMS surface is followed by the hydrophobic recovery of the sample (39). In this phenomena, the thermodynamically unstable hydrophilic surface of O_2 plasma treated 10:1 PDMS regains its hydrophobicity upon ageing because

4.6 Adhesion force—versus—relative vapor pressure of a liquid

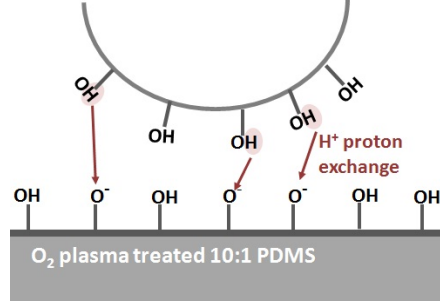


Figure 4.12: Schematic of the proton exchange mechanism between a silica micro-sphere of 2 μm radius and the O₂ plasma treated 10:1 PDMS. The hydrogen protons dissociate from the silica micro-sphere surface and attach to the O₂ plasma treated 10:1 PDMS surface (24).

of the diffusion of the non-cross-linked species or cross-linking residuals to the surface. Therefore, different plasma treatments conditions were tested to obtain the optimum conditions (80% power setting of the maximum O₂ plasma power of 100 W and for 5 s) for which least hydrophobic recovery during the adhesion measurements was negligible.¹ That was hardly achieved for the O₂ plasma treated 10:1 PDMS sample. For Sylgrad 184 PDMS kit, the highest density of cross-linking is obtained for 10:1 (by weight) mixing ratio where 2% total weight remains non-cross-linked (53). The higher as well as lower (base:curing agent) mixing ratios of PDMS such as 5:1, 15:1 and 20:1 result in the decrease of cross-linking density and therefore the enhancement of the hydrophobic recovery (54).² The hydrophobic recovery of PDMS was studied by measuring the advancing contact angle (ACA) of water on 15:1 PDMS treated with 0.1 mbar vacuum, at maximum plasma power of 100 W and for 1 minute during 20 hours. Water had the ACA of $114.7 \pm 0.9^\circ$ on the fresh as-prepared 15:1 PDMS sample. Right after the plasma treatment, the ACA decreased to $< 10^\circ$. Table (4.5) shows the change of the ACA values over the time.³ Finally, it was decided not to use water for further measurements of adhesion force—

¹One must notice that for adhesion measurements, first the liquid cell and chamber were exposed to inert nitrogen gas for half an hour. Then, the vapor pressure was increased. The time given to the system at each P/P_{sat} to reach thermodynamic equilibrium was twenty minutes. Plus the data acquisition at each P/P_{sat} takes 10 minutes. Therefore the whole experiment takes about 12 hours during which the sample surface must be relatively stable.

²It was also certified by tensile test and elastic module determination that the higher as well as lower (base:curing agent) PDMS mixing ratios such as 5:1, 15:1 and 20:1 are softer.

³The author could not find conditions for long term stability of 15:1 PDMS sample better than mentioned above.

4.6 Adhesion force—versus—relative vapor pressure of a liquid

Table 4.5: The change of the water ACA on O₂ plasma treated 15:1 PDMS sample as a result of the sample hydrophobic recovery.

Time (hour)	ACA (degree)
Right after treatment	< 10
1	21.8
1.5	23.1
2	24.9
2.5	25.3
3	27.2
4	30.4
4.5	32.6
20	53.5

versus P/P_{sat} of a liquid to avoid the following problems:

1. Formation of the cracks, increased surface roughness as well as the mixed inhomogeneous hydrophobic and hydrophilic areas on the soft PDMS sample surfaces. Prolonged plasma treatment such as the one used for 15:1 PDMS sample, leads to a large number of cracks on the sample surface. For shorter plasma treatments, the hydrophobic recovery takes place much faster and the surface inhomogeneity is enhanced.
2. The formation of a glassy surface layer on the top of the O₂ plasma treated sample surfaces (Fig. 4.10). The presence of this layer would have made the interpretations of the experimental data as well as the FEM simulations much more difficult.
3. the O₂ plasma treatment of the non-cross-linked cis-1,4 PI polymer samples led to the formation of radicals and degradation of these samples.

Ethanol was selected as a liquid that does wet both the PDMS and cis-1,4 PI surfaces without the need of surface treatment.

4.7 Adhesion force—versus— P/P_{sat} of ethanol

4.7.1 Adhesion force—versus— P/P_{sat} for a hard substrate

The adhesion force—versus— P/P_{sat} of ethanol between a silica micro—sphere and a silicon wafer was only measured while increasing the ethanol P/P_{sat} .¹ The adhesion force increased slightly up to $P/P_{sat} = 0.2$ and then decreased monotonically. In this experiment, one expects the adsorbed ethanol layers on both colloidal probe and the Si wafer surface. Both of these surfaces are hydrophilic, therefore thin layers of water are initially adsorbed onto them (Fig. 4.16) (4). When $P/P_{sat} = 0.15$, an ethanol monolayer has already formed via hydrogen bonding with the existing water layers on the both solid surfaces. With further increase of P/P_{sat} from 0.2 to 0.9, the formation of ethanol multilayers sets in as a result of vdW interactions between the first ethanol monolayer and the ethanol molecules but with a much lower affinity compared to the first ethanol monolayer formation.

The capillary adhesion force for a hard sphere/hard plane geometry without ethanol adsorption layer is simply

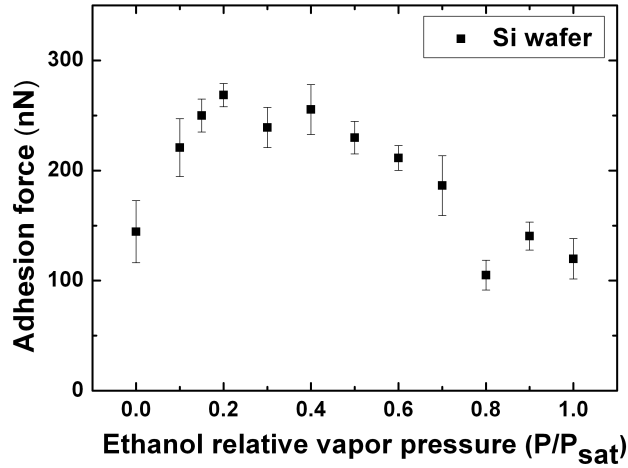


Figure 4.13: Adhesion force—versus— P/P_{sat} of ethanol, measured with silica micro—sphere of 2 μm radius on naturally oxidized Si wafers.

¹The author was not interested to study the hysteresis between the adhesion measurements while increasing and decreasing of ethanol P/P_{sat} . Therefore, the measurements were only performed while increasing the ethanol vapor pressure

4.7 Adhesion force—versus— P/P_{sat} of ethanol

$$|F_{Adh}| = 4\pi\gamma_l R \quad (4.2)$$

which is a constant value and does not depend on P/P_{sat} , since the effect of an increase in meniscus area with increasing relative vapor pressure cancels out with the decrease of Laplace pressure by increase of meniscus radius (44). However, when an adsorbate layer forms on the solid surfaces, filling angle and the meniscus area both grow faster compared to the case that there is no adsorbate layers. As a result, capillary adhesion force depends on P/P_{sat} and follows the eqn. 2.65. Indeed, in eqn. 2.65, h'/r as defined by

$$h'(\frac{P}{P_{sat}})/r = \frac{(7.03(\frac{P}{P_{sat}})^5 - 22.97(\frac{P}{P_{sat}})^4 + 31.76(\frac{P}{P_{sat}})^3 + 21.40(\frac{P}{P_{sat}})^2 + 7.10(\frac{P}{P_{sat}}) - 0.003)}{\lambda_K / \ln \frac{P}{P_{sat}}} \quad (4.3)$$

increases with P/P_{sat} for relative vapor pressures up to around 0.15 and then decreases monotonically (Fig. 4.14). Therefore, the general trend of decrease in adhesion—versus— P/P_{sat} originates from the competition between meniscus radius of curvature, r , and adsorbate layer thickness, h' .

The contribution from an adsorbed layer to the capillary force can be of the same order as the capillary force on a hard substrate, where no adsorbed layer is present.

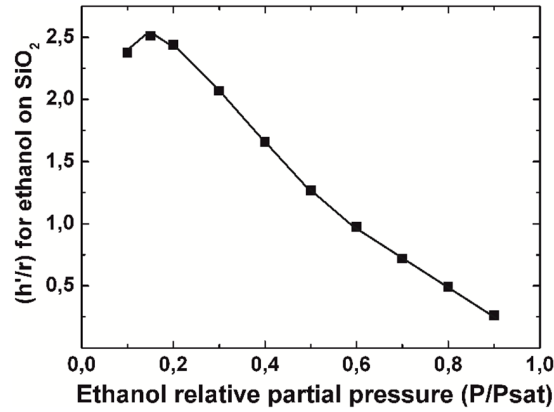


Figure 4.14: Ratio of physisorbed layer thickness h' on Si wafer surface to meniscus radius r in dependence on relative vapor pressure. Calculations were done for a silicon wafer surface in presence of an ethanol vapor. The meniscus radius (r) is calculated from Kelvin equation using eqn. 4.3 and h' is calculated from eqn. 2.36.

4.7.2 Adhesion force—versus— P/P_{sat} for soft PDMS substrates

The adhesion forces—versus— P/P_{sat} of ethanol were measured between a silica micro-sphere and the 10:1 PDMS and 20:1 PDMS samples are presented in Fig. 4.15. As expected, the adhesion forces are higher for the softer 20:1 PDMS sample. At $P/P_{sat} = 0.9$ the absolute value of the adhesion force for the 20:1 PDMS sample is $\simeq 95$ times higher compared to the adhesion force for the 10:1 PDMS sample. Such a large difference in adhesion force values measured on 10:1 PDMS and 20:1 PDMS samples was expected because the 20:1 PDMS sample contains much more non-cross-linked species compared with the 10:1 PDMS sample. Such species migrate to the sample surface and form a sticky liquid-like layer. One must notice that, the 20:1 PDMS samples were washed over night in ethanol bath. However, ethanol is a poor solvent for the 20:1 PDMS and it cannot remove and extract the non-cross-linked species effectively. From the SFG experiments we know that, the physisorption of ethanol does not occur on the 10:1 PDMS and 20:1 PDMS samples and is only expected for the silica micro-spheres as the colloidal probe (10, 23) (Fig. 4.16).

In both experiments, a hysteresis was observed between the adhesion forces measured during the increase and decrease of P/P_{sat} . This hysteresis is much more evident for the 20:1 PDMS sample.

Such a hysteresis can have several different sources. The most relevant one in these ex-

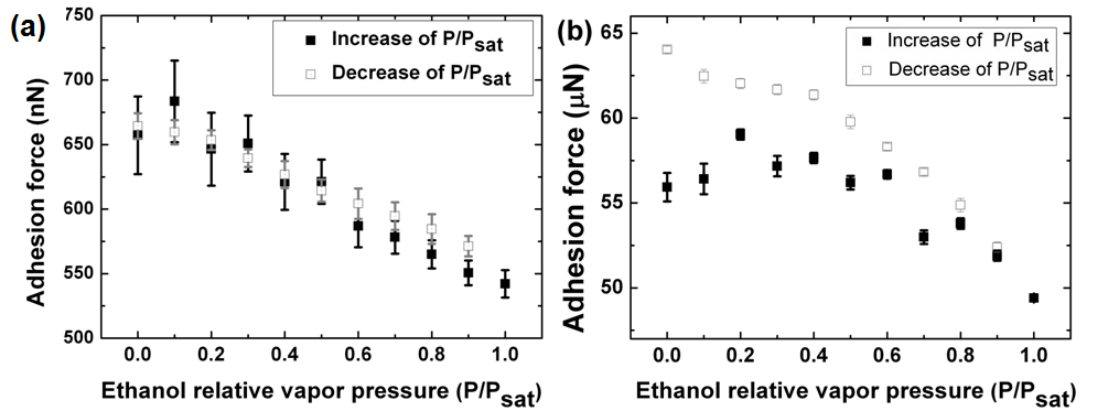


Figure 4.15: Adhesion force—versus— P/P_{sat} of ethanol, measured with silica micro-spheres of $2 \mu\text{m}$ radius on (a) the 10:1 PDMS and (b) the 20:1 PDMS samples. The error bars denote the standard deviations found in 560 times repeated measurements at each constant P/P_{sat} .

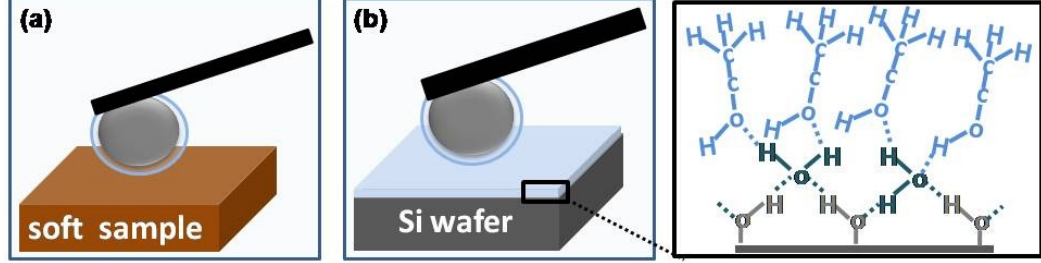


Figure 4.16: Schematic of a system in equilibrium with ethanol vapor consisting of (a): a colloidal probe and a soft sample with the ethanol adsorbate layer only on colloidal probe and (b): a colloidal probe and a Si wafer with the ethanol adsorbate layer on both. Note that the adsorbate layer thickness is not to scale.

periments are the vapor adsorption hysteresis on colloidal probe surface, physical change of 20:1 PDMS and 10:1 PDMS surfaces during the long time exposure to ethanol vapor by absorbing ethanol and finally hysteresis in solid–solid and liquid–solid interactions.

4.7.2.1 The adhesion force—versus—ethanol P/P_{sat} of ethanol: the comparison between Si wafer and soft PDMS samples

For the Si wafer as well as both soft PDMS samples, the adhesion forces showed qualitatively the same dependence on ethanol P/P_{sat} : the adhesion forces first slightly increased and then decreased with increasing the $P/P_{sat} > 0.2$ (Fig. 4.15 and 4.13). These results are interpreted as follows. The adhesion force measured between a silica micro-spheres of 2 μm radius and the Si wafer can be described by

$$|F_{Adh}| = 4\pi\gamma_l R + 2\pi R\gamma_l \frac{h'}{r} \quad (4.4)$$

where the first term is a constant value and the second term changes with P/P_{sat} . Here, the maximum value of adhesion force occurs at the maximum value of the second term.

For softer materials with E^* in the order of several MPa, the adhesion force was derived as

$$|F_{Adh}| = 4\pi\gamma_l R + \pi R h' \frac{\gamma_l}{r} + \left(\frac{\pi\gamma_l}{2r}\right)^3 \frac{2R^2}{3E^{*2}} \quad (4.5)$$

As an example, if one considers $E^* = 400$ MPa, the maximum value of adhesion force, F_{Adh} , occurs for $r = 0.22$ nm at $P/P_{sat} = 0.1$. For such low E^* , the last term in eqn.

4.7 Adhesion force—versus— P/P_{sat} of ethanol

Table 4.6: Comparison of different terms of eqn. 4.5 at two different P/P_{sat}

P/P_{sat}	$4\pi\gamma_l R$	$\pi R h' \frac{\gamma_l}{r}$	$(\frac{\pi\gamma_l}{2r})^3 \frac{2R^2}{3E^{*2}}$
0.1	0.55 μN	0.325 μN	7.27 μN
0.9	0.55 μN	0.035 μN	0.006 μN

4.5 is dominating. Yet, with the increase of P/P_{sat} and subsequently the values of r , meniscus radius of curvature, and h' , the adsorbate layers thickness, the first two terms in eqn. 4.5 also contribute significantly. In order to show different contributions of each term in eqn. 4.5, the values of each term are compared at two different P/P_{sat} of ethanol (table 4.6).¹ Therefore, for at a specific P/P_{sat} , the interpretation of the adhesion force is not straightforward and depends on the values of E^* , h' and r . The above discussion can be qualitatively used to interpret the adhesion forces on soft samples.

In all experiments, the higher adhesion forces were found for the softer materials: F_{Adh} for 20:1 PDMS $>$ F_{Adh} for 10:1 PDMS $>$ F_{Adh} for silicon wafer which is a consequence of the larger contact area between the soft samples and the colloidal probe (last term in eqn. 4.5).

The ratios between the force at $P/P_{sat} = 0.1$ and the force at saturated vapor phase are 1.2 for 20:1 PDMS and 1.3 for 10:1 PDMS, respectively. For the silicon wafer the ratio between the maximum force at $P/P_{sat} = 0.2$ and the force at saturated vapor phase is 2.2. The difference between theses force rations originates from the effect of different values of E^* , r and adsorbate layer thickness, h' on the adhesion forces. For example, for the PDMS samples as compared to the silicon wafer, the value of $\pi R h' \frac{\gamma_l}{r}$ in eqn. 2.62 is just half of $2\pi R h' \frac{\gamma_l}{r}$ in eqn. 2.61. In addition, the contribution from $(\frac{\pi\gamma_l}{2r})^3 \frac{2R^2}{3E^{*2}}$ term must also be taken into account.

4.7.3 Adhesion force—versus— P/P_{sat} of ethanol between the silica micro-spheres and the soft cis-1,4 PI samples

The adhesion forces—versus— P/P_{sat} of ethanol were measured for 800 kDa cis-1,4 PI, 1000 kDa cis-1,4 PI and 2500 kDa cis-1,4 PI polymer samples (Fig. 4.17). For both 800 kDa cis-1,4 PI and 1000 kDa cis-1,4 PI polymer samples, a monotonic decrease of adhesion force with the increase of ethanol P/P_{sat} was observed. But for the 2500 kDa

¹ $R = 2 \mu\text{m}$ and $\gamma_l = 0.022 \text{ N/m}$. r and h' were calculated for ethanol using eqs. 2.34 and 2.36, respectively.

4.7 Adhesion force–versus– P/P_{sat} of ethanol

cis-1,4 PI polymer sample, the adhesion force was almost constant up to $P/P_{sat} > 0.6$ and then decreases monotonically.

Fig. 4.17 also shows that at each individual P/P_{sat} , the value of adhesion forces measured on different cis-1,4 PI polymer samples increases with the molecular weight. This increase comes from the enhanced contribution of vdW forces in contact area between the colloidal probe and the cis-1,4 PI polymer samples with larger molecular weights. Amongst different PI samples, the 800 kDa cis-1,4 PI polymer sample showed the largest hysteresis for the adhesion forces measured while increasing and decreasing of ethanol P/P_{sat} . The reason for such hysteresis was attributed to the ethanol adsorption–desorption hysteresis into and from the polymer film matrix (33, 78). The absorption of the ethanol molecules into the polymer matrix changes the elasticity of the different cis-1,4 PI polymer samples. It has the greatest influence on the 800 kDa cis-1,4 PI polymer sample with the lowest molecular weight as well as degree of entan-

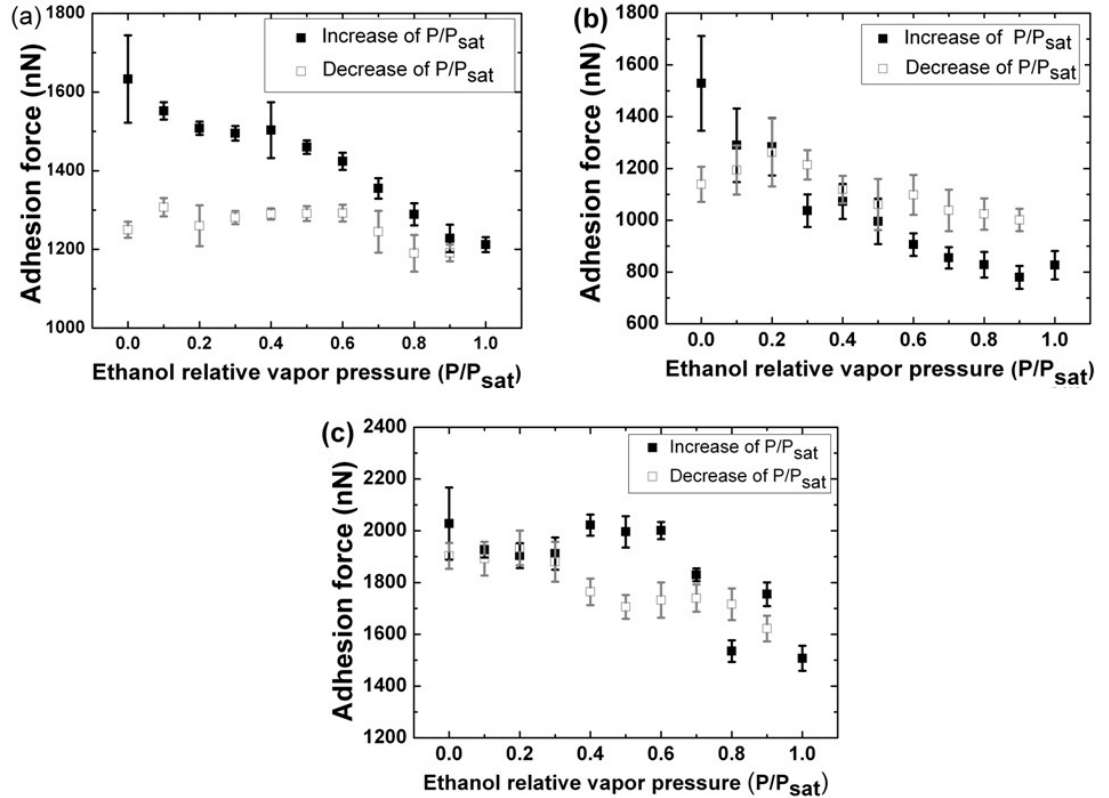


Figure 4.17: Adhesion force–versus– P/P_{sat} of ethanol, measured with silica micro–sphere of 2 μm radius on (a) 800 kDa, (b) 1000 kDa and (c) 2500 kDa cis-1,4 PI polymer samples.

gements. We observed that: the adhesion force measured for at $P/P_{sat} = 0$ at the end of a complete adhesion force-versus- P/P_{sat} measurement, returns back to its initial value at the beginning of the experiment, after being stored for 45 minutes in nitrogen environment.

4.7.3.1 The adhesion force-versus- P/P_{sat} of ethanol: the comparison between a rigid surface and soft PI samples

As expected, the adhesion forces measured on the soft cis-1,4 PI polymer samples are larger compared with the adhesion forces measured on Si wafer. In case of the 800 kDa and 1000 kDa cis-1,4 PI polymer samples, the adhesion force decreases monotonically from $P/P_{sat} = 0.1$. Therefore, the adhesion force-versus- P/P_{sat} of ethanol is fully governed by the $(\frac{\pi\gamma_l}{2r})^3 \frac{2R^2}{3E^{*2}}$ term in equations 2.61 and 2.62 (i.e. softness effect).

In addition, the adhesion forces measured between the silica micro-sphere and 800 kDa cis-1,4 PI and 1000 kDa cis-1,4 PI samples in pure nitrogen environment at ethanol $P/P_{sat} = 0$ are larger compared to the rest of data points at the other P/P_{sat} s. It indicates that adhesion forces arising from solid-solid interaction between the silica micro-sphere and the cis-1,4 PI polymer samples in nitrogen environment are stronger compared with the solid-solid interaction in presence of an ethanol meniscus. In fact, the Young-Laplace equation calculates only the capillary force component while the actual experimental data measures both capillary forces and direct solid-solid contact contributions (45).

Here again, based on the SFG results: no ethanol physisorption on top of different molecular weights of cis-1,4 PI polymer samples is taken into account.

4.7.3.2 The adhesion forces between a 2 μm radius silica micro-sphere and 2500 kDa cis-1,4 PI polymer sample in the liquid ethanol

Among the different molecular weights of cis-1,4 PI polymer samples, the 2500 kDa cis-1,4 PI polymer sample has the highest degree of entanglement, causing a high solvent resistance. In addition, the highest value for adhesion force at ethanol $P/P_{sat} = 0$ was measured between the silica micro-sphere and this sample (cf. Fig. 4.17). Therefore, the 2500 kDa cis-1,4 PI polymer sample was selected for the adhesion force measurements in the liquid ethanol. Fig. 4.18. Twenty nine force-versus-piezo displacement curves were measured at 29 individual arbitrary spots on the sample surface.

4.8 Scanning electron microscope (SEM) images from some of colloidal probes

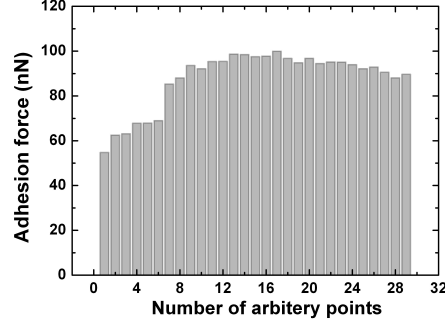


Figure 4.18: The adhesion force measured on the 2500 kDa cis-1,4 PI polymer sample in the liquid ethanol.

Obviously, the values of the adhesion force drops off to less than 100 nN. It can be explained as follows. If one considers the sphere/plane geometry in which the micro-sphere is made from SiO_2 , and the plane is made from 2500 kDa cis-1,4 PI polymer, the medium between them i.e. air is substituted by ethanol. This effectively reduces the vdW forces by changing the Hamaker constant (cf. section 2.2).

4.8 Scanning electron microscope (SEM) images from some of colloidal probes

Figure 4.19. **a–d** shows the SEM images of the colloidal probes used to measure the adhesion force-versus-ethanol P/P_{sat} on different substrates. The colloidal probe with

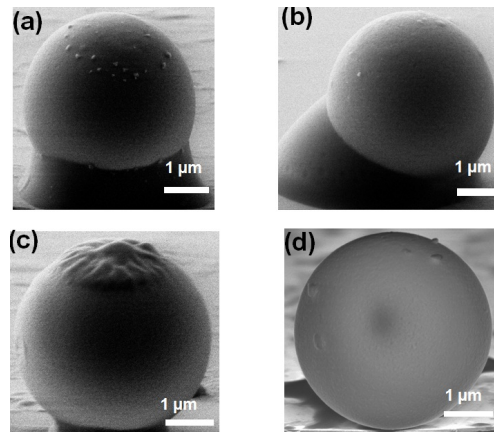


Figure 4.19: SEM images from the probes used for the adhesion-versus- P/P_{sat} of ethanol on the (a) 10:1 PDMS, (b) 800 kDa cis-1,4 PI polymer, (c) 1000 kDa cis-1,4 PI polymer samples and (d) naturally oxidized Si wafer.

4.8 Scanning electron microscope (SEM) images from some of colloidal probes

which the adhesion measurements were performed on 2500 kDa cis-1,4 PI polymer sample could not be imaged for it was detached during the experiment when the whole cantilever was immersed in ethanol.

The SEM images indicate that except for the colloidal probe in Fig. 4.19.c onto which some 1000 kDa cis-1,4 PI polymer is accumulated, the quality of other colloidal probes is very good. The 1000 kDa cis-1,4 PI polymer from which the samples were prepared had already been stored before experiments for a longer time. This extended storage time might have led to partial oxidation of the 1000 k cis-1,4 PI polymer, creating shorter length cis-1,4 PI polymer chains. Such shorter cis-1,4 PI polymer chains can simply accumulate to the colloidal probe at saturated vapor condition.

The SEM images also show that the silica micro-spheres are somewhat rough. The roughness affects the adhesion force measured between a $2\ \mu\text{m}$ silica micro-spheres and different substrates in two different ways. First, by reducing the contact area between the colloidal probes and a sample surface specially for the measurements performed on rigid surfaces. In this case a good effective contact area forms between the soft samples and the colloidal probes because the samples can deform and adopt the surface profile of the colloidal probe. Second, by changing the meniscus radius of curvature as the contact angle has to remain zero. It is, however, only relevant for the surface roughness values smaller than the size of the meniscus curvature, r . (Fig. 4.20).

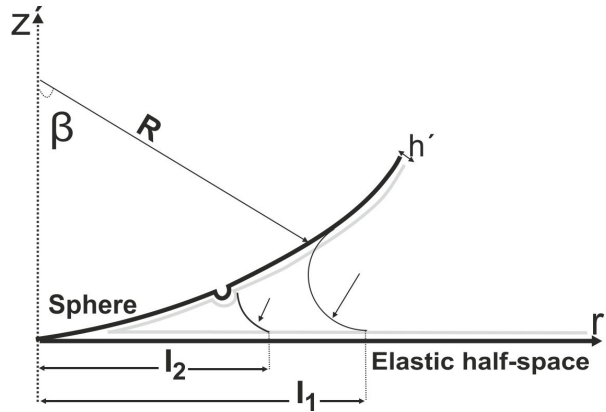


Figure 4.20: A small roughness compared with the meniscus radius, r , on the colloidal probe may result in a big change of the meniscus shape, the area over which the Laplace pressure acts (changing πl_2 to πl_1) and also the contact angle (60).

4.9 Finite element method simulation results

FEM simulations were carried out to calculate the Laplace pressure force including elastic surface deformation of the soft substrates caused by the capillary pressure close to the meniscus. While the analytical model only considers a Hertzian contact deformation, the FEM simulations also account for surface deformations within the meniscus area due to the Laplace pressure. This effect is not considered in the analytical model leads to the higher indentation of the sphere on a soft elastic support and therefore a larger contact area forms. The FEM simulations are performed step by step as follows

1. In order to verify the importance the adsorbate layer together with the meniscus, the FEM simulations were performed for a rigid support, like that of Si wafer.
2. The adhesion force is calculated for an elastic support with the elastic modulus of 400 MPa from $P/P_{sat} = 0.1$ to $P/P_{sat} = 0.9$. The results confirmed the general trend of decrease in adhesion force with the increase of P/P_{sat} .
3. The relative vapor pressure was fixed at $P/P_{sat} = 0.7$ and the elastic modulus of the support was varied from 700 MPa–60 MPa.

In all these simulations, the contact angle of ethanol with solid surfaces was assumed to be zero. This assumption is in good agreement with the experimental advancing contact angle measurements. The other constant variables in the simulations are $\gamma_l = 0.022$ N/m, $R = 2$ μ m, and Poisson ratios of $\nu = 0.2$ for rigid surfaces and $\nu = 0.4$ for soft samples, respectively.

4.9.1 A rigid support

For a support with a high elastic modulus (170 GPa, similar to that of Si substrate) two different cases were studied: with adsorbate layers and without (Fig. 4.21.a). For such a high elastic modulus, the effect of the surface deformation due to Laplace pressure within the meniscus area is in sub-nanometer order (adequately small). Therefore, the FEM simulation results can be directly compared with the analytical predictions.

Without ethanol adsorbate layer, the adhesion force is found to be almost constant (Fig. 4.21.a). It changes slightly from 0.51 μ N for $P/P_{sat} = 0.1$ to 0.54 μ N for $P/P_{sat} = 0.9$. For a hard micro-sphere of 2 μ m radius in contact with a hard elastic support,

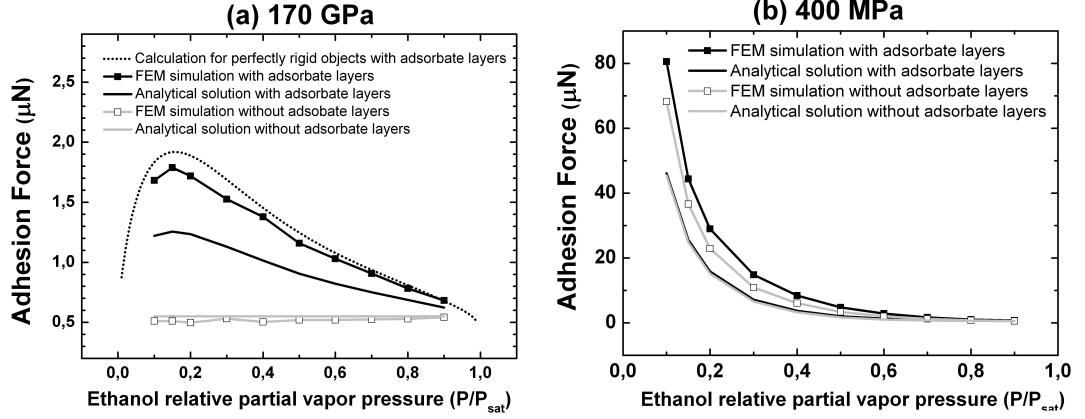


Figure 4.21: Comparison between FEM simulation results and analytical calculations (eqn. 2.61) of adhesion force–versus– P/P_{sat} for (a) 170 GPa and (b) 400 MPa elastic supports with (–■–, –) and without (–□–, –) presence of an ethanol adsorbate layer on both, the surface and the colloidal probe. The dotted line is the exact analytical solution of the capillary force–versus– P/P_{sat} of ethanol between a perfectly hard micro–sphere and a perfectly hard support without any deformation.

the second term in eqn. 2.61 is negligible and the third term is zero when there is no ethanol adsorbate layer. Therefore, the adhesion force is solely governed by the first term which gives $F_{cap} = 4\pi\gamma_l R = 0.55 \mu\text{N}$, in good agreement with the values obtained from simulations.

In the presence of ethanol adsorbate layers, a strong dependency of the adhesion force on the P/P_{sat} appears (Fig. 4.21. a). For both FEM simulations and analytical results, the maximum adhesion force occurs at $P/P_{sat} = 0.15$ which is in a perfect agreement with the previous results published by Kim et al. (4) (cf. section 2.7).

Kim et. al merely calculated the capillary forces assuming perfectly rigid objects. In presence of the adsorbate layers on both surfaces, the calculations for perfectly rigid objects without any indentation of micro–sphere into the support yield higher values compared with the FEM simulations of a micro–sphere indenting a deformable surface (Fig. 4.21.a). It was expected because according to eqn. 2.58 the restoring elastic force from the Hertz contact model is in opposite direction of the Laplace pressure force which means (FEM simulation results with adsorbate layers) = (calculation results for perfectly rigid objects with adsorbate layers) - (the restoring elastic force from the Hertz contact model)

The FEM simulation results however, yield higher adhesion forces in comparison with

4.9 Finite element method simulation results

the analytical results especially for lower relative partial vapor pressures, i.e. for smaller meniscus radii. The difference becomes less with increasing meniscus radius (Fig. 4.21. **a**). This difference has two reasons. First, it is related to the extra contribution of the upward surface deformation of the elastic support due to Laplace pressure in meniscus area (value of D in Fig. 3.17. **b**). Even for a hard material with elastic modulus of 170 GPa, there is still a finite upward surface deformation (for $P/P_{sat} = 0.9$ and $P/P_{sat} = 0.1$, it gives $D = 0.01$ nm and $D = 0.06$ nm, respectively). Second, the assumptions made to derive the analytical solution for the adhesion forces, i. e. eqns. 2.61 and 2.62, lead to an underestimation of the filling angles for small menisci. That is also why a better agreement between FEM simulations and analytical solutions is obtained with increasing meniscus radii, i.e. at larger P/P_{sat} (Figure 4.21).

From the comparison of FEM simulation results for 170 GPa sample, it was also observed that in presence of an ethanol adsorbate layer, the meniscus acts over a larger area and therefore, the adhesion force and the upward surface deformation, D , are both larger.

4.9.2 Soft elastic support

Figure 4.21. **b** shows both the analytical calculations and the FEM simulation results for a soft elastic support with $E = 400$ MPa in presence and absence of adsorbate layers. For such a soft support, the adhesion force decreases monotonically with increase of P/P_{sat} from 0.1 to 0.9.

In general, according to the eqn. 2.61 it can be argued that the trend of decrease in adhesion force with increase of P/P_{sat} has two different reasons: (i) for $P/P_{sat} < 0.5$, the general trend of decrease in adhesion is governed by $(\frac{\pi\gamma_l}{2r})^3 \frac{2R^2}{3E^{*2}}$ term as a result of support softness and (ii) for $P/P_{sat} > 0.5$ all terms do contribute.

As expected in the presence of adsorbate layers, the FEM results yielded higher adhesion forces because the meniscus acts over larger area.

The difference between the absolute values analytical calculations and FEM simulation results at each P/P_{sat} originates from

1. The increase of upward surface deformation for softer supports leads to a larger effective contact area and pushes the liquid meniscus further out. This increase

in area over which the Laplace pressure is acting, results in a higher adhesion force.

2. The underestimation of the filling angle, β , as a result of the assumptions used to derive the analytical expression for the adhesion force (cf. section 2.9)

4.9.3 Dependence on elastic modulus for fixed P/P_{sat}

In order to investigate the effect of elastic modulus on meniscus force including elastic surface deformation, the elastic modulus was varied while keeping $P/P_{sat} = 0.7$. At $P/P_{sat} = 0.7$, the radius of meniscus curvature is 1.45 nm, the ethanol adsorbate thickness is 1.04 nm and the Laplace pressure is 15.2 MPa. In fact, for the larger meniscus size at $P/P_{sat} = 0.7$, the application of continuum model is also better justified.

The choice of this relatively high P/P_{sat} , allowed performing the FEM simulations for the soft elastic supports down to 60 MPa where the Laplace pressure (15.2 MPa) amounts to one forth of elastic modulus. In fact at $P/P_{sat} = 0.7$ and for the $E < 60$ MPa, while calculating F_{Adh} , the strain in the contact area between the micro-sphere and the soft support becomes larger than 50 %. For such values of strain the linear elastic material property as well as current numerical model is not valid any more. For $E < 60$ MPa, the adhesion force can be still calculated using current model but for larger $P/P_{sat} > 0.7$. In fact, for larger meniscus radii, r , the Laplace pressure is lower causing the the indentation of the sphere onto the support. For smaller indentation, the strain is smaller and the current model system can be reliably used.

Figure 4.22.a shows the force-versus-indentation curves for the substrates with different elastic moduli. Each force-versus-indentation curves was obtained by changing the indentation via an inner iteration and calculating corresponding force for each value of indentation. The minimum, which is equal to the adhesion force, is shallower for the harder support ($E = 700$ MPa) and it becomes more and more pronounced with decrease of the elastic modulus. The indentation (δ_{min}) as well as adhesion force increase significantly with decrease of elastic modulus. Figure 4.22.b confirms that the upward surface deformation due to the constant Laplace pressure of 15.2 MPa increases for the softer support materials. Comparing the upward surface deformation for 60 MPa and 700 MPa shows that for a substrate with an elastic modulus of about 12 times lower, the maximum surface deformation is 6.5 times higher.

4.10 Comparing the FEM simulation as well as analytical results with the experiments

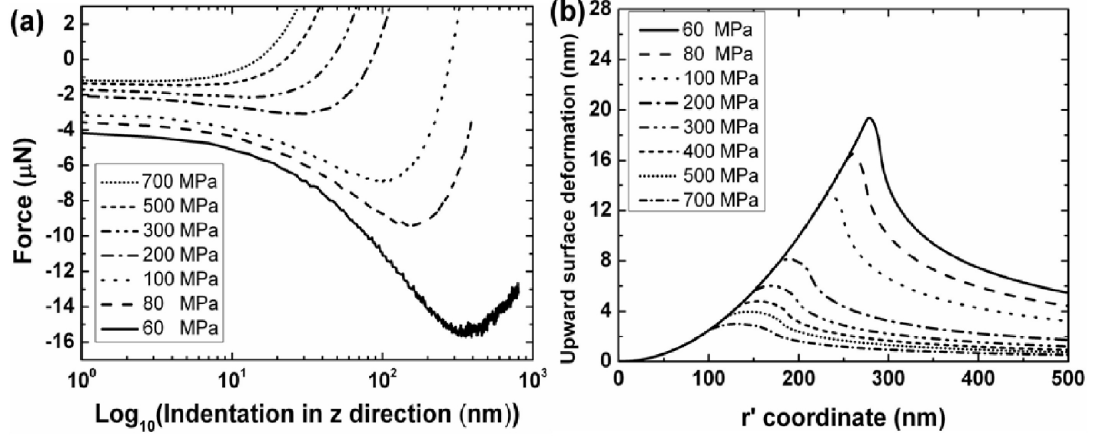


Figure 4.22: (a) simulation results of total force–versus–indentation for elastic supports with different elastic moduli at $P/P_{sat} = 0.7$. For softer materials the equilibrium indentation as well as adhesion force is higher. (b) Upward surface deformations (D in Fig. 3.17.b) versus r coordinate axis for a fixed indentation of 10^{-4} nm. Surface deformation increases with decreasing elastic modulus. The rising edge is defined by the indenting micro–sphere. The apparent deviation from is only due to different scaling of the axes.

The minimum in the total force–versus–indentation curve matches well with the value of δ_{min} calculated from eqn. 2.60 (Fig. 4.23.a). This means that the equilibrium indentation of the micro–sphere onto the solid support hardly changes upon including the surface deformation in the meniscus area. The main effect is therefore the upward surface deformation described above. It leads to a larger effective contact area and pushes the liquid meniscus further out. This increase in area over which the Laplace pressure is acting, results in a higher adhesion force. Therefore, in comparison with the analytical results from eqn. 2.61, the values of F_{Adh} obtained from simulation are therefore slightly larger. This increase in adhesion force becomes especially pronounced for substrates with elastic moduli less than 100 MPa.

4.10 Comparing the FEM simulation as well as analytical results with the experiments

When comparing the experimental results of the silicon wafer (Fig. 4.13) with FEM simulations as well as analytical results (Fig. 4.21.a), there is one main difference. Experimental values are lower than theoretically expected. This effect could be attributed to different factors like the surface roughness of SiO₂ substrate as well as the roughness

4.10 Comparing the FEM simulation as well as analytical results with the experiments

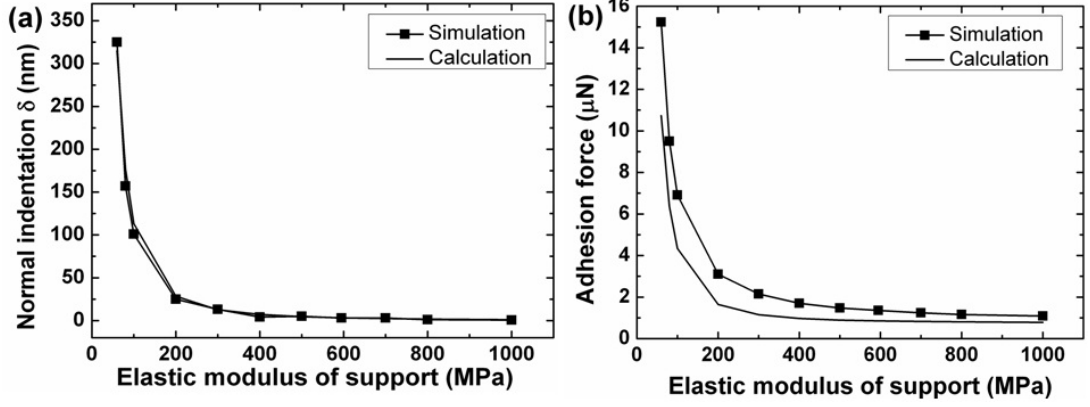


Figure 4.23: (a) Comparison of analytical solution (eqn. 2.60) and FEM model results of δ_{min} (indentation at which the force-versus-indentation curve has its minimum) for different elastic moduli. (b) Comparison of analytical solution of F_{Adh} (using eqn. 2.61) with values obtained from FEM simulations for different elastic moduli at $P/P_{sat} = 0.7$.

of the silica micro-sphere as the colloidal probe (76). Moreover, any trace of organic adsorbate on the surfaces leads to finite contact angle of ethanol with these surfaces whereas zero contact angle was assumed in the models. Finally the amount of initially adsorbed water to the solid surfaces may vary, which changes the adsorbate thickness (45). Each of these possible factors would lead to a decrease of the observed adhesion force. Therefore, the FEM simulation results should represent the highest achievable values for adhesion force in the system and it is thus not surprising that the measured values are lower.

For developing the analytical approach it was assumed that $\delta \ll R$, where δ is the indentation and R is the micro-sphere radius. It is the validity condition for applying Hertz contact mechanics model. Using eqn. 2.60 for 10:1 PDMS with elastic modulus of 1 MPa yields the unrealistic value of $\delta_{min} = 98 \mu\text{m}$. For the FEM simulations, convergence could not be achieved for elastic moduli lower than 60 MPa. The reason is the highly localized stress peak at the location of the meniscus. This leads to large strains within the materials that were hard to handle properly in the simulations even with the highly optimized mesh that were used. Therefore, in case of 10:1 PDMS as well as other soft samples which all have the elastic modulus lower than 1 MPa, it is not possible to compare the experimental results quantitatively with neither the analytical calculations nor the simulation results. Nevertheless, the analytical as well as FEM model approach, could in principle be extended by both incorporating non-linear

material properties and other contact mechanics models. However, to this end also additional measurements for quantifying non-linear material parameters would be needed which was beyond the scope of this thesis.

4.11 Summary

Adhesion measurements between a 2 μm silica micro-spheres and naturally oxidized silicon wafer as well as different soft samples were performed using atomic force microscope under different conditions. The qualitative behaviour of the adhesion force-versus-ethanol P/P_{sat} data could be interpreted on basis of the analytically derived formula eqn. 2.61. It was found that the general force dependence on the partial pressure can only be explained taking adsorption into account. For a rigid support, the observed pressure dependence is solely due to the third term in eqn. 2.61 which is connected to the adsorption isotherm of the liquid layer. In case of a soft support the forces are governed by the interplay between the third and the second term, with the latter one becoming dominant for lower elastic moduli.

With respect to a quantitative comparison of experimental and analytical results, it was found that the experimental forces are lower than the theoretical predictions. However, a quantitative agreement was not to be expected for numerous reasons, e.g. the analytical approach did not consider surface roughness, surface contamination, accurate contact angles and other microscopic details. All these aspects lead to the reduction of adhesion forces in the experimental system.

The simulation results were found to be close to the analytical findings for rigid support, as expected. Yet, differences become more and more pronounced for lower elastic moduli, when the Laplace pressure pulls the support partly onto the micro-sphere surface and vice versa. In this way, the contact area is enlarged leading to an additional force contribution for low elastic moduli, i.e. high adhesion forces. The experimental results on soft samples also confirmed that the contact area as well as the adhesion force is higher on softer material.

5

Conclusion and outlook

5.1 Conclusion

The current PhD thesis started with the aim to find an answer for the question: '*what is the effect of the substrate softness on capillary forces?*' This question was inspired by the wet bio-adhesion mechanism used by tree and torrent frogs with their extremely soft toe pads (9). The answer to was found by studying the capillary forces produced from the capillary condensation of ethanol in the contact area between a sphere and a plane. With such model system the effect of capillary forces on both hard and soft surfaces were investigated. The results show that the softness reduces the influence of surface roughness and induces a larger contact area causing larger adhesion forces. In addition, the adhesion force itself depends presence of adsorbed layers of a liquid on different surfaces.

Within an analytical approach the effect of physisorbed ethanol described by the isotherm introduced by Kim et al. (4) was combined with the earlier work by Butt et al. (21). The new analytical approach revealed three different constituent forces which sum up to the total adhesion force (eqs. 2.61, 2.62): first, capillary adhesion force between a hard sphere in contact with a hard surface; second, a contribution due to the deformation of the elastic support leading to an increased wetted area and third, an additional capillary force contribution in presence of adsorbed ethanol layers. As far as we know, the approximated analytical approach presented in this thesis, is the most complete analytical approach presented so far to explain the effect of the capillary forces on both hard and soft surfaces in thermodynamic equilibrium.

In the experimental part of this thesis, the capillary forces between a 2 μm radius silica bead and soft as well as hard samples were measured. The results provided new insights into the effect of capillary forces on both hard and deformable soft surfaces and could be interpreted on basis of the analytically derived formula eqn. 2.61. It was found that on hard surfaces the general force dependence on the partial pressure could only be explained taking adsorption into account. For a rigid support, the observed pressure dependence was solely due to the third term in eqn. 2.61 which is connected to the adsorbed liquid layers. In case of a soft support the forces are governed by the interplay between the third and the second term, with the latter one becoming dominant for lower elastic moduli.

For rigid supports, the deformation is fully described using Hertzian contact mechanics model. However, in case of soft support materials the Laplace pressure causes an additional upward deformation within the meniscus area. This additional aspect was taken into account within the FEM simulations. The simulation results were found to be close to the analytical findings for rigid support, as expected. Yet, differences become more and more pronounced for lower elastic moduli, when the Laplace pressure pulled the support partly onto the sphere surface and vice versa. In this way the contact area is enlarged leading to an additional force contribution for low elastic moduli, i.e. high adhesion forces. The experimental results on soft samples also confirmed that the contact area as well as the adhesion force is higher on softer materials.

With respect to a quantitative comparing of experimental and analytical results, it was found that the experimental forces are lower than the theoretical predictions. However, a quantitative agreement was not to be expected for numerous reasons, e.g. the analytical approach did not consider surface roughness, surface contamination, accurate contact angles and other microscopic details. All these aspects lead to the reduction of adhesion forces in the experimental system. Yet, the analytical consideration gave valuable insight helping to identify the most relevant force contributions.

5.2 Outlook for future

The model system introduced in this thesis can also be used to study the functionality of vapor-phase lubrication between soft surfaces. According to the results obtained in

this thesis, one expects the reduction of adhesion forces with increase of ethanol P/P_{sat} between two soft surfaces (such as two 10:1 PDMS surfaces).

In this analytical approach as well as the FEM simulations, the surface deformation as a result of sphere indentation was described by the Hertz contact mechanics model which had two important consequences. First, there is no friction forces between the sphere and the support. Second, the system was studied in linear elastic regime and no non-linearity was taken into account. Using other contact mechanics models and also taking into account plastic deformations make it possible to get a better quantitative agreement between the experiments, FEM simulations and analytical approach. In addition it is also possible to study a variety of other systems. As an example, it can be mentioned that the FFM model developed during this thesis was sent to Space Research Institute of the Austrian Academy of Science. There, the FEM model was extended to include the support plastic deformation and was used to study soil mechanics under pressure.

Finally, using the Hertz contact mechanics model, one can introduce a constant volume meniscus with meniscus radii in order of some micrometer in non-equilibrium thermodynamic conditions. It is more relevant for the case of tree frogs because their meniscus radii are also several micrometer.

Bibliography

- [1] AHN, D. & DHINOJWALA, A. (2012). *Sum Frequency Generation Vibrational Spectroscopy of Silicone Surfaces & Interfaces*, vol. 4 of *Advances in Silicon Science*, chap. 2, 23–58. Springer Netherlands. 79
- [2] ASAY, D.B. & KIM, S.H. (2007). Molar volume and adsorption isotherm dependence of capillary forces in nanoasperity contacts. *Langmuir*, **23**, 12174–12178, doi: 10.1021/la701954k. 26
- [3] ASAY, D.B., DUGGER, M.T., OHLHAUSEN, J.A. & KIM, S.H. (2007). Macro- to nanoscale wear prevention via molecular adsorption. *Langmuir*, **24**, 155–159, doi: 10.1021/la702598g. 26
- [4] ASAY, D.B., DE BOER, M.P. & KIM, S.H. (2010). Equilibrium vapor adsorption and capillary force: Exact laplaceyoung equation solution and circular approximation approaches. *Journal of Adhesion Science and Technology*, **24**, 2363–2382. vi, 8, 27, 29, 36, 85, 95, 101
- [5] ATTARD, P. (2002). Friction, adhesion, and deformation: dynamic measurements with the atomic force microscope. *Journal of Adhesion Science and Technology*, **16**, 753–791. 74
- [6] BAILEY, A.I. (1961). Friction and adhesion of clean and contaminated mica surfaces. *Journal of Applied Physics*, **32**, 1407–1412. 18
- [7] BARNES, W.J.P. (2007). Functional morphology and design constraints of smooth adhesive pads. *www/mrs.org/bulletin*, 479–485. v, 2, 3, 4
- [8] BARNES, W.J.P., OINES, C. & SMITH, J. (2006). Whole animal measurements of shear and adhesive forces in adult tree frogs: insights into underlying mechanisms of adhesion obtained from studying the effects of size and scale. *Journal of Comparative Physiology A*, **192**, 1179–1191. 4
- [9] BARNES, W.J.P., GOODWYN, P.P., NOKHBATOLFOGHAAI, M. & GORB, S. (2011). Elastic modulus of tree frog adhesive toe pads. *Journal of Comparative Physiology A*, **197**, 969–978. v, 6, 101
- [10] BARNETTE, A.L. & KIM, S.H. (2012). Coadsorption of n-propanol and water on sio2: Study of thickness, composition, and structure of binary adsorbate layer using attenuated total reflection infrared (atr-ir) and sum frequency generation (sfg) vibration spectroscopy. *The Journal of Physical Chemistry C*, **116**, 9909–9916. 27, 78, 87
- [11] BARNETTE, A.L., ASAY, D.B., JANIK, M.J. & KIM, S.H. (2009). Adsorption isotherm and orientation of alcohols on hydrophilic sio2 under ambient conditions. *The Journal of Physical Chemistry C*, **113**, 10632–10641, doi: 10.1021/jp901064r. 26, 78

BIBLIOGRAPHY

- [12] BEAGLEHOLE, D. & CHRISTENSON, H.K. (1992). Vapor adsorption on mica and silicon: entropy effects, layering, and surface forces. *The Journal of Physical Chemistry*, **96**, 3395–3403. 81
- [13] BHAVIKATTI, S.S. (2007). *Finite element analysis*. New Age International. viii, 53, 60
- [14] BHUSHAN, B. (2003). Adhesion and stiction: Mechanisms, measurement techniques, and methods for reduction. *Journal of Vacuum Science & Technology B: Microelectronics and Nanometer Structures*, **21**, 2262–2296. vi, 1, 17, 18, 19
- [15] BINNIG, G., QUATE, C.F. & GERBER, C. (1986). Atomic force microscope. *Physical Review Letters*, **56**, 930–933, pRL. 43
- [16] BRADLEY, R. (1932). The cohesive force between solid surfaces and the surface energy of solids. *Philosophical Magazine Series 7*, **13**, 853–862. 18
- [17] BUTT, H.J. (1991). Measuring electrostatic, van der waals, and hydration forces in electrolyte solutions with an atomic force microscope. *Biophysical Journal*, **60**, 1438 – 1444. 50
- [18] BUTT, H.J. & JASCHKE, M. (1995). Calculation of thermal noise in atomic force microscopy. *Nanotechnology*, **6**, 1. 52
- [19] BUTT, H.J. & KAPPL, M. (2010). *Surface and interfacial forces*. Wiley-VCH. vi, 12, 14, 17, 31, 48
- [20] BUTT, H.J., CAPPELLA, B. & KAPPL, M. (2005). Force measurements with the atomic force microscope: Technique, interpretation and applications. *Surface Science Reports*, **59**, 1–152. viii, 47
- [21] BUTT, H.J., BARNES, W.J.P., DEL CAMPO, A., KAPPL, M. & SCHONFELD, F. (2010). Capillary forces between soft, elastic spheres. *Soft Matter*, **6**, 5930–5936. 8, 9, 30, 31, 34, 36, 101
- [22] CAPPELLA, B. & DIETLER, G. (1999). Force-distance curves by atomic force microscopy. *Surface Science Reports*, **34**, 1–104. viii, 48, 49
- [23] CHENG, T. & SUN, H. (2012). Adsorption of ethanol vapor on mica surface under different relative humidities: A molecular simulation study. *The Journal of Physical Chemistry C*, **116**, 16436–16446. 27, 87
- [24] COLE, J.J., BARRY, C.R., WANG, X. & JACOBS, H.O. (2010). Nanocontact electrification through forced delamination of dielectric interfaces. *ACS Nano*, **4**, 7492–7498. 82, 83
- [25] CRASSOUS, C.M., JEROME & CHARLAIX, E. (2011). Capillary force between wetted nanometric contacts and its application to atomic force microscopy. *Langmuir*, **27**, 3468–3473. 8
- [26] DERJAGUIN, B., MULLER, V. & TOPOROV, Y. (1975). Effect of contact deformations on the adhesion of particles. *Journal of Colloid and Interface Science*, **53**, 314 – 326. 21
- [27] DOWLING, N.E. (1999). *Mechanical Behavior of Materials: Engineering Methods for Deformation, Fracture, and Fatigue*. Prentice Hall. 54, 55, 56

BIBLIOGRAPHY

- [28] DUCKER, S.T.J.P.R.M., WILLIAM A. (1991/09/19/print). Direct measurement of colloidal forces using an atomic force microscope. *Nature*, **353**, 239–241. 50
- [29] DZYALOSHINSKII, I.E., LIFSHITZ, E.M. & PITAEVSKII, L.P. (1961). General theory of van der waals' forces. *Soviet Physics Uspekhi*, **4**, 153. 15
- [30] EDGAR, M. (2007). Physical methods and techniques nmr spectroscopy. *Annual Reports Section "B" (Organic Chemistry)*, **103**, 331–351. 40
- [31] EMERSON, S.B. & DIEHL, D. (1980). Toe pad morphology and mechanisms of sticking in frogs. *Biological Journal of the Linnean Society*, **13**, 199–216. 3, 4
- [32] ENDLEIN, T., JI, A., SAMUEL, D., YAO, N., WANG, Z., BARNES, W.J.P., FEDERLE, W., KAPPL, M. & DAI, Z. (2013). Sticking like sticky tape: tree frogs use friction forces to enhance attachment on overhanging surfaces. *Journal of The Royal Society Interface*, **10**. 6
- [33] FAVRE, E., NGUYEN, Q.T., SCHAEZEL, P., CLEMENT, R. & NEEL, J. (1993). Sorption of organic solvents into dense silicone membranes. part 1.-validity and limitations of flory-huggins and related theories. *Journal of the Chemical Society, Faraday Transactions*, **89**, 4339–4346. 90
- [34] FEDERLE, W. & ENDLEIN, T. (2004). Locomotion and adhesion: dynamic control of adhesive surface contact in ants. *Arthropod Structure & Development*, **33**, 67–75. 6
- [35] FEDERLE, W., BARNES, W., BAUMGARTNER, W., DRECHSLER, P. & SMITH, J. (2006). Wet but not slippery: boundary friction in tree frog adhesive toe pads. *Journal of The Royal Society Interface*, **3**, 689–697. v, 2, 5, 6
- [36] FISHER, R.A. (1926). On the capillary forces in an ideal soil; correction of formulae given by w. b. haines. *The Journal of Agricultural Science*, **16**, 495–505. 30
- [37] FOGDEN, A. & WHITE, L.R. (1990). Contact elasticity in the presence of capillary condensation: I. the nonadhesive hertz problem. *Journal of Colloid and Interface Science*, **138**, 414–430. 8
- [38] FRENCH, R., CANNON, R., DENOYER, L. & CHIANG, Y.M. (1995). Full spectral calculation of non-retarded hamaker constants for ceramic systems from interband transition strengths. *Solid State Ionics*, **75**, 13 – 33. 16
- [39] FRITZ, J.L. & OWEN, M.J. (1995). Hydrophobic recovery of plasma-treated polydimethylsiloxane. *The Journal of Adhesion*, **54**, 33–45. 82
- [40] GALLIANO, A., BISTAC, S. & SCHULTZ, J. (2003). Adhesion and friction of pdms networks: molecular weight effects. *Journal of Colloid and Interface Science*, **265**, 372–379. 75, 76, 77
- [41] GROTH, C. & MLLER, G. (2007). *FEM fr Praktiker Band 1. Grundlagen: Basiswissen und Arbeitsbeispiele zu FEM-Anwendungen- Lsungen mit dem Programm ANSYS Rev.9/10*. Expert-Verlag GmbH. ix, 60
- [42] HAMAKER, H. (1937). The london-van der waals attraction between spherical particles. *Physica*, **4**, 1058 – 1072. 13

BIBLIOGRAPHY

- [43] HANNA, G., JOM, W. & BARNES, W.P.J., W. ARNES (1991). Adhesion and detachment of the toe pads of tree frogs. *Journal of Experimental Biology*, **155**, 103–125. 4
- [44] HANS-JUERGEN BUTT, K.G. & KAPPL, M. (2006). *Physics and chemistry of interfaces*. Wiley. vi, 23, 24, 86
- [45] HSIAO, E., MARINO, M.J. & KIM, S.H. (2010). Effects of gas adsorption isotherm and liquid contact angle on capillary force for sphere-on-flat and cone-on-flat geometries. *Journal of Colloid and Interface Science*, **352**, 549–557. 66, 91, 99
- [46] HUTTER, J.L. & BECHHOEFER, J. (1993). Calibration of atomic-force microscope tips. *Review of Scientific Instruments*, **64**, 1868–1873. 51
- [47] ISRAELACHVILI, J.N. (2010). *Intermolecular and surface forces, 3rd edition*. Academic Press. vi, 15
- [48] JOHNSON, K.L. & GREENWOOD, J.A. (1997). An adhesion map for the contact of elastic spheres. *Journal of Colloid and Interface Science*, **192**, 326–333. 21, 22
- [49] JOHNSON, K.L., KENDALL, K. & ROBERTS, A.D. (1971). Surface energy and the contact of elastic solids. *Proceedings of the Royal Society of London. A. Mathematical and Physical Sciences*, **324**, 301–313. 5
- [50] KEESOM, W.H. (1921). Die van der waalschen kohäsionkraft. *Physikalische Zeitschrift*, **22**, 364. 12
- [51] LAMBERT, A.G., DAVIES, P.B. & NEIVANDT, D.J. (2005). Implementing the theory of sum frequency generation vibrational spectroscopy: A tutorial review. *Applied Spectroscopy Reviews*, **40**, 103–145. 57
- [52] LAPLACE, P.S. (1805-1806). Sur l' action capillaire. In *Dixieme Livre du Traite de Mecanique Celeste: Paris*, 1–65. 8, 24
- [53] LEE, J.N., PARK, C. & WHITESIDES, G.M. (2003). Solvent compatibility of poly(dimethylsiloxane)-based microfluidic devices. *Analytical Chemistry*, **75**, 6544–6554, doi: 10.1021/ac0346712. 83
- [54] LEE, J.N., JIANG, X., RYAN, D. & WHITESIDES, G.M. (2004). Compatibility of mammalian cells on surfaces of poly(dimethylsiloxane). *Langmuir*, **20**, 11684–11691. 83
- [55] LIFSHITZ, E.M. (1956). The theory of molecular attractive forces between solids. *Soviet Physics JETP (English translation)*, **2**, 73. 15
- [56] LONDON, F. (1930). Ueber einige eigenschaften und anwendungen der molekularkräfte. *zeitschrift fuer Physikalische Chemie (Muenchen, Germany)*, **11**, 222–251. 13
- [57] LUCH, D. & YEH, G.S.Y. (1972). Morphology of strain-induced crystallization of natural rubber. i. electron microscopy on uncrosslinked thin film. *Journal of Applied Physics*, **43**, 4326–4338. 71

- [58] MARMUR, A. (1993). Tip-surface capillary interactions. *Langmuir*, **9**, 1922–1926, doi: 10.1021/la00031a047. 32
- [59] MAUGIS, D. (2000). *Contact, adhesion and rupture of elastic solids*. Springer. 19, 32
- [60] NOSONOVSKY, M. & BHUSHAN, B. (2008). Capillary effects and instabilities in nanocontacts. *Ultramicroscopy*, **108**, 1181–1185. xi, 93
- [61] OHLER, B. (2007). Cantilever spring constant calibration using laser doppler vibrometry. *Review of Scientific Instruments*, **78**, 063701–5. 52
- [62] OWEN, M.J. & SMITH, P.J. (1994). Plasma treatment of polydimethylsiloxane. *Journal of Adhesion Science and Technology*, **8**, 1063–1075. 81
- [63] PIAU, J.M., RAVILLY, G. & VERDIER, C. (2005). Peeling of polydimethylsiloxane adhesives at low velocities: Cohesive failure. *Journal of Polymer Science Part B: Polymer Physics*, **43**, 145–157. 5
- [64] ROY, S. & HORE, D.K. (2012). Simulated structure and nonlinear vibrational spectra of water next to hydrophobic and hydrophilic solid surfaces. *The Journal of Physical Chemistry C*, **116**, 22867–22877. 81
- [65] SAMORI, P. (2008). *STM and AFM Studies on (Bio)molecular Systems: Unravelling the Nanoworld*. Springer. 44
- [66] SCHOLZ, I., BARNES, W.J.P., SMITH, J.M. & BAUMGARTNER, W. (2009). Ultrastructure and physical properties of an adhesive surface, the toe pad epithelium of the tree frog, *Litoria caerulea* white. *Journal of Experimental Biology*, **212**, 155–162. 7
- [67] SHAFRIN, E.G. & ZISMAN, W.A. (1960). Constitutive relations in the wetting of low energy surfaces and the theory of the retraction method of preparing monolayers1. *The Journal of Physical Chemistry*, **64**, 519–524. 23
- [68] SKINNER, L.M. & SAMBLES, J.R. (1972). The kelvin equation-a review. *Journal of Aerosol Science*, **3**, 199–210. 8, 25
- [69] SNEDDON, I.N. (1965). The relation between load and penetration in the axisymmetric boussinesq problem for a punch of arbitrary profile. *International Journal of Engineering Science*, **3**, 47 – 57. 21
- [70] STRAWHECKER, K., ASAY, D.B., MCKINNEY, J. & KIM, S.H. (2005). Reduction of adhesion and friction of silicon oxide surface in the presence of n-propanol vapor in the gas phase. *Tribology Letters*, **19**, 17–21. 26
- [71] SUN, G.C., YUJIE WALKER (2005). Viscoelastic response of poly(dimethylsiloxane) in the adhesive interaction with afm tips. *Langmuir*, **21**, 8694–8702, doi: 10.1021/la050448j. 74, 75
- [72] TABOR, D. & WINTERTON, R.H.S. (1969). The direct measurement of normal and retarded van der waals forces. *Proceedings of the Royal Society of London. A. Mathematical and Physical Sciences*, **312**, 435–450. 15

BIBLIOGRAPHY

- [73] TING, T.C.T. (1966). The contact stresses between a rigid indenter and a viscoelastic half-space. *Journal of Applied Mechanics*, **33**, 845–854. 21
- [74] TU, A., KWAG, H.R., BARNETTE, A.L. & KIM, S.H. (2012). Water adsorption isotherms on ch₃-, oh-, and cooh-terminated organic surfaces at ambient conditions measured with pm-rirs. *Langmuir*, **28**, 15263–15269. 81
- [75] VAENKATESAN, V., LI, Z., VELLINGA, W.P. & DE JEU, W.H. (2006). Adhesion and friction behaviours of polydimethylsiloxane a fresh perspective on jkr measurements. *Polymer*, **47**, 8317–8325. 74, 76, 77
- [76] VAN ZWOL, P.J., PALASANTZAS, G. & DE HOSSON, J.T.M. (2007). Influence of random roughness on the adhesion between metal surfaces due to capillary condensation. *Applied Physics Letters*, **91**, 101905–3. 99
- [77] WANG, Z.L. & WU, W. (2012). Nanotechnology-enabled energy harvesting for self-powered micro-/nanosystems. *Angewandte Chemie International Edition*, **51**, 11700–11721. 82
- [78] WIBAWA, G., HATANO, R., SATO, Y., TAKISHIMA, S. & MASUOKA, H. (2002). Solubilities of 11 polar organic solvents in four polymers using the piezoelectricquartz sorption method. *Journal of Chemical & Engineering Data*, **47**, 1022–1029. 90
- [79] XUE, X. & POLYCARPOU, A.A. (2008). Meniscus model for noncontacting and contacting sphere-on-flat surfaces including elastic-plastic deformation. *Journal of Applied Physics*, **103**, 023502–9. 8
- [80] YANG, Y., LIN, L., ZHANG, Y., JING, Q., HOU, T.C. & WANG, Z.L. (2012). Self-powered magnetic sensor based on a triboelectric nanogenerator. *ACS Nano*, **6**, 10378–10383. 82
- [81] YOUNG, G. (1958). Interaction of water vapor with silica surfaces. *Journal of Colloid Science*, **13**, 67 – 85. 81
- [82] YOUNG, T. (1805). An essay on the cohesion of fluids. *Philosophical Transactions of the Royal Society of London*, **95**, 65–87. 8, 24
- [83] ZHANG, X.S., HAN, M.D., WANG, R.X., ZHU, F.Y., LI, Z.H., WANG, W. & ZHANG, H.X. (2013). Frequency-multiplication high-output triboelectric nanogenerator for sustainably powering biomedical microsystems. *Nano Letters*, **13**, 1168–1172. 82